Politecnico di Torino

ScuDo
Scuola di Dottorato ~ Doctoral School
WHAT YOU ARE, TAKES YOU FAR

Doctoral Dissertation
Doctoral Program in Mechanical Engineering (34th Cycle)

Stability analysis of systems under Parametric Excitation

By

Ghasem Ghannad Tehrani

******

Supervisor(s):
Prof. Teresa Maria Berruti
Prof. Chiara Gastaldi

Doctoral Examination Committee:
Prof. Luigi Carassale, Università di Genova, Italy
Prof. Biao Zhou, Nanjing University of Aeronautics & Astronautics, China

Politecnico di Torino
2022

Declaration

I hereby declare that, the contents and organization of this dissertation constitute my own original work and does not compromise in any way the rights of third parties, including those relating to the security of personal data.

Ghasem Ghannad Tehrani
Politecnico di Torino
2022

* This dissertation is presented in partial fulfillment of the requirements for **Ph.D. degree** in the Graduate School of Politecnico di Torino (ScuDo).

I would like to dedicate this thesis to:
My motivators and unconditional supporters,
my loving parents ***Nasrin*** *&* ***Morteza***
And, my eternal beloved friend,
my brother ***Amirmohammad***

Acknowledgment

I dedicate this thesis to the most inspiring people in my life my Mom, Dad, and my Brother whose presence, unconditional love, and support are my daily motivations to move forward.

My sincere and special acknowledgments go to my dear supervisors Professor Teresa Maria Berruti and Professor Chiara Gastaldi for accepting and trusting me for this doctoral position. Their scientific insights and constructive ideas as well as their positivity, kindness, patience, and support were the key elements to conduct this research work. It was an honor to have the opportunity to not only work and collaborate with them but more importantly to learn a lot from them.

I would like to thank all my dear friends in and outside the University for being by my side on my happy and sad days. I feel blessed to have them in my life. In particular, I am thankful to Farhad, Abbas, Zeeshan, Rizwan, Ehsan, Shahram, Mehrdad, Erhan, Gianmarco, Reddy, Valeria, Serena, and Federica for their positivity and supportive behavior in the workplace.

I would like to send my heartfelt appreciation to Prof. Daniele, Prof. Stefano, Prof. Christian, Prof. Lavella and Prof. Giuseppe at AERMEC group for their ever – smiling, respectful and friendly behavior towards me.

In the end, I am genuinely thankful Professor Muzio Gola, the founder of AERMEC, for establishing such an innovative, scientific, and amicable ambient in the first place.

Ghasem Ghannad Tehrani
Politecnico di Torino
September 2022

Abstract

Unwanted vibrations in mechanical structures may gradually lead to failures of the components and consequently the operating system. Such oscillations could be induced by different external or internal excitation sources depending on the working condition. A particular form of excitation is generated due to the variation of physical characteristic parameter(s) of the operating system with time and is known as 'Parametric Excitation'. Parametric excitation is observable in various mechanical structures such as a simple swinging pendulum, rotating machineries, offshore structures, etc. The main property of a parametrically excited system is the occurrence of unstable zones, containing diverging responses, which are separated from the stable zones by means of the so – called 'Transition Curves'. Such instabilities arise due to pumping extra energy to the operating system when the frequency of the parametric excitation approaches the Twice of the natural frequency/ies or the Combination (summation or difference) of the two different natural frequencies. The regions of instability formed around the twice and combination of the natural frequencies are respectively known as 'Primary' and 'Combination' parametric resonances.

In this research work, the state-of-the-art stability analysis approaches applicable to the study of parametrically excited systems i.e. Floquet Theory, Hill's method, Harmonic Balance Method (HBM), Multiple Scales Method, and recently developed method named Jacobian Based Approach (JBA) are explained in detail. The implementation procedure and the applicability of each stability analysis tool have been explained in detail via an example of a Mass – Spring – Damper. In this chapter, the accuracy and efficiency of JBA have been evaluated by comparing the results and the computational time outputted from this method and the state-of-the-art stability analysis approaches.

A detailed study of the HBM for the stability analysis of a parametrically excited system is performed in the third chapter of the thesis. A Jeffcott rotor supported by Rolling Elements Bearing (REB) is adopted as a case study. Here, the REB due to its varying compliance has been modeled as a time – varying stiffness, introducing the parametric excitation in the system. In this study, an improved form of HBM named 'Trained HBM (THBM)' to obtain the stability plot has been proposed. However, it has been proven that THBM is not efficient to implement for bigger systems. In this chapter, a detailed study of the newly proposed method i.e. Jacobian Based Approach (JBA) is given and its efficiency and applicability have been further investigated.

The study of the JBA's applicability for stability analysis of a more complex system under parametric excitation and an experimental study of the instability triggered by the parametric excitation are performed in chapter 4. For this work, a cantilever beam model mounted on a spring with time – varying stiffness is adopted as a demonstrator. By comparing the stability plots obtained by JBA and Hill's method, the performance of the JBA has been examined. A test rig consisting of a

cantilever beam and an electromagnet unit is designed for the experimental activity. In this study, it has been demonstrated, experimentally and numerically, that the electromagnet generates a time –varying stiffness where by tuning the frequency of the electromagnet to the combination parametric resonance frequency a diverging response of the beam is observed. The validity of this study is justified by validating the numerical results by the results from the experiment at the combination parametric resonance frequency.

Contents

List of Figures

List of Tables

Chapter 1

Introduction & Literature Review

1.1 Introduction

Unwanted vibrations are one of the indisputable occurrences in oscillating structures. Depending on the structure, the excitation imposed on the system can have different sources. For instance, in rotating machinery an unbalance disk, mistuning, flutter, varying compliance of the rolling bearings, defective bearings, cracks etc. can lead to undesirable oscillations of the system.

In some oscillating structures, the extra energy fed into the system might be produced from a physical parameter of the system whose value is a function of time. Such an excitation generated by a time – varying physical parameter of the vibrating system is known as "Parametric Excitation". As a simple illustration of a parametrically excited system, a pendulum with support motion is demonstrated in Figure 1. For small vibration amplitude, the governing equations of motion could be expressed as the following (Das and Wahi, 2017):

$$ML\ddot{\theta} + C\dot{\theta} + \left[MgL - MLA\omega^2 \cos\omega t \right]\theta = 0 \tag{1.1}$$

This is a typical example of a system under parametric excitation caused by a time – dependent stiffness.

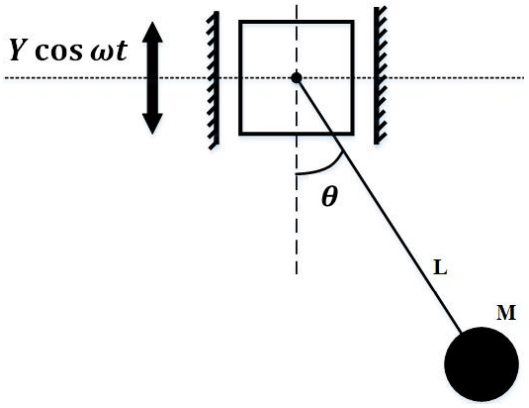

Figure 1: Parametrically excited pendulum

The characteristic of systems under parametric excitation is the emersion of unstable regions around specific exciting parametric frequencies different from simple resonances. Such frequencies are referred to as 'Parametric Resonance Frequencies'. The aforementioned unstable zones contain responses growing with time and periodic responses at their border. The curve passing through the periodic responses are called "Transition Curves" which highlight the boundaries of stability. Typically, the instability due to parametric excitation occurs when its frequency is either close to twice each natural frequency of the system or the combination (summation or subtraction) of the two natural frequencies. The unstable zones/instabilities formed around these frequencies are respectively known as 'Primary Parametric Resonance' and 'Combination Parametric Resonance' regions (Champneys, 2011):

$$\text{Primary Parametric Resonance Frequency: } \eta = \frac{2\omega_{\mathrm{n}i}}{l}$$
$$\text{Combination Parametric Resonance Frequency: } \eta = \frac{\left|\omega_{\mathrm{n}i} \pm \omega_{\mathrm{n}j}\right|}{l} \tag{1.2}$$

Here ω_{n_i} and ω_{n_j} are the natural frequencies of the system and η is the representative of the frequency of the parametric excitation. In Eq. (1.2) l in the denominator is an integer number that determines the order of the resonance and $\underline{l = 1}$ is the most significant case.

Depending on the number of the Degrees of Freedom and Natural Frequencies of the system under parametric excitation, following scenarios may occur:

- In the case of a single Dof system, the instability due to the Primary Parametric Resonance exists. This will be shown in chapter 2.
- In the case of a 2-Dof system with two equal natural frequencies i.e. $\omega_{\mathrm{n}_i} = \omega_{\mathrm{n}_j} = \omega_{\mathrm{n}}$ (like the first two bending modes of a Jeffcott Rotor which will be discussed in chapter 3), the instability due to the Combination Parametric Resonance is present.
- In the case of n-Dof ($\mathrm{n} \geq 2$) system with different natural frequencies ω_{n_i} and ω_{n_j}, instabilities caused by both the Primary and Combination Parametric Resonances arise. This point will be investigated in chapter 4.

The typical approach to study parametrically excited systems is via providing the so – called 'Stability Plot' as demonstrated in Figure 2. As shown in this figure, this plot is built by taking the physical parameters of the understudy system as

control parameters. Depending on the adopted stability analysis method, one would be able to present the stability plot either by determining the area containing the unbounded responses, highlighted by black, or by specifying the Transition Curves (Jazar, 2004) (Rand, 2014). This point will be discussed in detail in chapter 3.

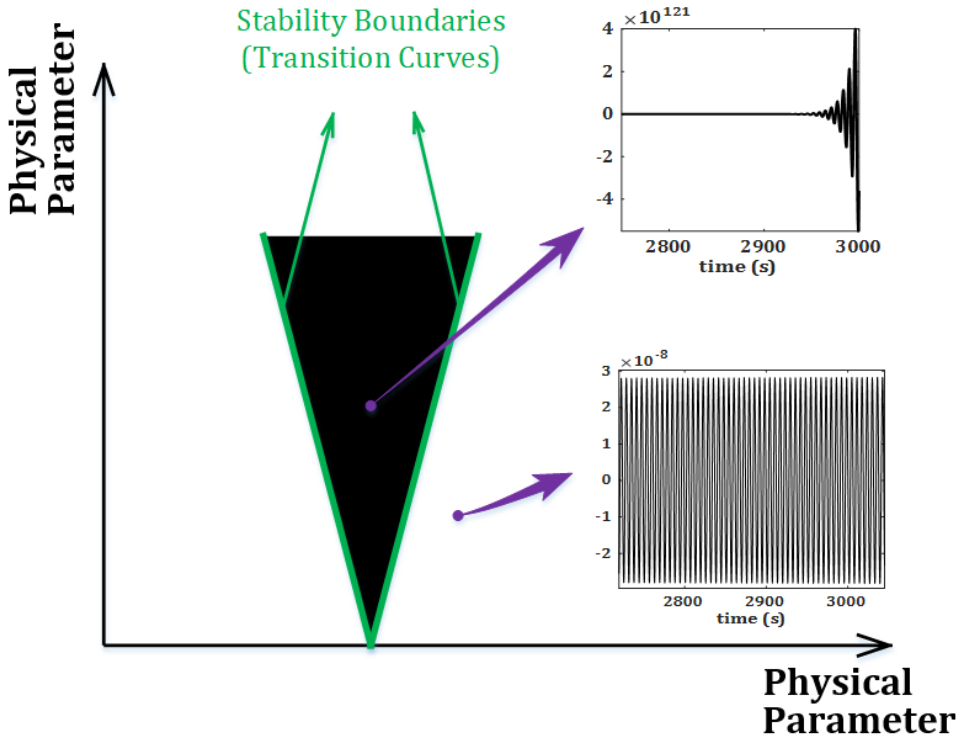

Figure 2: Sample stability plot demonstration

1.2 Literature review

In this section, some of the previous works, theoretical & experimental, regarding the parametric excitation phenomena are reviewed. Here, it has been tried to go over a variety of study contexts involving parametric excitation.

Mathieu equation is considered as the characteristic equation representing parametric excitation. This ordinary differential equation, containing a periodic parameter, has been first proposed by Emile Mathieu (Mathieu, 1868):

$$\ddot{x}+\left(\delta-\varepsilon\cos 2t\right)x=0\,, \tag{1.3}$$

where the real constants δ and ε are respectively named characteristic number and parameter. The presence of time – dependent parameter in Eq. (1.3) is quite

advantageous in studying systems under parametric excitation. Numerous, engineering systems under parametric excitations have been modeled by such an equation and their dynamic behavior has been studied. A comprehensive study of the Mathieu equation has been done in (Kovacic, Rand, and Sah, 2018). This paper starts with the analysis of the simple form of the Mathieu equation where the stability plots are demonstrated. Then, different complementary parts are added such as damping and nonlinearity, and their effect on the primary stability plots are investigated in detail. El-Dib in (El-Dib, 2001) has focused on nonlinear Mathieu equation. In this study, the author utilized the Multiple Scales Method to investigate different sub and super harmonics responses and also their stability. Here, in the stability plots, it has been observed that nonlinearity would result in the generation of stable responses within the unstable responses, distinguished by transition curves. This peculiar phenomenon is called 'coupled resonance regions'. The inhomogeneous, weakly nonlinear, and weakly damped form of the Mathieu equation has been studied in (Ramakrishnan and Brian F Feeny, 2012). In this study, adopting the multiple scales method different resonances of the system due to parametric excitation and nonlinearity have been identified. Rand et. al. in (Rand, Sah, and Suchorsky, 2010) researched a Fractional Mathieu equation. Such an equation according to the authors is applicable in different fields of study such as viscoelasticity, heat conduction etc. In this paper, the authors utilized the harmonic balance method to obtain the transition curves for different orders of the fractional part.

One of the main contributions of the Mathieu equation is characterizing the dynamics of a pendulum under support motion. Nonlinear dynamic analysis of a parametrically excited pendulum has been done in (Garira and Bishop, 2003). Here, the authors performed a detailed analysis to investigate different phenomena due to nonlinearity such as period – doubling, bifurcation etc. A planar pendulum under elliptic force was studied by (Sah and Mann, 2012). Such force which is exerted by moving support is a 'cosine Jacobi elliptic function'. In this paper, the authors investigated the stability plot of the system using Floquet theory and HBM and compared the results. In addition, the effect of the amplitude of the elliptical force on the transition curves has been investigated. The stability analysis of a planar pendulum with butterfly – like motion was performed in (Younesian, Esmailzadeh, and Sedaghati, 2007). Such motion resulted in a governing equation of inhomogeneous Mathieu – type equation. In this study, the authors obtained the stability plot adopting the multiple scales method. An investigation of an asymmetric Mathieu equation which is a special case of the Mathieu equation has been conducted by (Marathe and Chatterjee, 2006). The Mathieu equation here was

adopted to characterize the motion of a pendulum with asymmetric elastic restrains and periodic oscillation of the support. Utilizing the Lyapunov – like exponent method, the authors found the stable and unstable responses of the system. An energy harvesting application attributed to an inverted pendulum floated in water is proposed in (Hasnain *et al.*, 2020). In this paper, the authors followed the purpose of stabilizing the pendulum at its unstable upright equilibrium using parametric excitation. Here, the parametric excitation is simulated by the vertical motion of the pendulum's support and, a generator is attached to the tip of the pendulum to generate the energy.

In addition to the pendulum which is an example of a system with lumped mass (discrete system), numerous studies of continuous systems under parametric excitation have been carried out. A rotating beam under parametric excitation is studied (Arvin, Arena, and Lacarbonara, 2020). In this paper, the parametric excitation is induced by angular velocity modulation, time – dependency of angular velocity, and the stability of the system has been studied. Here the method of multiple scales was adopted and the instability of the first kind, primary parametric resonance, has been investigated. Another study on a parametrically excited beam model is performed by (Zhang *et al.*, 2021). The considered model in this paper is an axially moving beam with time – varying transporting speed. Here, the stability of the system has been studied utilizing the multiple scales method at the primary parametric resonance frequencies. A nonlinear model of a rotating shaft under parametric excitation is considered by (Qaderi, Hosseini, and Zamanian, 2018). In this work, the parametric excitation has been provided by a periodic axial load. Here, it has been concluded that at the combination parametric resonance, the forward whirling mode could be suppressed and its energy transferred to the backward mode. The dynamic behavior of a simply supported beam under parametric excitation is studied by (Xu, Wang, and Li, 2021). Due to the diversity of parametric excitation in frequency, the authors considered the system under multi – frequency parametric excitation. Adopting the Floquet theory, the effect of single and multiple harmonic parametric excitations on the domain of instabilities has been compared and discussed.

From the practical point of view, parametric excitation can be readily observed in a rotor system supported by Rolling Bearing Elements (REB) (Cao *et al.*, 2018). This is due to the time – varying contact forces (equivalent to time – varying stiffness) generated by REB during their angular displacement. Even a healthy REB induces a parametric excitation and it is due to the 'Varying Compliance' (Sharma *et al.*, 2018). As a result of the varying compliance of a loaded bearing, a loading

zone is formed within the bearing where the number of balls alters via rotation and correspondingly the stiffness of the bearing [(Harris, 2001), (Gupta, Gupta, and Sehgal, 2011)]. A detailed study of varying compliance of the REB is performed by (Zhang, Chen, and Cao, 2015a) and (Zhang *et al.*, 2020). After modeling the dynamics of the REB based on the Hertz Contact Theory, the method of harmonic balance and alternating frequency/time domain (HB – AFT) was adopted to seek different types of resonance/instability caused by the varying compliance. Numerous researches on the dynamic behavior of rotor systems mounted on REB have been conducted by scholars. Stability analysis of rotor system induced by the varying compliance of REB has been carried out by (Zhang *et al.*, 2013) and (Zhang *et al.*, 2016). In these papers, the parametric excitation is realized due to time – dependent stiffnesses generated by the supporting bearings. In addition, the instability has been investigated at the primary and combination parametric resonances via Floquet theory. A comprehensive investigation of the influence of varying compliance on the dynamics of a rotor system is performed by (Yang *et al.*, 2018). Here, the authors conducted numerical and experimental analyses to first observe the vibrations induced by varying compliance and also study the effect of different parameters such as the number of the balls and eccentricity on such vibrations. A Jeffcott rotor model supported by REB, considering the varying compliance and centrifugal forces of the REB, is studied by (Haslam, Schwingshackl, and Rix, 2020). In the work, by utilizing the HBM, the nonlinear vibration analysis of the system has been carried out. Furthermore, the stability analysis of the system using the Hill's method has been investigated. The dynamic behavior of a rotor system mounted on REBs in investigated by (Villa, Sinou and Thouverez, 2008) and (Sinou, 2009). In these research works, the nonlinearity due to the varying compliance has been taken into account and a nonlinear vibration analysis using HBM has been accomplished.

Similar behavior to varying compliance which results in the variation of the effective stiffness in time is observed in gearbox systems. In such structures at different time instances, different number(s) of teeth would be in contact; as a result, the effective mesh stiffness changes through time which results in parametric excitation occurrence (Bruzzone and Rosso, 2020). Stability analysis of planetary gear system considering the time – varying mesh stiffness is carried out by (Lin and Parker, 2002). In this paper, the stability plot where the domain of unbounded responses resulted from different parametric resonance frequencies is obtained analytically by the Multiple Scales Method. Approving the aforementioned results numerically, it has been shown that some of the instability regions could be suppressed under specific mesh phasing conditions. A very simple model of one

pair of in – contact gears is given by (Khang, Cau, and Dien, 2004). In this study, the effect of static transmission error in presence of the time – varying mesh stiffness has been investigated numerically and experimentally. An investigation of time - varying mesh stiffness is performed by (Hedlund and Lehtovaara, 2008). In this paper, the authors developed a test rig where the effect of the time – dependent mesh stiffness has been assessed by calculating the natural frequency of the rig. This procedure has been verified numerically by the FE model. The effect of speed fluctuations on instability regions of a planetary gear system is studied by (Qiu, Han, and Chu, 2017). Here, it has been indicated that the presence of speed fluctuations which result in frequency – modulated time – varying mesh stiffness, causes the emergence of more instability regions. In this paper, the exploitation of speed fluctuations to reduce the instabilities is also studied by the authors.

Experimental investigations of instability occurrence due to parametric excitation and also exploitation of parametric excitation have been done in numerous researches. A theoretical and experimental study of a parametrically excited one DOF system has been done by (Yatawara, Neilson, and Barr, 2006). In the experimental part, the authors proposed a pendulum with base excitation and neglected the nonlinearity in the theoretical model. The stability plot obtained for the theoretical model applying Floquet theory well matched the experimental results for low – amplitude of vibrations. Parametric resonances of a double coupled pendulum are investigated by (Hocquet and Devaud, 2020). In this study, the parametric excitation, generated by length modulation, has been tuned around the primary and combination parametric resonances where the boundaries of stability – instability are obtained. In other studies, an electromagnet is used to generate the time – varying spring. The stability of a parametrically excited cantilever beam theoretically and experimentally is studied by (Han, Wang and Li, 2011). In this paper, to tune the numerical model to the experimental one the amplitude of the time – varying stiffness has been computed in terms of the flowing current for the constant gap between the beam and the electromagnet. Another numerical – experimental study of a parametrically excited system has been done by (Han, Wang, and Li, 2011). In this paper, the stability of a cantilever beam excited by two electromagnets has been taken into consideration. In the numerical part, the authors adopted Bolotin's method for the stability analysis. In this paper, the instability investigation was performed for a single value of damping based on different gaps, location of the magnets, and excitation phase. Theoretical and experimental observations of reduction of vibration amplitude at the parametric combination resonance of difference type, are carried out by (Dohnal and Mace, 2008). In this

work, a cantilever beam under an electromagnetic field is used to demonstrate the experimental results. The exploitation of the parametric combination resonance of difference type or so – called "parametric combination anti – resonance" to reduce the vibration amplitudes is studied by (Dohnal, 2012). By adopting three experimental rigs Uniaxial electromagnetic actuator, Cantilever beam under electromagnetic field, and Rotor system with multiple disks mounted on magnetic bearings the author evidenced the occurrence of vibration suppression via augmentation of the damping resulted from the parametric combination anti – resonance. A detailed demonstration of vibration reduction employing the parametric combination anti – resonance is carried out in (Dohnal and Tondl, 2013). In this study, the authors investigated the influecen of parametric combination anti – resonance via modal interactions. Herein, it has been shown that at parametric combination anti – resonance frequency the energy could be transferred between any two modes of interest which results in the suppression of the level of oscillating energy. The application of energy harvesting of a cantilever beam model driven by parametric excitation is proposed in (Zaghari, Rustighi, and Ghandchi Tehrani, 2018). In this paper, the authors performed a complete identification of the experimental model parameters (electrical parameters) to tune the numerical model. It has been demonstrated theoretically and experimentally that at the parametric resonances of the first and second kind, the piezo-electric maximizes energy production.

Other sources of vibration which could give rise to parametric excitation are base (foundation) motions and cracks. Such incidents are observable in engineering structures specifically in rotary machinery. A rotor system model with an angular motion in three orthogonal directions, resulting in time – dependent mass, stiffness, and gyroscopic matrices, is studied by (Han and Chu, 2015). The authors performed the stability analysis via the discrete state transition matrix (DSTM) method. In this paper, the stability plots have been obtained and demonstrated by tuning the parametric frequency around the system's forward, backward, and their summation frequencies. The same model of a rotor as in (Han and Chu, 2015) with a 3D base angular motions and asymmetric disk and shaft is studied by (Yi, Qiu, and Han, 2018). In this research work, stability analysis using DSTM and investigations of different resonances due to the base motions are carried out. The stability of a rotor system, supported by magnetic bearings, under base periodic motions is studied by (Soni, Dutt, and Das, 2020). In this paper, it has been shown that due to the presence of time – varying parameters within the governing equations of motion, the emergence of unbounded/unstable responses is probable. To reduce the instabilities due to parametric excitation, two control laws i.e. PID and Four – element

(proposed by the authors) are considered for the magnetic bearings. The results show that the magnetic bearing operating under the suggested control law leads to a safer operation of the system under parametric excitation. Stability investigation of a rotor system with transverse breathing crack and an initial bending has been accomplished by (Wang, Xiong, and Hu, 2021). By formulating the crack, it has been shown that the stiffness matrix of the system becomes time – dependent which is representative of parametric excitation. In this paper, Hill's method is adopted for the stability analysis. The stability of a rotor system with a cracked shaft is analyzed by (Sawicki and Kulesza, 2015). In this paper, the parametric excitation has been realized as a result of transverse breathing crack simulation. Here, the stability plots are obtained by the averaging method and Floquet theory. Comparing the results, the unstable regions due to primary and combination parametric resonances found by the averaging method are shown to be in good agreement with the ones obtained by Floquet theory.

Stability analysis of offshore structures due to the wave motion is another field of study of vibrations induced by parametric excitation (Chang, 2008). In such structures, the wave of the water flow is introduced as a time – varying parameter in the governing equations of motion. The stability analysis of a top – tensioned riser (TTR) that connects a floating platform to the seabed is investigated by (Lei *et al.*, 2017). In this paper, the parametric excitation has been exerted on the TTR caused by the heave motion of the platform, due to the sea wave, which is formulated by a time – varying tension. The unstable regions of the TTR, modeled by the Bernoulli – Euler beam, have been investigated by the extended precise integration method (EIPM) proposed by the authors. In this study, since at the onset of instability the displacement is small, the linear equation of motion was studied using EIPM. The stability analysis of the US navy's Mobile Offshore Base (MOB) has performed by (Falzarano, Cheng, and Das, 2003). Due to the head seas consideration, only the roll motion, the main motion leading to the instability of the structure, has been taken into account. In this paper, by modeling the roll motion by the well – known Mathieu equation, the stability was obtained numerically using standard offshore analysis software. The dynamic behavior of a container ship during its rolling motion is studied by (Moideen, Falzarano, and Sharma, 2012). In this paper, first, the rolling motion of the ship with mono frequency has been formulated by the Mathieu equation and the possible unbounded response zones are demonstrated. second, it is proven that in the case of multi – frequency waves, the Mathieu equation is not valid anymore and must be substituted by Hill's equation. In addition, the effect of parameters such as nonlinear damping provided by roll

tanks, bilge keels, and the ship's forward speed have been investigated via the stability plot.

Furthermore, in onshore structures such as wind turbines, the vibrations induced by parametric excitation are quite probable. In such structures, variation of the gravity force during the rotations of the blades and the aerodynamics effect of the wind stream introduce time – dependent parameters associated with the coordinate of the system which result in parametric excitation. A forced and nonlinear Mathieu equation representing the transverse vibration of a blade of a turbine, considering the change of the gravity and aerodynamic loads, is proposed by (Ramakrishnan and Brian F. Feeny, 2012). The investigation of superharmonic subharmonic and simple resonances has been done via the Multiple Scales method and the effect of parametric excitation on the amplitude of such resonances has been carried out. The stability analysis of a three – bladed wind turbine modeled as a 5-DOF system has been performed by (Ikeda, Harata, and Ishida, 2018). In this study, the stability plots containing the regions of stable and unstable responses, have been obtained by using Floquet Theory. A simple model of a wind turbine system has been proposed by (Acar, Acar, and Feeny, 2020). In this paper, parametric excitation due to the stiffness variation of the blade caused y the change of gravity force is taken into account. Adopting the multiple scales method, the stability plots are obtained where the regions of instability are highlighted.

In this thesis, an extensive study of all the state-of-the-art stability analysis approaches i.e. Floquet theory, Hill's method, Harmonic Balance Method, and Multiple Scales Method, adopted for analyzing the stability of parametrically excited systems, is carried out. A substantial portion of the thesis is dedicated to a comprehensive and detailed study of the Harmonic Balance Method (HBM) used for the stability analysis of systems under parametric excitation.

The main and core new contributions of this thesis can be summarized as follows.

- Developing a new method named "Jacobian Based Approach (JBA)" to obtain the stability plots
- Proposing an improved procedure of HBM denoted as "Trained HBM (THBM)" to locate accurately the unstable regions
- Design of a simple test rig to prove experimentally the presence of instabilities due to parametric excitation.

1.4 Research objectives & Organization of the thesis

This study has been dedicated to the investigation of the following objectives:

- Examining and Comparing different stability analysis approaches implemented to a system under parametric excitation, with special attention to Harmonic Balance Method (HBM)
- Broadening the application of HBM for stability analysis of a parametrically excited system
- Experimental exploration of the instability caused by the combination parametric resonance frequency

The structure of the thesis is as follows:

- In chapter 2, the state-of-the-art stability analysis approaches i.e. Floquet Theory, Hill's method, HBM, and the newly proposed method in this thesis named Jacobian Based Approach (JBA) are explained in detail through academic examples.
- In chapter 3, stability analysis of a Jeffcott rotor induced by the varying compliance of supporting Rolling Bearing Elements, source of Parametric Excitation, is performed. In this chapter, all the stability analysis approaches introduced in chapter 2 are employed.
- In chapter 4, a supplementary study of JBA for a more complicated model as well as an experimental – numerical investigation of parametric instability due to combination parametric resonance have been carried out.
- The significant outcomes of the thesis and the potential future research topics are given in Chapter 5.
- At the end of the thesis, the references and the appendices are presented.

Chapter 2

Stability Analysis Techniques to Study Systems Under Parametric Excitation: Explanation & Implementation

2.1 Introduction

Due to the probability of instability occurrence in parametrically excited systems, this chapter has been dedicated to the explanation of the employed stability analysis approaches in this work.

In this chapter, the state-of-the-art stability analysis approaches i.e. Floquet Theory, Hill's method, Harmonic Balance Method (HBM), and a recently proposed method named "Jacobian Based Approach" are introduced and explained in detail.

Furthermore, an example of a simple mass – spring – damper is adopted to demonstrate the detailed implementation procedure of each stability analysis approach.

2.2 Floquet Theory

Floquet theory is mainly used to study the linear dynamical systems with periodic coefficients with the following general form:

$$\begin{Bmatrix} \dot{x}_1(t) \\ \dot{x}_2(t) \\ \vdots \\ \dot{x}_N(t) \end{Bmatrix} = \begin{Bmatrix} h_1\left(t,\zeta,x_1(t),x_2(t),\ldots,x_N(t)\right) \\ h_2\left(t,\zeta,x_1(t),x_2(t),\ldots,x_N(t)\right) \\ \vdots \\ h_N\left(t,\zeta,x_1(t),x_2(t),\ldots,x_N(t)\right) \end{Bmatrix} \tag{2.1}$$

In which could be expressed in a compact form as follows:

$$\{\dot{x}(t)\} = \{h(t,\varsigma,\{x(t)\})\} \ , \tag{2.2}$$

where $\{x(t)\}$ is a N – dimensional state vector and ς is a control parameter such as 'Exciting Frequency' in dynamical systems. It must be noted that for a n-DOf system $N = 2n$. The vector symbol $\{\}$ will be dropped for simplicity. Considering a solution of Eq. (2.2) denoted by $x_p(t)$, the stability of this solution could be examined by perturbing it with a small disturbance (Lazarus and Thomas, 2010):

$$x(t) = x_p(t) + p(t) \ , \tag{2.3}$$

where $p(t)$ is a perturbing term. Substituting Eq. (2.3) in Eq. (2.2) (Lazarus and Thomas, 2010):

$$\dot{x}_p + \dot{p} = h(t,\zeta,x_p + p) \tag{2.4}$$

Since x_p is a solution of Eq. (2.2), hence, $h(t,\varsigma,x_p) = \dot{x}_p$. By expanding Eq. (2.4) using the Taylor series around x_p:

$$\dot{x}_p + \dot{p} = h(t,\zeta,x_p) + \left(\frac{\partial h}{\partial x}(t,\zeta,x_p)\right)p + O\left(\|p\|^2\right) \ , \tag{2.5}$$

and, reminding that $h(t,\varsigma,x_p) = \dot{x}_p$ and neglecting higher order terms results in the following:

$$\dot{p}(t) = \left(\frac{\partial h}{\partial x}(t,\zeta,x_p)\right)p(t) = J(t)\,p(t) \tag{2.6}$$

Where $J(t)$is the Jacobian matrix and has the same periodic as x_p which is T. The formula of $J(t)$ for a system of the form given by Eq. (2.1) is as follows:

$$J(t) = \begin{bmatrix} \dfrac{\partial h_1(t,\zeta,x_1(t),x_2(t),\ldots,x_N(t))}{\partial x_1} & \cdots & \dfrac{\partial h_1(t,\zeta,x_1(t),x_2(t),\ldots,x_N(t))}{\partial x_N} \\ \vdots & & \vdots \\ \dfrac{\partial h_N(t,\zeta,x_1(t),x_2(t),\ldots,x_N(t))}{\partial x_1} & \cdots & \dfrac{\partial h_N(t,\zeta,x_1(t),x_2(t),\ldots,x_N(t))}{\partial x_N} \end{bmatrix} \tag{2.7}$$

To determine whether $x_p(t)$ is bounded or unbounded, one must investigate if $p(t)$ diverges or converges through time. Eq. (2.6) is a linear homogenous differential equation and therefore it has N linearly independent solutions such that any solution like $p(t)$ could be written in terms of their summation as follows (Thomas, O., Lazarus, A. and Touzé, 2010):

$$p(t) = \sum_{n=1}^{N} c_n p_n(t) , \tag{2.8}$$

where c_n are coefficients determined by the initial condition. Collecting all the p_is in a matrix as $P = [p_1(t)\ p_2(t)\ \dots p_N(t)]$, Eq. (2.8) could be expressed for each of the solutions as below:

$$\begin{aligned} \dot{p}_1(t) &= J(t)\, p_1(t) \\ &\vdots \\ \dot{p}_N(t) &= J(t)\, p_N(t) \end{aligned} \tag{2.9}$$

Gathering all the differential equations in Eq. (2.9), they could be rewritten in the following matrix form:

$$\dot{P}(t) = J(t) P(t) \tag{2.10}$$

Since $J(t)$ is periodic, the following is hold:

$$\dot{p}(t+T) = J(t+T)\, p(t+T) \rightarrow \dot{p}(t+T) = J(t)\, p(t+T) \tag{2.11}$$

According to Eq. (2.11), $p(t+T)$ is a solution of the system where $P(t+T)$ is a matrix of the form $[p_1(t+T) \dots p_N(t+T)]$. Since the system can have just N linearly independent solutions, $P(t+T)$ could be constructed by $P(t)$ as follows:

$$P(t+T) = P(t)\, \Upsilon \tag{2.12}$$

It is observable that Eq. (2.12) builds the response at time $t+T$ from time t. Such mapping enables to study the stability of the response [(Lazarus and Thomas, 2010), (Nayfeh A. H., 1993)]. To compute Υ, one could study Eq. (2.12) at the initial condition $t = 0$:

$$P(T) = P(0)\,\Upsilon \tag{2.13}$$

Since $P(0)$ is a matrix whose columns are linearly independent, it is acceptable to consider it as simple as possible. To this end, $P(0) = I_{N\times N}$ where $I_{N\times N}$ is the identity matrix (Rand, 2014). And, it results in:

$$\Upsilon = P(T) \tag{2.14}$$

In Eq. (2.14) Υ is called 'Monodromy matrix' and has a key role in determining the stability condition. To compute the Monodromy matrix Υ whose dimension is $N \times N$, Eq. (2.10) must be solved numerically over one period T for N times (Lazarus and Thomas, 2010). For the ith time of the numerical computation, take the ith column of $P(0) = I_{N\times N}$ as the initial condition; for example for the 1st time of numerical computation adopt the 1st column of $P(0)$ as the initial condition, for the 2nd time of numerical computation take the 2nd column of $P(0)$ as the initial condition and so on. At the end of each ith time of the numerical computation, the obtained responses must be placed in the ith column of the matrix Υ.

To investigate the role of the monodromy matrix Υ, the following transformation is considered (Rand, 2014):

$$Y(t) = P(t)\,\mathrm{K}\,, \tag{2.15}$$

where $Y(t)$ is another solution of the system and K is a non – singular matrix. Computing $Y(t)$ after one period T results in (using Eq. (2.12) and (2.14)):

$$\begin{aligned} &Y(t+T) = P(t+T)\,\mathrm{K} \rightarrow Y(t+T) = P(t)\,\Upsilon\mathrm{K} \rightarrow \\ &Y(t+T) = Y(t)\,\mathrm{K}^{-1}\Upsilon\mathrm{K} \end{aligned} \tag{2.16}$$

Assuming that the eigenvalues of Υ, known as 'Floquet Multipliers', are distinct (Rand, 2014), then $\mathrm{K}^{-1}\Upsilon\mathrm{K}$ would be a diagonal matrix with the eigenvalues of Υ on its diagonal elements. In this case, Eq. (2.16) turns into N equations of the following form:

$$\begin{aligned} y_1(t+T) &= \lambda_1 y_1(t) \\ &\vdots \\ y_n(t+T) &= \lambda_n y_n(t) \\ &\vdots \\ y_N(t+T) &= \lambda_N y_N(t) \ , \end{aligned} \tag{2.17}$$

where λ_i represents the i[th] eigenvalue of Υ. Eq. (2.17) shows a mapping of $y_n(t)$ at time t into its value at time $t+T$. From Eq. (2.17), it is evident that:

$$\begin{aligned} y_1(t+mT) &= \lambda_1^m y_1(t) \\ &\vdots \\ y_n(t+mT) &= \lambda_n^m y_n(t) \\ &\vdots \\ y_N(t+mT) &= \lambda_N^m y_N(t) \end{aligned} \tag{2.18}$$

According to Eq. (2.18), for an infinite time ($m \to \infty$):

$$\begin{aligned} y_n(t) &\to 0 \text{ if } |\lambda_n| < 1 \\ y_n(t) &\to \infty \text{ if } |\lambda_n| > 1 \end{aligned} \tag{2.19}$$

Eq. (2.19) shows that the perturbing term decays (bounded/stable $x_p(t)$) if all Floquet multipliers are smaller than one in modulus; while the existence of one single Floquet multiplier greater than one in modulus results in the growth of the perturbation term through time and correspondingly unbounded/unstable $x_p(t)$.

When $|\lambda_n| \approx 1$, Depending on the value of λ_n, the following conditions are held:

$$\begin{aligned} \lambda_n &\approx 1 \to y_n(t+T) = y_n(t) \\ \lambda_n &\approx -1 \to y_n(t+2T) = y_n(t) \end{aligned} \tag{2.20}$$

In this case, the response is said to be on the borders of stability which was previously referred to as Transition Curves'. Eq. (2.20) is explained more in detail in APPENDIX A.

It must be mentioned that the Floquet theory is capable of detecting all of the instabilities mentioned earlier in this chapter (Primary and Combination parametric resonances) by computing and examining the absolute value of the eigenvalues corresponding to the Monodromy matrix. This will be investigated and demonstrated later in this chapter.

2.2.1 Case study: 1-Dof mass – spring – damper model

In this section, the implementation procedure of the Floquet Theory for stability analysis of a simple system under parametric excitation is taken into account. For this study, a single Dof mass – spring – damper illustrated in Figure 3 is adopted as an example. The governing equation of the model is as follows:

$$m_1\ddot{x}_1 + C_1\dot{x}_1 + K_{v1}(t)x_1 = 0 \tag{2.21}$$

Where $K_{v1}(t) = K_1 + k_1 \cos \eta t$ is the time – varying stiffness generating the parametric excitation whose frequency is denoted by η. The parametric excitation is a periodic function with period $T = 2\pi/\eta$. The parameters K_1 and k_1 represent respectively the mean(static) value and amplitude of the harmonic part of the time – varying stiffness. The values of the parameters are given in

Table **1**. The damping is proportional and computed by $\alpha m_1 + \beta K_{v1}$.

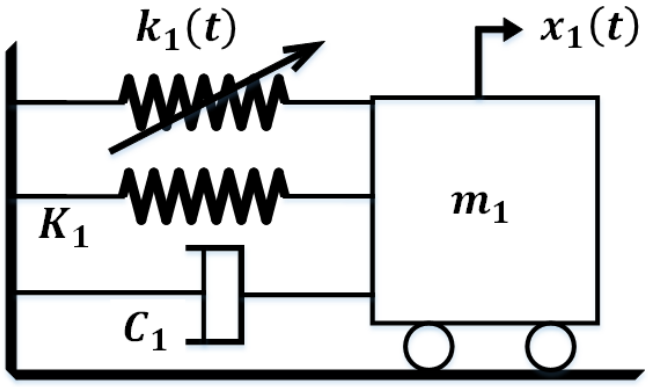

Figure 3: 1DOF Mass – Damper – Spring system with time – varying stiffness

Table 1: Values of the parameters of the model in Figure 3

Parameters	**Values**
$m_1(\mathrm{kg})$	10
$K_1(\mathrm{N/m})$	10^5
$\omega_n(\mathrm{rad/s})$	$\sqrt{K_1/m_1} = 100$
ζ	0.001

For the stability analysis, a solution of Eq. (2.21) x_{1p} is adopted. According to the previous studies e.g. (Champneys, 2011), the employed solution to investigate its stability is the trivial solution of the system which is simply the equilibrium. For the current model, the equilibrium is $x_{1p} = 0$ and stability of the system around its equilibrium under parametric excitation would be studied. By perturbing the trivial solution:

$$x_1 = 0 + p \ , \tag{2.22}$$

and substituting Eq. (2.22) in Eq. (2.21), the subsequent is obtained:

$$m_1\ddot{p} + C_1\dot{p} + K_{v1}(t)\,p = 0 \tag{2.23}$$

To compute the Monodromy matrix, it is required to transform Eq. (2.23) to state – space form. To do so, the two – dimensional state vector $\{y\}$ is defined as follows:

$$\{y\} = \begin{Bmatrix} y_1 \\ y_2 \end{Bmatrix} = \begin{Bmatrix} p \\ \dot{p} \end{Bmatrix} \tag{2.24}$$

Then, using Eq. (2.23) and Eq. (2.24):

$$\begin{Bmatrix} \dot{y}_1 \\ \dot{y}_2 \end{Bmatrix} = \begin{Bmatrix} y_2 \\ -\dfrac{K_{v1}(t)}{m_1} y_1 - \dfrac{C_1}{m_1} y_2 \end{Bmatrix} \tag{2.25}$$

Where $K_{v1}(t) = K_1 + k_1 \cos \eta t$. Using Eq. (2.1) and choosing the control parameters ζ to be equal to the frequency of the parametric excitation η, then:

$$\begin{Bmatrix} h_1(t,\eta,y_1,y_2) \\ h_2(t,\eta,y_1,y_2) \end{Bmatrix} = \begin{Bmatrix} y_2 \\ -\dfrac{K_{v1}(t)}{m_1} y_1 - \dfrac{C_1}{m_1} y_2 \end{Bmatrix} \tag{2.26}$$

To compute the Jacobian matrix in $J(t)$, the derivatives given by Eq. (2.7) must be computed. Here the states are y_1 and y_2, hence:

$$J(t) = \begin{bmatrix} 0 & 1 \\ -\dfrac{K_{v1}(t)}{m_1} & -\dfrac{C_1}{m_1} \end{bmatrix} \tag{2.27}$$

Where $J(t)$ is periodic with T. Then by using Eq. (2.27), Eq. (2.25) would be rewritten as follows:

$$\begin{Bmatrix} \dot{y}_1 \\ \dot{y}_2 \end{Bmatrix} = J(t) \begin{Bmatrix} y_1 \\ y_2 \end{Bmatrix} \tag{2.28}$$

As it was mentioned earlier, to study the stability of the system first the Monodromy matrix given by Eq. (2.14) must be computed. For this study, the parameters k_1 and η are taken as control parameters. To obtain the monodromy matrix, based on the procedure explained after Eq. (2.14), Eq. (2.28) is solved, using time – integration solver, two times (number of states) where each time the computational time lasts for one periodic $T = 2\pi/\eta$ of the parametric excitation. For each computational round e.g. 1st or 2nd, the column of the identity matrix $\mathrm{I}_{2\times2} = \begin{bmatrix} 1 & 0 \\ 0 & 1 \end{bmatrix}$ corresponding to each round of the computation is adopted as the initial condition. By collecting the solutions obtained at the end of each round of the computation i.e. $\begin{Bmatrix} y_1 \\ y_2 \end{Bmatrix}$, in each column of the Υ, the monodromy would be built. For example, solving Eq. (2.28)when $k_1 = 10^3 \left(\frac{N}{m}\right)$ and $\eta = 50 \left(\frac{rad}{s}\right)$ resutls in the following Monodromy matrix $\Upsilon = \begin{bmatrix} 0.9875 & -8.8793 \times 10^{-7} \\ 0.0089 & 0.9875 \end{bmatrix}$. Then, by computing the eigenvalues of the Monodromy matrix and examining their modulus according to Eq. (2.19). For this specific example the vector of the eigenvalues is equal to $\begin{Bmatrix} \lambda_1 \\ \lambda_2 \end{Bmatrix} = \begin{Bmatrix} 0.9875 \\ 0.9875 \end{Bmatrix}$ and since the modulus of both of the eigenvalues are lower than one, hence the system is stable.

Repeating the above procedure for different (η, k_1) values results in the stability plot shown in Figure 4. According to this figure, there are two unstable zones for this model shown by the black areas. The first unstable region is generated due to the simple resonance of the system. As shown here, the line of $\eta = \omega_n$ passes through this area which proves the formation of this region as a result of simple resonance. The second unstable instead appears due to the parametric resonance. According to Figure 4, the second unstable area is formed around the line of $\eta = 2\omega_n$, in which according to Eq. (1.2) for $l = 1$ are frequencies which cause instabilies due to the Primary Parametric resonance. In addition, since the system has just one natural frequency, the parametric instability is due only to the Primary parametric resonance. It is observable from this figure that instability due to the parametric excitation is quite significant and systems under such excitations must be analyzed carefully. It must be noted that the results from Floquet theory would be considered as the reference in the subsequent sections where other stability analysis approaches are explained.

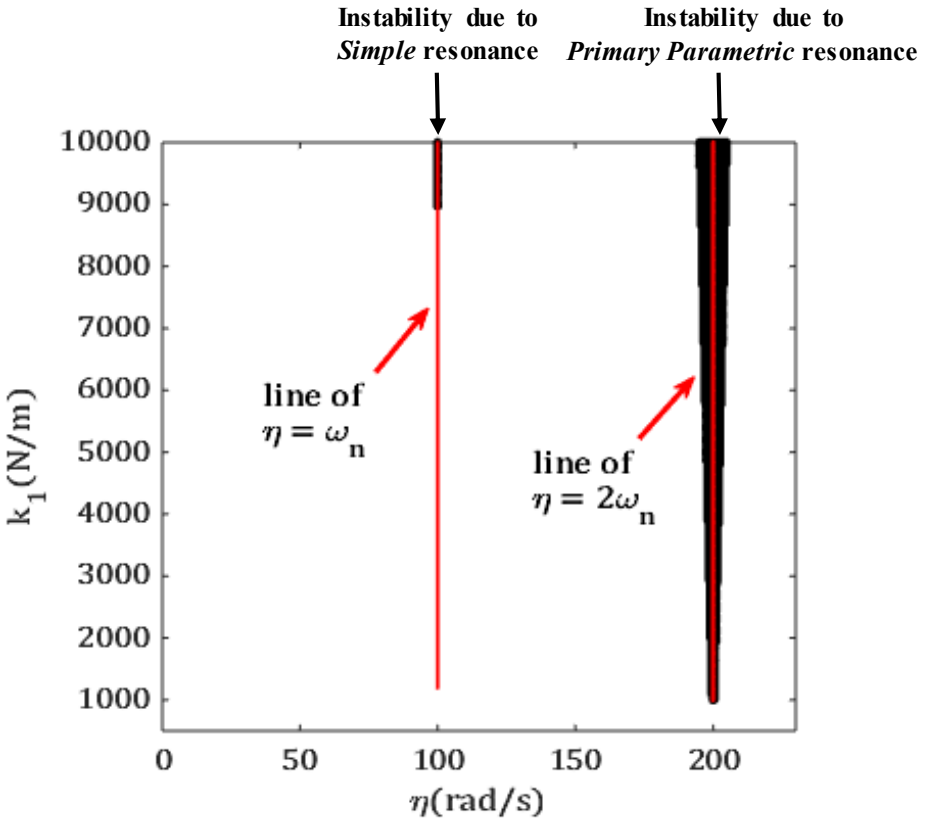

Figure 4: Stability plot of a parametrically excited 1-Dof mass – spring – damper model by implementing Floquet Theory

2.3 Harmonic Balance Method (HBM)

Harmonic balance is an analytical approach that converts the governing equations of motion from the time domain to the frequency domain. By this transformation, one would be easily able to investigate resonance frequencies, study the effect of the nonlinearities [(Gastaldi and Berruti, 2017), (Krack and Gross, 2019)] etc, which are quite a time – consuming procedures in the time domain.

Another application of HBM which has not been investigated adequately in the literature is to obtain the stability plot of a system under parametric excitation. According to Eq. (2.20), on the borders of stability there exist periodic responses; hence, it is quite convenient to implement HBM and find the corresponding transition curves (already explained in chapter 1). To proceed, consider a linear homogenous dynamical system including a T – periodic coefficient $K(t)$ by the following general form:

$$[M]\{\ddot{r}\}+[C]\{\dot{r}\}+\left[K+K(t)\right]\{r\}=0 \tag{2.29}$$

Here $K(t)$ is a time – varying stiffness which represents the parametric excitation and has a sinusoidal form as $K_0 + K_p \cos \eta t$. According to Eq. (2.20), there are periodic solutions of linear dynamic systems which are T or $2T$ periodic. Considering these periodic solutions and applying Fourier series, each coordinate of the system in Eq. (2.29) could be written as follows (Rand, 2014):

$$r_i = \sum_{z=0,1,2,\dots}^{N_h} \left(a_{iz} \sin \frac{z\eta t}{2} + b_{iz} \cos \frac{z\eta t}{2} \right), \tag{2.30}$$

where the T and $2T$ periodic responses are the main components associated with the even and odd indices z in Eq. (2.30). In detail $z = 1$ and $z = 2$ correspond to periodic responses of periods $2T$ and T respectively. Here, N_h designates the number harmonics on which the Fourier series is truncated. By stacking all the r_i in a column vector, substituting it in Eq. (2.29), and balancing the resultant equations according to each frequency content (harmonic), the following algebraic equation would be derived:

$$[J]\{A\}=0\ , \tag{2.31}$$

where $[J]$ is the Jacobian matrix given and $\{A\}$ is the vector of the sinusoidal amplitudes $\{a_z\}$ and $\{b_z\}$. A detailed expression of $[J]$ is given in Appendix B. It must be pointed out that to obtain the transition curve using HBM, the Jacobian matrix $[J]$ must contain unknown parameter(s). This parameter could be chosen optionally and here it is considered as a function of η. For a non – trivial solution of Eq. (2.31) the determinant of $[J]$ must be equated to zero (Rand, 2014). Doing so, the Transition Curves corresponding to the T and $2T$ periodic responses would be acquired.

Expressing the coordinates as Eq. (2.30) results in transition curves that encompass unstable/unbounded responses due to Primary parametric and Simple resonances. However, these frequency components are inadequate to predict the unstable zones due to Combination Parametric resonances. To be able to find the transition curves corresponding to such instabilities, the frequency contents of Eq. (2.30) must be modified. According to what has already been pointed out in chapter 1, the instabilities caused by Combination Parametric resonance contain responses with two incommensurable frequency components like ω_1 and ω_2 which have the following characteristic:

$$\omega_1 + \omega_2 = \eta \tag{2.32}$$

Expanding each coordinate by:

$$r_i = \sum_{z=0,1,2,\dots}^{N_{h1}} \left(a_{iz} \sin\frac{z\eta t}{2} + b_{iz} \cos\frac{z\eta t}{2} \right) + \sum_{s=0,1,2,\dots}^{N_{h2}} \left(c_{is} \sin s\omega_1 t + d_{is} \cos s\omega_2 t \right), \tag{2.33}$$

and following the same procedure as before, an algebraic equation similar to Eq. (2.31) would be obtained. The difference here is that the Jacobian matrix is a function of ω_1 or ω_2 in addition to η. Since the number of unknowns has increased to two, it is necessary to have another equation as well as $|J| = 0$. According to (W. szemplii~iska-stupnicka, 1978), the additional equation could be provided by equating the determinant of the highest minor of $[J]$, denoted by $[J]_m$, to zero. Therefore, the following equations must be solved simultaneously to find the corresponding transition curves:

$$\begin{aligned} |J| &= 0 \\ |J|_m &= 0 \end{aligned} \tag{2.34}$$

2.3.1 Case study: 1-Dof mass – spring – damper model

In this section, the computation of the Transition Curves using HBM is taken into account. The simple mass – spring – damper depicted in Figure 3 whose governing equations of motion given by Eq. (2.21) is adopted as the case study.

To proceed with HBM, first the response of the system x_1 must be expressed in terms of the desired harmonics. As mentioned in section 2.3, the responses on the border of stability or transition curves are periodic with T or $2T$. For the current system the $T = 2\pi/\eta$. To obtain the transition curves, the response of the system must be expressed by the T and $2T$ periodic responses and their harmonics using the Fourier series. Using Eq. (2.30), the T and $2T$ periodic responses and their harmonics are expressed respectively by the x_{1_T} and $x_{1_{TT}}$ as follows:

$$\begin{aligned} x_{1_T} &= \sum_{z=0,2,4} \left(a_z \sin\frac{z\eta t}{2} + b_z \cos\frac{z\eta t}{2} \right) \\ &= b_0 + a_2 \sin(\eta t) + b_2 \cos(\eta t) + a_4 \sin(2\eta t) + b_4 \cos(2\eta t) \end{aligned} \tag{2.35}$$

$$\begin{aligned} x_{1_{TT}} &= \sum_{z=1,3} \left(a_z \sin\frac{z\eta t}{2} + b_z \cos\frac{z\eta t}{2} \right) \\ &= a_1 \sin(\frac{\eta t}{2}) + b_1 \cos(\frac{\eta t}{2}) + a_3 \sin(\frac{3\eta t}{2}) + b_3 \cos(\frac{3\eta t}{2}) \end{aligned} \tag{2.36}$$

The reason behind distinguishing the T and $2T$ periodic responses is to specify and indicate their contributions to the computed transition curves. Then Eq. (2.35) and Eq. (2.36) must be substituted in the equations of motion given in Eq. (2.21). For example, the substitution of Eq. (2.35) in Eq. (2.21) results in the following:

$$
\begin{aligned}
&K_1 b_0 + \frac{a_1 k_1}{2} + b_0 k_1 cos(\eta t) + K_1 a_1 cos(\eta t) + K_1 b_1 sin(\eta t) \\
&+ \frac{a_2 k_1}{2} cos(\eta t) + \frac{b_2 k_1}{2} sin(\eta t) - a_1 \alpha \eta m_1 sin(\eta t) - a_1 \eta^2 m_1 cos(\eta t) \\
&- b_1 \eta^2 m_1 sin(\eta t) + b_1 \alpha \eta m_1 cos(\eta t) + K_1 b_1 \beta \eta cos(\eta t) - K_1 a_1 \beta \eta sin(\eta t) \\
&+ 2K_1 b_2 \beta \eta cos(2\eta t) + \frac{b_1 k_1}{2} sin(2\eta t) - 2K_1 a_2 \beta \eta sin(2\eta t) + K_1 b_2 sin(2\eta t) \\
&+ K_1 a_2 cos(2\eta t) + 2b_2 \alpha \eta m_1 cos(2\eta t) - 4a_2 \eta^2 m_1 cos(2\eta t) + \frac{a_1 k_1}{2} cos(2\eta t) \\
&- 4b_2 \eta^2 m_1 sin(2\eta t) - 2a_2 \alpha \eta m_1 sin(2\eta t) + \frac{a_2 k_1}{2} cos(3\eta t) + \frac{b_2 k_1}{2} sin(3\eta t) = 0
\end{aligned}
\tag{2.37}
$$

Then, by balancing the resultant equations based on the frequency components used in Eq. (2.35) and Eq. (2.36), a set of algebraic equations would be obtained. Using the matrix – vector compact form, the resultant equation could be expressed as follows:

$$
\left[J_T\right]\begin{Bmatrix} b_0 \\ a_2 \\ b_2 \\ a_4 \\ b_4 \end{Bmatrix} = 0 \ , \tag{2.38}
$$

$$
\left[J_{TT}\right]\begin{Bmatrix} a_1 \\ b_1 \\ a_3 \\ b_3 \end{Bmatrix} = 0 \tag{2.39}
$$

And, the Jacobian matrix corresponding to the T and $2T$ periodic are respectively as follows:

$$J_T = \begin{bmatrix} K_1 & 0 & \frac{k_1}{2} & 0 & -\frac{k_1}{2} \\ 0 & -m_1\eta^2 + K_1 & -K_1\beta\eta - \alpha\eta m_1 & \frac{k_1}{2} & 0 \\ k_1 & K_1\beta\eta + \alpha\eta m_1 & -m_1\eta^2 + K_1 & 0 & \frac{k_1}{2} \\ 0 & \frac{k_1}{2} & 0 & -4m_1\eta^2 + K_1 & -2K_1\beta\eta - 2\alpha\eta m_1 \\ 0 & 0 & \frac{k_1}{2} & 2K_1\beta\eta + 2\alpha\eta m_1 & -4m_1\eta^2 + K_1 \end{bmatrix} \tag{2.40}$$

$$J_{TT} = \begin{bmatrix} K_1 - \frac{k_1}{2} - \frac{\eta^2 m_1}{4} & -\frac{K_1\beta\eta}{2} - \frac{\alpha\eta m_1}{2} & \frac{k_1}{2} & 0 \\ \frac{K_1\beta\eta}{2} + \frac{\alpha\eta m_1}{2} & K_1 + \frac{k_1}{2} - \frac{\eta^2 m_1}{4} & 0 & \frac{k_1}{2} \\ \frac{k_1}{2} & 0 & K_1 - \frac{9\eta^2 m_1}{4} & -\frac{3K_1\beta\eta}{2} - \frac{3\alpha\eta m_1}{2} \\ 0 & \frac{k_1}{2} & \frac{3K_1\beta\eta}{2} + \frac{3\alpha\eta m_1}{2} & K_1 - \frac{9\eta^2 m_1}{4} \end{bmatrix} \tag{2.41}$$

As explained below Eq. (2.31), for non – trivial solutions, the determinant of the Jacobian matrix must be equated to zero. This results in the computation of the transition curves. For this study, the frequency of the parametric excitation η is considered to be unknown. Hence, by solving the determinants of the Jacobian matrices give in Eq. (2.40) and Eq. (2.41), the values of η at which non-trivial solutions of Eq. (2.38) and Eq. (2.39) exist would be computed.

Recalling that in section 2.2.1 k_1 was adopted as a control parameter, by solving the determinants of J_T and J_{TT} for different values of k_1 and collecting the computed values of η, a stability plot depicted in Figure 5 depicting the transition curves is acquired. According to this figure, the transition curves obtained using HBM, accurately locate the unstable regions computed by the Floquet theory designated by the black dots. As shown in Figure 5, solving the determinant of J_T corresponding to the T periodic responses result in the transition curves highlighting the area of instability caused by simple resonance. On the other hand, the computation of the determinant of J_{TT} corresponding to the $2T$ periodic responses results in the transition curves, shown by purple dots, which encloses the unstable region due to the Primary Parametric resonances. It must be mentioned that in

Figure 5, 'TCs' stands for Transition Curves. It is worth mentioning unlike the results from Floquet Theory, HBM detects the instabilities via the transition curves where the responses are bounded and periodic. The reason is that HBM considers the response to be purely periodic therefore, it is unable to capture the unbounded responses inside the unstable regions.

The procedure of computing the transition curve corresponding to the instability due to the combination parametric resonance is quite similar to the current case while an extra equation as indicated by Eq. (2.34) in section 2.3 must be taken into account. In addition, as mentioned in the previous chapter, to have instabilities due to the combination parametric resonance, the system must have at least two Dof or higher. This will be explained later in this chapter.

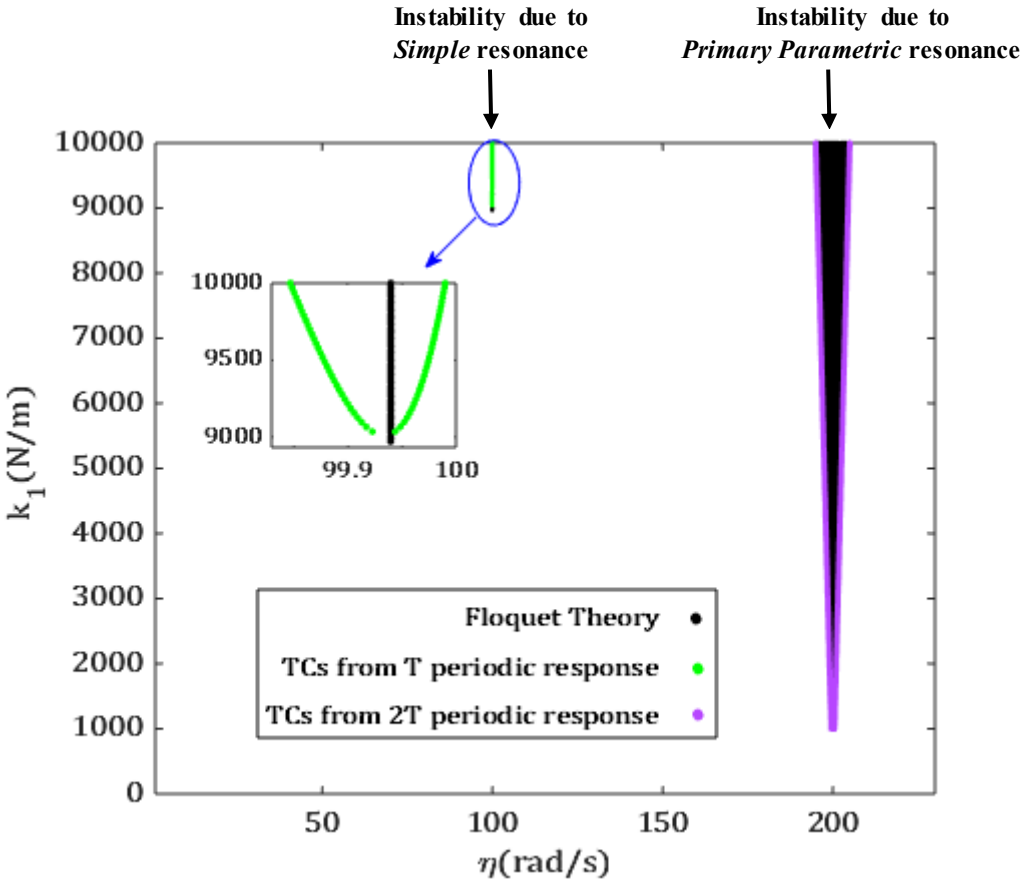

Figure 5: Stability plot of a parametrically excited 1-Dof mass – spring – damper model containing the transition curves obtained by implementing HBM

2.4 Hill's method

In section 2.2 using Floquet theory, the mathematical formulation to perform the stability analysis of a linear homogenous dynamical system with periodic coefficients has been given in the time domain. It has been shown that the modulus of the Floquet multipliers determines whether the response of the system grows or decays over time. Since Floquet theory studies the stability in the time domain, analyzing systems with high numbers of Dof would be considerably time – consuming. Therefore, Hill's method, as an alternative to Floquet theory, which investigates the stability problem in the frequency domain is recommended. This method is based on HBM and by considering a sufficient number of Fourier coefficients, the stability of the system could be well determined.

To apply this method to a dynamical system with a periodic parameter presented by Eq. (2.29), first, the perturbing term in Eq. (2.3) in section 2.2 is expressed in the Floquet Form (Lazarus and Thomas, 2010) (Nayfeh A. H., 1993):

$$p(t) = \mathrm{X}(t)e^{\gamma t} \ , \tag{2.42}$$

where γ is called 'Floquet exponent' and $\mathrm{X(t)}$ is a periodic vector in which $\mathrm{X(t)} = \mathrm{X(t+T)}$. According to this equation, the value of the Floquet exponent determines whether the solution grows or decays via time. To implement Hill's method, a linear homogeneous dynamical system with periodic coefficient as Eq. (2.29) in section 2.3 is taken into account. For the stability analysis, a solution of Eq.(2.29), $r(t)_p$, is perturbed using Eq. (2.42):

$$r(t) = r_p(t) + p(t) \tag{2.43}$$

Substituting Eq. (2.43) into Eq. (2.29):

$$E(r_p) + E(p)e^{\gamma t} = 0 \ , \tag{2.44}$$

where $E(r_p)$ and $E(p)$ are defined as follows:

$$\begin{aligned} E(r_p) &= M\ddot{r}_p + C\dot{r}_p + (K + K(t))r_p \\ E(p) &= M\ddot{\mathrm{X}} + C\dot{\mathrm{X}} + (K + K(t) + M\gamma^2)\mathrm{X} + (2M\dot{\mathrm{X}} + C\mathrm{X})\gamma \end{aligned} \tag{2.45}$$

It must be reminded that $K(t) = K_0 + K_p \cos \eta t$ Since r_p is considered to be a solution of the Eq. (2.29), hence $E(r_p) = 0$. As pointed out earlier, X is a periodic function and therefore could be expressed by Fourier series. For this system, X corresponds to periodic responses with T and $2T$ periods (Eq. (2.20), section 2.2):

$$\mathrm{X}_i = \sum_{z=0,1,2,\ldots}^{N_h} \left(a_{iz} \sin \frac{z\eta t}{2} + b_{iz} \cos \frac{z\eta t}{2} \right) \tag{2.46}$$

Collecting all $\mathrm{X_i}$ in a column vector, substituting it into Eq. (2.44), and balancing the resultant equations by the same harmonic components, the following compact form algebraic equation would be obtained (Detroux *et al.*, 2015):

$$\left(\left(\gamma^2 \Gamma_2 + \gamma \Gamma_1 + \mathrm{J} \right) u \right) e^{\gamma t} = 0 \tag{2.47}$$

The formation of Eq. (2.47) is given in APPENDIX C. In Eq. (2.47), the vector u is vector of the sinusoidal coefficients $\vec{a}_z$ and $\vec{b}_z$, matrix J is Jacobian matrix and matrices Γ_1 and Γ_2 are defined as follows:

$$\Gamma_1 = \begin{bmatrix} [C] & & & \\ & \ddots & & \\ & & \begin{bmatrix} [C] & -2\Omega_z [M] \\ 2\Omega_z [M] & [C] \end{bmatrix}_z & \\ & & & \ddots \end{bmatrix}_{n(2N_h+1)\times n(2N_h+1)} \tag{2.48}$$

$$\Gamma_2 = diag\left([M], \ldots, [M] \right)_{n(2N_h+1)\times n(2N_h+1)}$$

In Eq. (2.48) N_h and n indicate respectively the number of harmonics given in Eq. (2.46) and the number of Dof of the system. The vector u and the matrices J, $\mathrm{X_1}$ and $\mathrm{X_2}$ are all presented in APPENDIX C. In Eq. (2.48) Ω_z respresents the z^{th} frequency of the Fourier series in Eq. (2.46); for instance $\Omega_1 = \eta/2$ or $\Omega_2 = \eta$. For non – trivial solution of Eq. (2.46) the determinant of the inner parentheses must be equated to zero:

$$\left| \gamma^2 \Gamma_2 + \gamma \Gamma_1 + \mathrm{J} \right| = 0 \tag{2.49}$$

Eq. (2.49) is the characteristic equation of the following eigenvalue problem (Detroux *et al.*, 2015):

$$\Lambda\vec{v} = \gamma\vec{v} \tag{2.50}$$

where this equation shows that the Floquet exponents γ computed by solving Eq. (2.49) are the eigenvalues of matrix Λ which has the following form:

$$\Lambda = \begin{bmatrix} -\Gamma_2^{-1}\Gamma_1 & -\Gamma_2^{-1}J \\ \mathbb{I} & 0 \end{bmatrix}_{2n(2N_h+1)\times 2n(2N_h+1)} \tag{2.51}$$

Hence, instead of solving Eq. (2.49) to obtain the Floquet Exponents γ, one can simpliy compute the eigenvalues of the matrix Λ:

$$\gamma = eig(\Lambda) \tag{2.52}$$

According to (Detroux *et al.*, 2015), among all the $2n(2N_h + 1)$ numbers of γ, $2n$ of them with the *smallest imaginary part in modulus,* determine the stability status of the perturbing term in Eq. (2.42). Doing so, the stability plot containing the unstable regions would be obtained. This will be further discussed and demonstrated later in this chapter.

2.4.1 Case study: 1-Dof mass – spring – damper model

In this section, the implementation of Hill's method to obtain the stability plot of the model shown in Figure 3, is explained.

By perturbing the trivial solution of Eq. (2.21) in section 2.2.1 i.e. $x_p = 0$ by Floquet Form given in Eq. (2.42) and substituting it in Eq. (2.21), the following equation would be obtained:

$$E(x_p = 0) + E(X)e^{\gamma t} = 0 \tag{2.53}$$

Where:

$$E(x_p = 0) = 0 \tag{2.54}$$

$$E(X) = m_1\ddot{X} + C\dot{X} + \left(m_1\gamma^2 + K_{v1}(t)\right)X + \left(CX + 2m_1\dot{X}\right)\gamma \tag{2.55}$$

Considering the T and $2T$ periodic responses and their harmonics (please take a look at Eq. (2.35) & Eq. (2.36)), the periodic vector $X(t)$ can be expressed as the following:

$$X(t) = \sum_{z=0,1,2,\ldots}^{N_h} \left(a_z \sin\frac{z\eta t}{2} + b_z \cos\frac{z\eta t}{2} \right) = b_0 + a_1 \sin\frac{\eta t}{2} + b_1 \cos\frac{\eta t}{2} + a_2 \sin\eta t + b_2 \cos\eta t + a_3 \sin\frac{3\eta t}{2} + b_3 \cos\frac{3\eta t}{2} + a_4 \sin 2\eta t + b_4 \cos 2\eta t \tag{2.56}$$

Substituting Eq. (2.56) in Eq. (2.55) and following the procedure explained in APPENDIX C, results in the following compact form equation:

$$\left(\left(\gamma^2 \mathrm{X}_2 + \gamma \mathrm{X}_1 + \mathrm{J} \right) u \right) e^{\gamma t} = 0 \tag{2.57}$$

To determine whether the perturbing term grows or decays with time, it is required to compute the values of the γ which are known as 'Floquet Exponents'.

Here, $N_h = 4$ and the number of Dofs denoted by n is equal to 1. Hence, the matrices in Eq. (2.57) have the dimension of 9 according to Eq. (2.48)). The matrices X_1, X_2 and J for this specific system are as follows:

$$\mathrm{X}_1 = \begin{bmatrix} \mathrm{m}_1 & & & & & & & & \\ & \mathrm{m}_1 & & & & & & & \\ & & \mathrm{m}_1 & & & & & & \\ & & & \mathrm{m}_1 & & & & & \\ & & & & \mathrm{m}_1 & & & & \\ & & & & & \mathrm{m}_1 & & & \\ & & & & & & \mathrm{m}_1 & & \\ & & & & & & & \mathrm{m}_1 & \\ & & & & & & & & \mathrm{m}_1 \end{bmatrix}$$

$$\mathrm{X}_2 = \begin{bmatrix} \mathrm{K}_1\beta + \alpha\mathrm{m}_1 & & & & & & & & \\ & \mathrm{K}_1\beta + \alpha\mathrm{m}_1 & -\eta\mathrm{m}_1 & & & & & & \\ & \eta\mathrm{m}_1 & \mathrm{K}_1\beta + \alpha\mathrm{m}_1 & & & & & & \\ & & & \mathrm{K}_1\beta + \alpha\mathrm{m}_1 & -2\eta\mathrm{m}_1 & & & & \\ & & & 2\eta\mathrm{m}_1 & \mathrm{K}_1\beta + \alpha\mathrm{m}_1 & & & & \\ & & & & & \mathrm{K}_1\beta + \alpha\mathrm{m}_1 & -3\eta\mathrm{m}_1 & & \\ & & & & & 3\eta\mathrm{m}_1 & \mathrm{K}_1\beta + \alpha\mathrm{m}_1 & & \\ & & & & & & & \mathrm{K}_1\beta + \alpha\mathrm{m}_1 & -4\eta\mathrm{m}_1 \\ & & & & & & & 4\eta\mathrm{m}_1 & \mathrm{K}_1\beta + \alpha\mathrm{m}_1 \end{bmatrix}$$

$$
J = \begin{bmatrix}
K_1 & & & \frac{k_1}{2} & & & & & & \\
 & K_1 - \frac{k_1}{2} - \frac{m_1\eta^2}{4} & -\frac{K_1\beta\eta + \alpha\eta m_1}{2} & & & \frac{k_1}{2} & & & & \\
 & \frac{K_1\beta\eta + \alpha\eta m_1}{2} & K_1 + \frac{k_1}{2} - \frac{\eta^2 m_1}{4} & & & & \frac{k_1}{2} & & & \\
 & & & -m_1\eta^2 + K_1 & -K_1\beta\eta - \alpha\eta m_1 & & & \frac{k_1}{2} & & \\
k_1 & & & K_1\beta\eta + \alpha\eta m_1 & -m_1\eta^2 + K_1 & & & & & \frac{k_1}{2} \\
 & \frac{k_1}{2} & & & & K_1 - \frac{9\eta^2 m_1}{4} & -\frac{3K_1\beta\eta + 3\alpha\eta m_1}{2} & & & \\
 & & \frac{k_1}{2} & & & \frac{3K_1\beta\eta + 3\alpha\eta m_1}{2} & K_1 - \frac{9\eta^2 m_1}{4} & & & \\
 & & & \frac{k_1}{2} & & & & -4m_1\eta^2 + K_1 & -2K_1\beta\eta - 2\alpha\eta m_1 & \\
 & & & & \frac{k_1}{2} & & & 2K_1\beta\eta + 2\alpha\eta m_1 & -4m_1\eta^2 + K_1 &
\end{bmatrix}
$$

For non – trivial soltuions of Eq. (2.57), the determinant of the $(\gamma^2 X_2 + \gamma X_1 + J)$ must be equated to zero which resutls in the computation of the Floquet exponents γ. However, as explained in section 2.4 (please refer to Eq. (2.50)), a much simpler way is to obtain the Floquet exponents γ is to compute the eigenvalues of the matrix Λ given by Eq. (2.51). In fact, the eigenvalues of the matrix Λ are the Floquet exponents.

By examining the real parts of the $2n$ eigenvalues with the smallest imaginary parts (please read the criteria explained below Eq. (2.52)) for each pair of (k_1, η), the stability plot shown in Figure 6 would be obtained. As mentioned before, n is the number of Dofs in which for the current system is equal to 1.

According to Figure 6, the results from Hill's method highlight the unstable/unbounded responses shown by the blue area. To evaluate the accuracy of Hill's method, the results from HBM i.e. Transition Curves, which are already approved by Floquet Theory in Figure 5, are adopted. As depicted in Figure 6, Hill's method perfectly captures the unbounded responses inside the area of the Transition Curves computed by HBM.

It is worth noting that the existence of the exponential part in the Floquet Form (Eq. (2.42)), allows Hill's method to detect the diverging responses corresponding to the frequency components fed into. The similarity of the results from Hill's method and Floquet theory is due to this point.

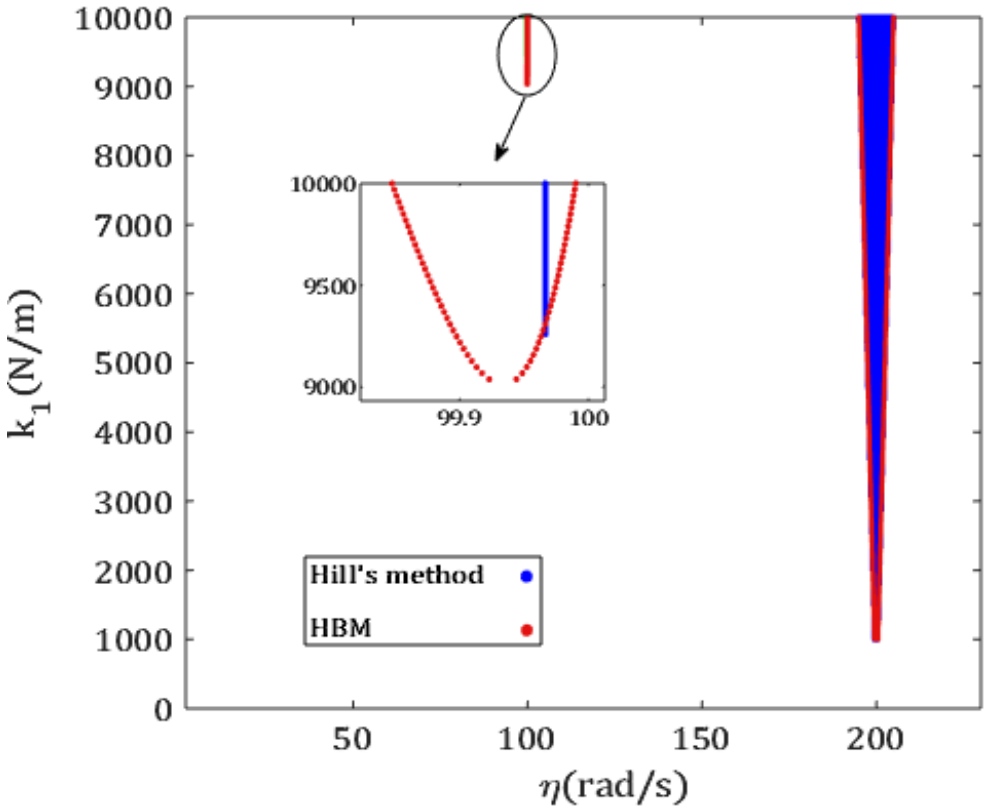

Figure 6: Stability plot of a parametrically excited 1-Dof mass – spring – damper model obtained by implementing Hill's method

To demonstrate the procedure of selecting the proper Floquet exponents to study the stability using Hill's method, the eigenvalues of the matrix Λ when $k_1 = 6000(\mathrm{N/m})$ and $\eta = 2\omega_n = 200(\mathrm{rad/s})$ are computed:

$$\gamma = \begin{bmatrix} -0.1+500i \\ -0.1-500i \\ -1.6+300i \\ -1.6-3.00i \\ 1.4+300i \\ 1.4-300i \\ -1.6+100i \\ -1.6-100i \\ 1.4+100i \\ 1.4-100i \\ -0.1+400i \\ -0.1-400i \\ -1.6+200i \\ -1.6-200i \\ 1.4+200i \\ 1.4-200i \\ -1.6 \\ 1.4 \end{bmatrix} \tag{2.58}$$

To specify the stability whether the system is stable or unstable when $k_1 = 6000(\mathrm{N/m})$ and $\eta = 200(\mathrm{rad/s})$, first, the $2n$ eigenvalues with the smallest imaginary must be selected. According to Eq. (2.58), the last two values highlighted by red are adopted. Since one of them is positive, the perturbing will grow exponentially which results in an unstable/unbounded response of the system.

2.5 Perturbation method

The Perturbation method is an analytical method to solve the linear and weakly nonlinear and also weakly damped governing equations of motion approximately (Nayfeh, 2000). This method is built based on a small parameter known as 'Perturbation Parameter', usually represented by ϵ, in which the response of the system is approximated and expanded based on. In fact, an equation in the perturbation form has two independent parameters: Time and Perturbation Parameter. This method here is mainly adopted to make a comparison with HBM in terms of mathematical calculations and applicability to find the transition curves.

To apply this method, a single DOF homogenous equation of motion of a linear dynamical system with a periodic coefficient is taken into account:

$$m\ddot{x} + c\dot{x} + \left(k + k_0 \cos \eta t\right) x = 0 \tag{2.59}$$

In this method, all the terms except the acceleration and displacement with constant coefficients are considered perturbing terms. Because of this, their coefficients are rescaled using the perturbation parameter ϵ. By introducing the following parameters:

$$\begin{aligned} k_0 &= \epsilon \hat{k}_0 \\ c &= \epsilon \hat{c} \ , \end{aligned} \tag{2.60}$$

and by substituting Eq. (2.60) into Eq. (2.59):

$$m\ddot{x} + \epsilon \hat{c}\dot{x} + \left(k + \epsilon \hat{k}_0 \cos \eta t\right) x = 0 \tag{2.61}$$

To be able to obtain the transition curves, first, the Method of Straightforward expansion is utilized where the cause(s) of non-uniformity of the response x expanded in terms of the ϵ and t will be clarified**.** This information would be used in applying the Method of Multiple Scales to obtain the transition curves.

2.5.1 Straight Forward Expansion

First, the response of Eq. (2.61) is expanded in terms of ϵ and t (Nayfeh A. H., 1993):

$$x\left(\epsilon; t\right) = x_0\left(t\right) + \epsilon x_1\left(t\right) + O\left(\epsilon^2\right) \tag{2.62}$$

Eq. (2.62) is a first – order expansion and terms of the order ϵ^2 are disregareded. Here, x_0 is a linear solution of the equation of motion without perturbed terms (damping and periodic stiffness) while x_1 is the correction added due to the presence of the perturbed terms (Nayfeh A. H., 1995). Substituting Eq. (2.62) in Eq. (2.61) and neglecting the higher – order terms, results in:

$$m\ddot{x}_0 + kx_0 + \epsilon\left(\ddot{x}_1 + kx_1 + \hat{c}\dot{x}_0 + \hat{k}_0 x_0 \cos \eta t\right) + O\left(\epsilon^2\right) = 0 \tag{2.63}$$

By equating each power of ϵ to zero, the following differential equations are obtained:

$$m\ddot{x}_0 + kx_0 = 0 \rightarrow x_0 = A_1 \cos \omega_{nf} t + B_1 \sin \omega_{nf} t \tag{2.64}$$

$$m\ddot{x}_1 + kx_1 = -\hat{c}\dot{x}_0 - \hat{k}_0 x_0 \cos \eta t, \tag{2.65}$$

where the answer to Eq. (2.64) is given in front of it where $\omega_{nf} = \sqrt{k/m}$. Then inserting x_0 from Eq. (2.64) in Eq. (2.65) yields the following:

$$\begin{aligned} \ddot{x}_1 + \omega_{nf}^2 x_1 = & -\frac{\hat{c}\omega_{nf}}{m}\left(-A_1 \sin \omega_{nf} t + B_1 \cos \omega_{nf} t\right) \\ & -\frac{\hat{k}_0}{m}\begin{pmatrix} A_1\left(\cos\left(\omega_{nf} + \eta\right)t + \cos\left(\omega_{nf} - \eta\right)t\right) \\ +B_1\left(\sin\left(\omega_{nf} + \eta\right)t + \sin\left(\omega_{nf} - \eta\right)t\right) \end{pmatrix} \end{aligned} \tag{2.66}$$

and the solution of Eq. (2.66) would be as follows:

$$\begin{aligned} x_1 = & -\frac{\hat{c}}{2m} t\left(A_1 \cos \omega_{nf} t + B_1 \sin \omega_{nf} t\right) \\ & -\frac{\hat{k}_0}{m}\begin{pmatrix} A_1\left(\frac{1}{\left(2\omega_{nf} + \eta\right)\eta}\cos\left(\omega_{nf} + \eta\right)t + \frac{1}{\left(2\omega_{nf} - \eta\right)\eta}\cos\left(\omega_{nf} - \eta\right)t\right) \\ +B_1\left(-\frac{1}{\left(2\omega_{nf} + \eta\right)\eta}\sin\left(\omega_{nf} + \eta\right)t + \frac{1}{\left(2\omega_{nf} - \eta\right)\eta}\sin\left(\omega_{nf} - \eta\right)t\right) \end{pmatrix} \end{aligned} \tag{2.67}$$

The expansion of the response given in Eq. (2.62) fails due to the presence of the subsequent terms in Eq. (2.67):

a) A Secular Term: the term multiplied by t and grows with time
b) A Small devisor: the term $\left(2\omega_{nf} - \eta\right)\eta$ at the denominator which produces resonance when $\eta = 2\omega_{nf}$

In the following section, the application of the multiple scales method, to compute the transition curves is investigated.

2.5.2 Method of Multiple Scales (MMS)

According to this approach, the response of the system is a function of multiple time scales i.e. fast and slow (Nayfeh A. H., 1993). Hence, it is possible to expand the response in terms of different time scales as well as the perturbation parameter ϵ. To do so, first, the following time scales are introduced:

$$\begin{aligned} T_0 &= t \\ T_1 &= \epsilon t \ , \end{aligned} \tag{2.68}$$

where T_0 and T_1 introduce respectively fast and slow time scales. Then, the response x is expanded as the following first – order expansion:

$$x(\epsilon; T_0, T_1) = x_0(T_0, T_1) + \epsilon x_1(T_0, T_1) + \dots \tag{2.69}$$

Then, by expressing the time derivatives in terms of the new time scales the ordinary differential equation would be transformed into a partial differential equation:

$$\begin{aligned} \frac{d}{dt} &= D_0 + \epsilon D_1 + \dots \\ \frac{d^2}{dt^2} &= D_0^2 + 2\epsilon D_0 D_1 + \dots , \end{aligned} \tag{2.70}$$

where $D_i = \partial / \partial T_i$. Substituting Eq. (2.69) and Eq. (2.70) in Eq. (2.61) results in the following partial differential equation:

$$mD_0^2 x_0 + kx_0 + \epsilon\left(mD_0^2 x_1 + kx_1 + 2mD_0 D_1 x_0 + \hat{c} D_0 x_0 + \hat{k}_0 \cos \eta T_0 \, x_0\right) = 0 \tag{2.71}$$

Following the same procedure as before and equating each power of ϵ to zero results in the subsequent equations:

$$D_0^2 x_0 + \omega_{nf}^2 x_0 = 0 \rightarrow x_0 = A_1(T_1)\cos \omega_{nf} T_0 + B_1(T_1)\sin \omega_{nf} T_0 \tag{2.72}$$

$$mD_0^2 x_1 + kx_1 = -2mD_0 D_1 x_0 - \hat{c} D_0 x_0 - \hat{k}_0 x_0 \cos \eta T_0 \tag{2.73}$$

Replacing x_0 from Eq. (2.72) in Eq. (2.73), yields the following equation for x_1:

$$
\begin{aligned}
&D_0^2 x_1 + \omega_{nf}^2 x_1 = \\
&-2\omega_{nf}\left(-\frac{\partial A_1}{\partial T_1}\sin\omega_{nf}T_0 + \frac{\partial B_1}{\partial T_1}\cos\omega_{nf}T_0\right) \\
&-\frac{\hat{c}\omega_{nf}}{m}\left(-A_2\sin\omega_{nf}T_0 + B_2\cos\omega_{nf}T_0\right) \\
&-\frac{\hat{k}_0}{2m}\begin{pmatrix} A_1\left(\cos\left(\omega_{nf}+\eta\right)T_0 + \cos\left(\omega_{nf}-\eta\right)T_0\right) \\ +B_1\left(\sin\left(\omega_{nf}+\eta\right)T_0 + \sin\left(\omega_{nf}-\eta\right)T_0\right)\end{pmatrix}
\end{aligned}
\tag{2.74}
$$

Comparing Eq. (2.74) and Eq. (2.66), it is evident that the response x_1 will contain secular and small divisor terms. In detail, the expressions multiplied by $-2\omega_{nf}$ and $\hat{c}\omega_{nf}/m$ generate secular terms while the cosine and sine terms containing $\omega_{nf}-\eta$ result in small divisors.

According to Lindstedt – Poincare method, the perturbation terms may change the natural frequency of the system, therefore, it could be expanded in terms of the perturbing parameter (Nayfeh A. H., 1993). Applying this procedure, the following would be obtained:

$$
\omega_{nf}^2 = \omega_0^2 + \epsilon\omega_1^2 + O\left(\epsilon^2\right), \tag{2.75}
$$

where ω_0 is the linear natural frequency. Since the aim here is to study the system around the parametric resonance and according to the small divisor obtained by straightforward expansion, the resonance occurs at $\omega_{nf} = \eta/2$. Therefore, ω_0 is considered to be equal to $\eta/2$. The objective here is to obtain ω_1. Substituting Eq. (2.75) in Eq. (2.61) results in the following:

$$
\begin{aligned}
&D_0^2 x_0 + \omega_0 x_0 \\
&+\epsilon\left(D_0^2 x_1 + \omega_0^2 x_1 + 2D_0 D_1 x_0 + \frac{\hat{c}}{m}D_0 x_0 + \omega_1^2 x_0 + \frac{\hat{k}_0}{m}x_0\cos\eta T_0\right) = 0
\end{aligned}
\tag{2.76}
$$

Equating the coefficients of each power of ϵ to zero yields the following (taking into account that $\omega_0 = \eta/2$):

$$
D_0^2 x_0 + \frac{\eta^2}{4}x_0 = 0 \rightarrow x_0 = A_1\left(T_1\right)\cos\frac{\eta}{2}T_0 + B_1\left(T_1\right)\sin\frac{\eta}{2}T_0 \tag{2.77}
$$

$$
\begin{aligned}
&D_0^2 x_1 + \frac{\eta^2}{4} x_1 \\
&= -\eta\left(-\frac{\partial A_1}{\partial T_1}\sin\frac{\eta}{2}T_0 + \frac{\partial B_1}{\partial T_1}\cos\frac{\eta}{2}T_0 \right) \\
&-\frac{\hat{c}\eta}{2m}\left(-A_1\sin\frac{\eta}{2}T_0 + B_1\cos\frac{\eta}{2}T_0 \right) \\
&-\omega_1^2\left(A_1\cos\frac{\eta}{2}T_0 + B_1\sin\frac{\eta}{2}T_0 \right) \\
&-\frac{\hat{k}_0}{2m}\left(A_1\left(\cos\frac{3\eta}{2}T_0 + \cos\frac{\eta}{2}T_0 \right) + B_1\left(\sin\frac{3\eta}{2}T_0 - \sin\frac{\eta}{2}T_0 \right) \right)
\end{aligned}
\tag{2.78}
$$

It is observable from Eq. (2.78) that by implementing Eq. (2.75) all the small divisor generator terms are converted to secular term generators. To have a uniform expansion of Eq. (2.69), one must eliminate all the expressions multiplied by $\sin\frac{\eta}{2}T_0$ and $\cos\frac{\eta}{2}T_0$ which gives rise to secular terms in the x_1 (Nayfeh A. H., 1993). Doing so, results in the subsequent equation:

$$
\begin{aligned}
&\left(\eta\frac{\partial A_1}{\partial T_1} + \frac{\hat{c}\eta}{2m}A_1 + \left(\frac{\hat{k}_0}{2m} - \omega_1^2 \right) B_1 \right)\sin\frac{\eta}{2}T_0 - \\
&\left(\eta\frac{\partial B_1}{\partial T_1} + \frac{\hat{c}\eta}{2m}B_1 + \left(\frac{\hat{k}_0}{2m} + \omega_1^2 \right) A_1 \right)\cos\frac{\eta}{2}T_0 = 0
\end{aligned}
\tag{2.79}
$$

Equating the coefficients of the sin and cos to zero results in the following first – order differential equations:

$$
\left\{ \dot{X} \right\} = \left[\Delta \right]\left\{ X \right\}, \tag{2.80}
$$

where:

$$
\left\{ \dot{X} \right\} = \begin{Bmatrix} \dfrac{\partial A_1}{\partial T_1} \\ \dfrac{\partial B_1}{\partial T_1} \end{Bmatrix}, \left\{ X \right\} = \begin{Bmatrix} A_1 \\ B_1 \end{Bmatrix}, \left[\Delta \right] = \begin{bmatrix} \dfrac{\hat{c}}{2m} & \dfrac{\hat{k}_0}{2m\eta} - \dfrac{\omega_1^2}{\eta} \\ \dfrac{\hat{k}_0}{2m\eta} + \dfrac{\omega_1^2}{\eta} & \dfrac{\hat{c}}{2m} \end{bmatrix} \tag{2.81}
$$

The general form of the solution of Eq. (2.80) is $\{X\} = \{S\}e^{\lambda T_1}$. Substituting this solution in Eq. (2.80) yields the following eigenvalue problem:

$$\lambda\{S\} = [\Delta]\{S\} \rightarrow [\Delta - \lambda I]\{S\} = 0 \tag{2.82}$$

For non – trivial solutions, $|\Delta - \lambda I| = 0$ that gives λ which are the eigenvalues of Δ:

$$\lambda_{1,2} = \frac{\hat{c}}{2m} \pm \frac{\sqrt{\hat{k}_0^2 - 4m^2\omega_1^4}}{2\eta m} \tag{2.83}$$

As was observed earlier in section 2.2, according to the Floquet theory, on the transition curves the responses are purely periodic. According to Eq. (2.77), x_0 would be purely periodic if the $A_1(T_1)$ and $B_1(T_1)$ are invariant with time. Accordingly, the vector $\{X\} = \begin{Bmatrix} A_1 \\ B_1 \end{Bmatrix}$ given in Eq. (2.81) must be chosen in such a way to become a constant. To this end, it is necessary to equate the eigenvalues in Eq. (2.83) to zero. Doing so and using Eq. (2.60), results in the following:

$$\omega_1^2 = \pm\frac{1}{\varepsilon}\sqrt{\frac{k_0^2 - c^2\eta^2}{4m^2}} \tag{2.84}$$

Substituting Eq. (2.84) in Eq. (2.75), the expression for the natural frequency would be:

$$\omega_{nf}^2 = \frac{\eta^2}{4} \pm \sqrt{\frac{k_0^2 - c^2\eta^2}{4m^2}} \tag{2.85}$$

Using Eq. (2.85) one can compute the Transition Curves in any plane of parameters of interest.

2.5.3 Case study: 1-Dof mass – spring – damper model

As mentioned at the beginning of section 2.5, the Perturbation method is implemented to a single Dof system given by Eq. (2.59). Since the current case study, depicted in Figure 3, is also a single Dof model, the mathematical procedure of applying MMS is completely the same as explained in section 2.5.2. Therefore, Eq. (2.85) can be adopted to compute the Transition Curves.

By neglecting the higher – order terms, Eq. (2.85) for the current system can be rewritten as the following:

$$\omega_n^2 - \frac{\eta^2}{4} \pm \sqrt{\frac{k_1^2 - C_1^2\eta^2}{4m_1^2}} = 0 \tag{2.86}$$

To obtain the transition curves, Eq. (2.86) must be solved numerically. Taking η and $\hat{k}_1$ as the control parameters, the stability plot resulted from MMS implementation is shown in Figure 7.

According to Figure 7, first – order expansion of the response (please refer to Eq. (2.69)) results in transition curves locating the instability due to the parametric resonance. For this study, the results from HBM (denoted by red dots) which were already approved by Floquet Theory are adopted as the reference to examine the preciseness of the transition curves obtained by MMS. As depicted in Figure 7, the accuracy of the transition curves from MMS to specify the unstable zone highly depends on the value of the perturbation parameter ϵ. Here, the transition curves computed by MMS for $\epsilon = 0.1$ is obtained and it is observable that the results computed by MMS overlap perfectly the ones from HBM. It can be implied from the results that that first order expansion of the response using MSM is accurate enough to locate the instabilities due to the primary parametric resonance.

Furthermore, according to Figure 7, the implementation of MMS does not detect the unstable zone due to simple resonance. According to the zoomed view of the first unstable zone, no transition curves are resulted from employing MMS to highlight this region. This deficiency is because in implementing Lindstedt – Poincare method to obtain Eq. (2.75), ω_0 is considered to be equal to $\eta/2$ which is a representative frequency content of the responses due to the parametric resonances. This method will not be investigated anymore for the second case study.

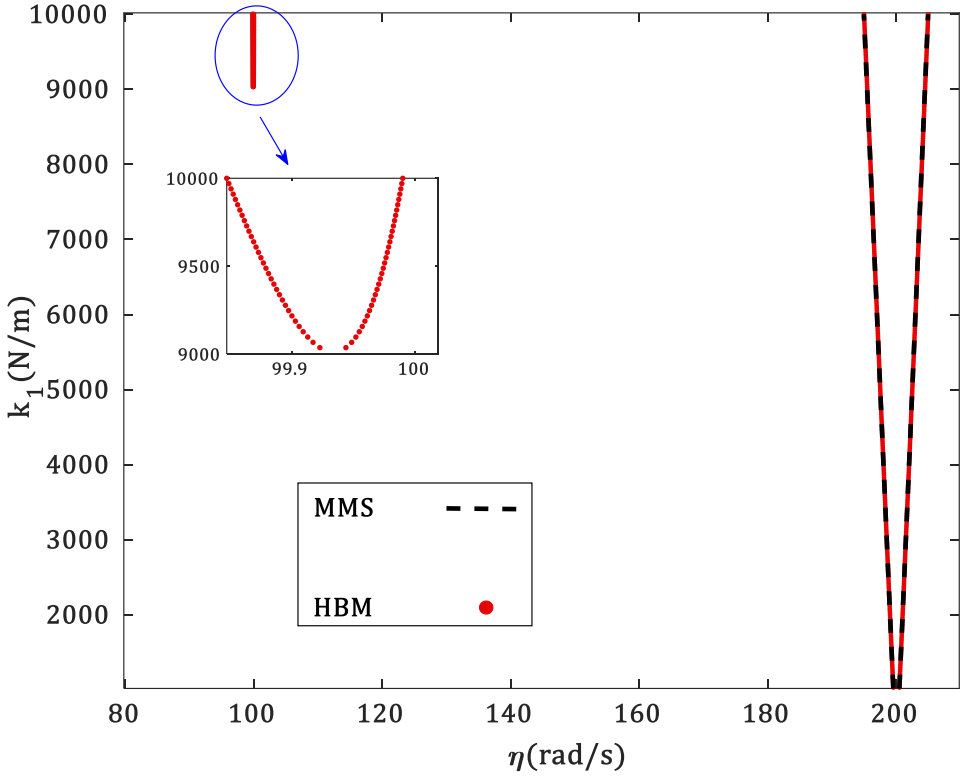

Figure 7: Stability plot of a parametrically excited 1-Dof mass – spring – damper model containing the transition curves obtained by implementing MMS ($\boldsymbol{\epsilon = 0.1}$)

2.6 Jacobian Based Approach (JBA)_Proposed Method

Consider the following general form of the equation of motion of an n–Dof parametrically and externally excited system:

$$[M]\{\ddot{r}\}+[C]\{\dot{r}\}+\left[K+K(t)\right]\{r\}=\{f(t)\} \tag{2.87}$$

Where in Eq. (2.87), $K(t)=K_0+K_p\cos\eta t$ and $\{f(t)\}=\{F_H\}\cos\Omega t$. To implement HBM, the response at each Dof r_i is expressed by the Fourier series in terms of the external force frequency Ω, the T and $2T$ periodics components associted to η and their harmonics:

$$r_i=\sum_{s=0,1,\ldots}^{N_{h1}}\left(b_{is}\sin s\Omega t+a_{is}\cos s\Omega t\right)+\sum_{z=1,\ldots}^{N_{h2}}\left(e_{iz}\sin\frac{z\eta t}{2}+g_{iz}\cos\frac{z\eta t}{2}\right) \tag{2.88}$$

In Eq. (2.88) the odd and even values of N_{h2} respectively correspond to $2T$ and T periodic responses and their harmonics. By collecting all the r_i in Eq. (2.88) in a row column vector, substituting it in Eq. (2.87) and balancing the terms of the same frequency components, yields the subsequent set of algebraic equations:

$$\{R\} = [J]\{U\} - \{F\} \tag{2.89}$$

Eq. (2.89) is called Residual equation and $[J]$, $\{U\}$, $\{F\}$ and {R} are respectively Jacobian matrix, vector of harmonic amplitudes, vector of residuals and forcing vector. It must be noted that the balancing procedure is the same as explained in APPENDIX B. The aim here is to compute the vector $\{U\}$. To do so, the residual $\{R\}$ must be minimized. Considering the residual to be very close to zero one can write:

$$\{U\} = [J]^{-1}\{F\} \tag{2.90}$$

By solving Eq. (2.90) for different values of Ω, computing and plotting the vector $\{U\}$, well – known the Frequency Response plot which is a representative of a forced response analysis would be obtained.

The idea of developing JBA is based on the Forced Response Analysis explained above using HBM of a harmonically excited system. In this procedure, the domains of instabilities (unstable zones) are obtained without addressing the determinant of the Jacobian matrix which was the case in applying HBM. The motivation behind proposing this method and the implementation procedure is better addressed via a simple example. To this end, the case study presented in Figure 3 is adopted as a demonstrator.

2.6.1 Case study: 1-Dof mass – spring – damper model

Imagine that the system shown in Figure 3 is under a sinusoidal external force. Then, the governing equation of motion of the system is as follows:

$$m_1\ddot{x}_1 + C_1\dot{x}_1 + K_{v1}(t)x_1 = F_1\cos\Omega t \tag{2.91}$$

For this study, $\Omega = \alpha\eta$ and for simplicity $\alpha = 1$. To obtain the frequency response, HBM is adopted and the response of the system is expressed using Eq.

(2.88) considering $N_{h1} = 1$ and $N_{h2} = 4$ (i in Eq. (2.88) is dropped since the system has one Dof):

$$x_1 = a_0 + b_1 \sin \Omega t + a_1 \cos \Omega t + \mathrm{e}_1 \sin \frac{\eta t}{2} + g_1 \cos \frac{\eta t}{2} + e_3 \sin \frac{3\eta t}{2} + g_3 \cos \frac{3\eta t}{2} + \mathrm{e}_2 \sin \eta t + g_2 \cos \eta t + e_4 \sin 2\eta t + g_4 \cos 2\eta t \tag{2.92}$$

By substituting Eq. (2.92) in Eq. (2.91) and balancing and organizing the resultant, the residual equation given by Eq. (2.89) would be derived. For the current model the Jacobian matrix $[J]$ and the vector $\{U\}$ and $\{F\}$ have the following forms:

$$J = \begin{bmatrix} K_1 & & & & & & & & & & & \frac{k_1}{2} \\ & -m_1\Omega^2 + K_1 & -K_1\beta\Omega - \alpha m_1\Omega & & & & & & & & & \\ & K_1\beta\Omega + \alpha m_1\Omega & -m_1\Omega^2 + K_1 & & & & & & & & & \\ & & & K_1 - \frac{2k_1 + \eta^2 m_1}{4} & -\frac{K_1\beta\eta + \alpha\eta m_1}{2} & \frac{k_1}{2} & & & & & & \\ & & & \frac{K_1\beta\eta + \alpha\eta m_1}{2} & K_1 + \frac{2k_1 - \eta^2 m_1}{4} & & \frac{k_1}{2} & & & & & \\ & & & \frac{k_1}{2} & & K_1 - \frac{9\eta^2 m_1}{4} & -\frac{3K_1\beta\eta + 3\alpha\eta m_1}{2} & & & & & \\ & & & & \frac{k_1}{2} & \frac{3K_1\beta\eta + 3\alpha\eta m_1}{2} & K_1 - \frac{9\eta^2 m_1}{4} & & & & & \\ & & & & & & & -m_1\eta^2 + K_1 & -K_1\beta\eta - \alpha\eta m_1 & \frac{k_1}{2} & & \\ k_1 & & & & & & & K_1\beta\eta + \alpha\eta m_1 & -m_1\eta^2 + K_1 & & \frac{k_1}{2} & \\ & & & & & & & \frac{k_1}{2} & & -4m_1\eta^2 + K_1 & -2K_1\beta\eta - 2\alpha\eta m_1 & \\ & & & & & & & & \frac{k_1}{2} & 2K_1\beta\eta + 2\alpha\eta m_1 & -4m_1\eta^2 + K_1 & \end{bmatrix}$$

$$\{U\} = \{a_0 \quad b_1 \quad a_1 \quad e_1 \quad g_1 \quad e_3 \quad g_3 \quad e_2 \quad g_2 \quad e_4 \quad g_4\}^T$$

$$\{F\} = \{0 \quad 0 \quad 0 \quad -F_1 \quad 0 \quad 0 \quad 0 \quad 0 \quad 0 \quad 0 \quad 0 \quad 0\}^T$$

Then, Eq. (2.90) is solved for different values Ω and a single value $k_1 = 5000\left(\frac{\mathrm{N}}{\mathrm{m}}\right)$ where the frequency response of the system is depicted in Figure 8. It must be noted that for this study the frequency of the external force Ω is considered to be the same as the frequency of the parametric excitation η.

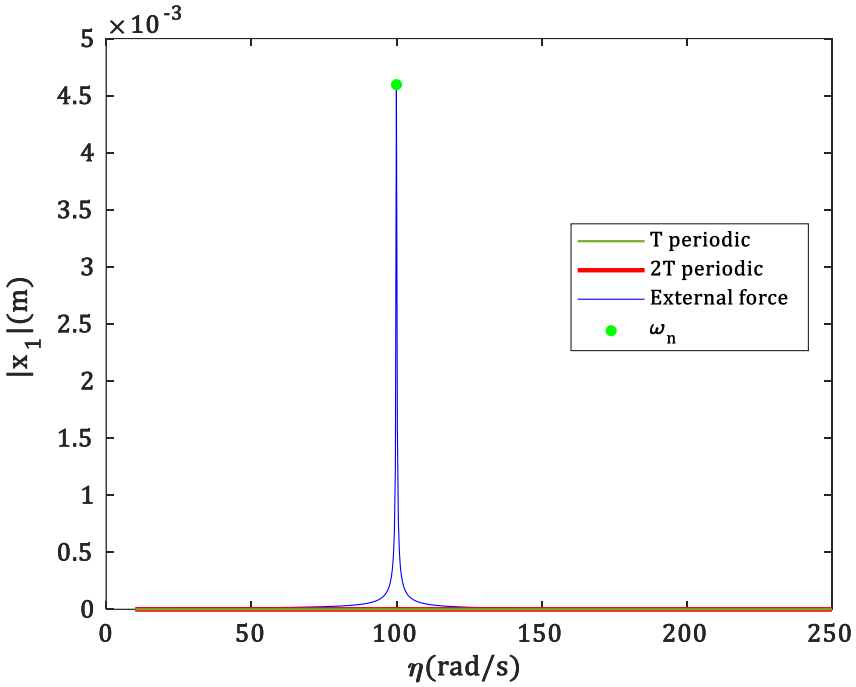

Figure 8: Frequency response at $k_1 = 5000\left(\frac{N}{m}\right)$

As shown in Figure 8, the components of the response given by Eq. (2.92) i.e. 2T periodic, T periodic, and External force are distinguished and plotted separately. To clarify this point, the components illustrated by different solid lines in Figure 8 are given as follows:

$$\begin{aligned} &\text{2T periodic} \quad && e_1 \sin\frac{\eta t}{2} + g_1 \cos\frac{\eta t}{2} + e_3 \sin\frac{3\eta t}{2} + g_3 \cos\frac{3\eta t}{2} \\ &\text{T periodic} \quad && e_2 \sin\eta t + g_2 \cos\eta t + e_4 \sin 2\eta t + g_4 \cos 2\eta t \\ &\text{External force} \quad && b_1 \sin\Omega t + a_1 \cos\Omega t \end{aligned} \tag{2.93}$$

According to Figure 8, the frequency response has just a peak at $\eta = \omega_n = 100(\text{rad/s})$ which correponds to the simple resonance; however, in the previously obtained stability plots e.g. Figure 4, it has been observed that at η around $2\omega_n$ the system has unbounded/unstable responses. This information is missed in Figure 8. To address this deficiency, consider the spy plot of the $[J]^{-1}$ given in Figure 9, where the frequency components of the unstable responses are highlighted by red rectangles. According to this figure, as long as the force vector $\{F\}$ contains zero values at the components related to the unstable responses, the corresponding

displacements within the vector of displacement $\{U\}$ would not be activated and accordingly, in the frequency response plot, no instability due to parametric excitation could be observed.

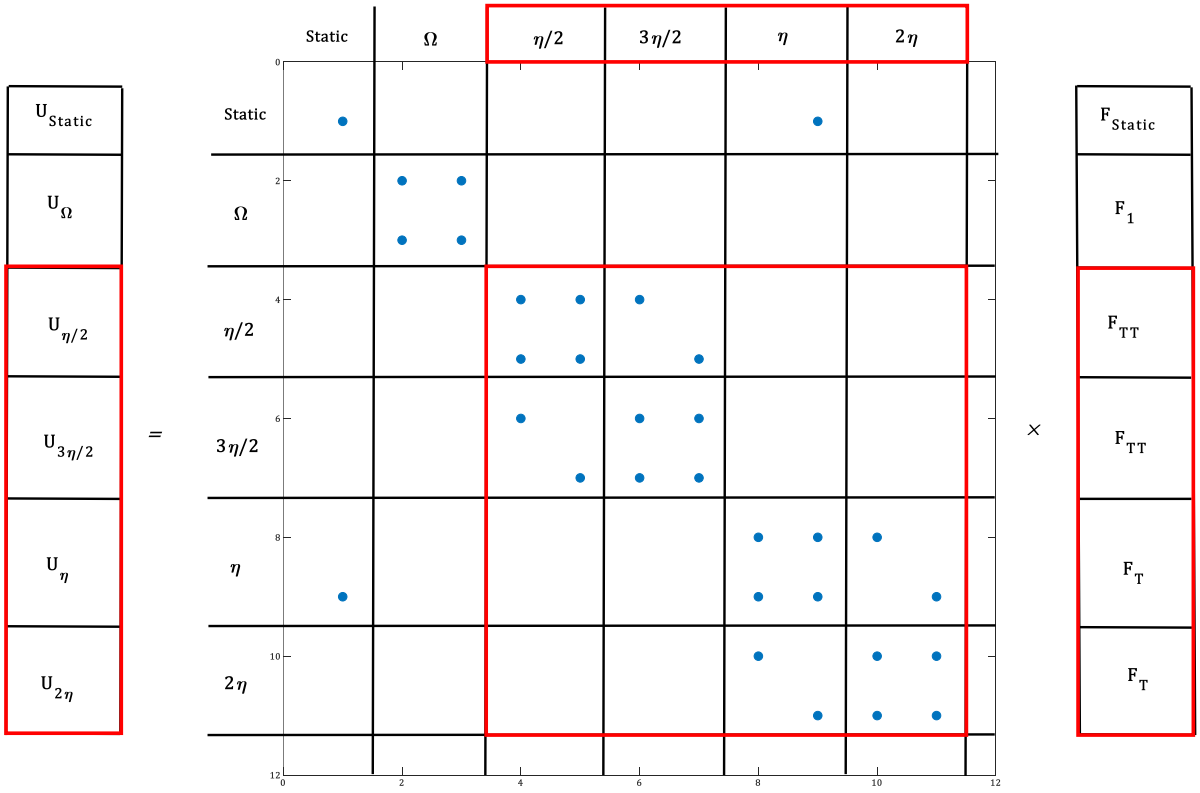

Figure 9: spy plot of the $[\boldsymbol{J}]^{-1}$ at $k_1 = 5000\left(\frac{N}{m}\right)$

To solve such an issue, some test forces whose frequencies are tuned to the frequency component of the unstable response (denoted by the red rectangles in Figure 9) are put in the equations of motion as demonstrated in the following:

$$m_1\ddot{x}_1 + C_1\dot{x}_1 + K_{1v}(t)x_1 = F_1\cos\Omega t + f_{TT} + f_T \ , \tag{2.94}$$

where:

$$\begin{aligned} f_{TT} &= F_{TT}\left(\sin\frac{\eta t}{2} + \cos\frac{\eta t}{2} + \sin\frac{3\eta t}{2} + \cos\frac{3\eta t}{2}\right) \\ f_T &= F_T\left(\sin\eta t + \cos\eta t + \sin 2\eta t + \cos 2\eta t\right) \end{aligned} \tag{2.95}$$

Then, the earlier explained procedure of HBM is followed and Eq. (2.90) is obtained. Here, the matrix Jacobian $[J]$ and vector $\{U\}$ remain the same while the elements of $\{F\}$ in Figure 9 is as follows:

$$F_{static} = \begin{Bmatrix} 0 \\ 0 \end{Bmatrix} F_{\Omega} = \begin{Bmatrix} -F_1 \\ -F_1 \end{Bmatrix}, F_{\eta/2} = F_{3\eta/2} = \begin{Bmatrix} -F_{TT} \\ -F_{TT} \end{Bmatrix}, F_{\eta} = F_{2\eta} = \begin{Bmatrix} -F_T \\ -F_T \end{Bmatrix}.$$

The idea of tracking instability due to parametric excitation by adding to the equation of motion the so – called ‘’test forces‘’ whose frequencies are related to the unstable response is proposed in this thesis. Since this method originates from HBM, it is named ‘’Jacobian Based Approach (JBA)‘’.

By solving Eq. (2.90) with new $\{F\}$, the frequency response curve of the system when $k_1 = 5000 \left(\frac{\mathrm{N}}{\mathrm{m}}\right)$ is computed for different values of η and shown in lower portion of Figure 10. In the upper part of this figure, the stability plot obtained by the Floquet theory (please check Figure 4), adopted as the reference, is depicted. According to this figure, the frequency response curve has a U – shape part around $\eta \cong 2\omega_n$ resulted from the 2T periodic components depicted by red solid lines (check Eq. (2.93)). By comparing the values of the η at the peaks of the U – shape part and the values of η at the intersections between the purple dashed line (line of $k_1 = 5000 \left(\frac{\mathrm{N}}{\mathrm{m}}\right)$) and the unstable zone in the upper part of Figure 10, it could be understood that the peaks of the U – shape part of the frequency response are associated with the boundaries of the unstable zone at $k_1 = 5000 \left(\frac{\mathrm{N}}{\mathrm{m}}\right)$ indicated by the vertical dashed blue lines.

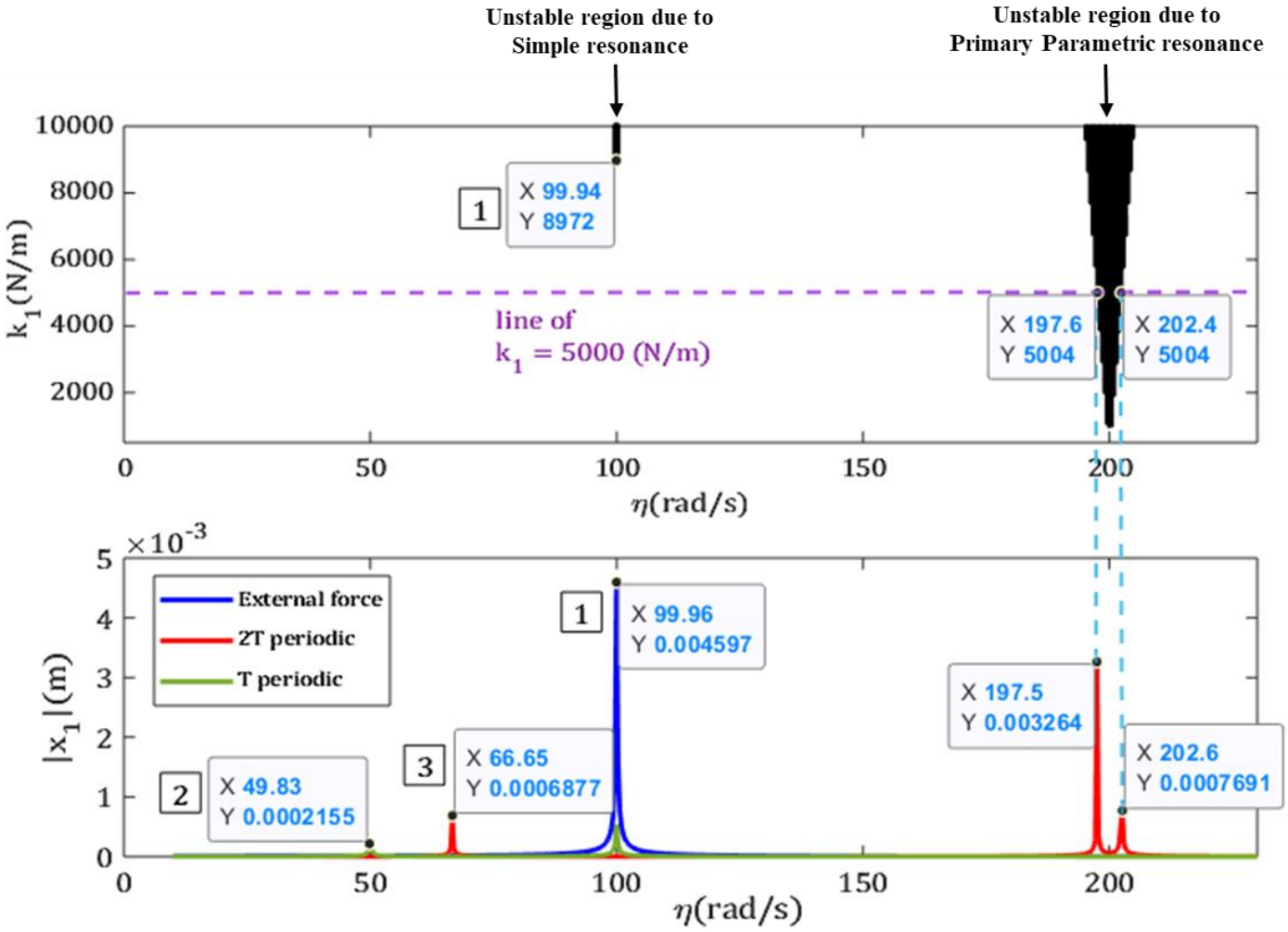

Figure 10: **Upper portion**) Stability plot Floquet Theory, **Lower Portion**) Frequency response using JBA at $k_1 = 5000\left(\frac{N}{m}\right)$

In addition, the frequency response contains other peaks which are appeared due to triggering the resonance frequency of the system. For instance, in the frequency response plot, peak 1 occurs when $\eta = \omega_n$. And, peaks 2 & 3 are due to the equality of the frequency components of the test forces introduced by Eq. (2.95) with the natural frequency of the system ω_n. For instance, according to Figure 10, the value of η at peak 2 is equal to $49.83\left(\frac{\text{rad}}{\text{s}}\right)$. Considering the frequency components of the T periodic components given in Eq. (2.93) the following is hold:

$$\eta = 49.83 \rightarrow 2\eta = 99.66 \approx \omega_n$$

which triggers the resonance frequency of the system. Similarly, by considering the value of η at peak 3 which is $66.85\left(\frac{\text{rad}}{\text{s}}\right)$, and taking into account the frequency components of 2T periodic components in Eq. (2.93), the following relation holds:

$$\eta = 66.85 \rightarrow 3\eta/2 = 99.97 \approx \omega_n$$

which again triggers the resonance frequency of the system and justifies the presence of peak 3.

In the implementation of JBA, considering a realistic value of F_{TT} and F_T is not of concern and that is why they are named "test forces". It is because the objective here is just to obtain and specify the location of the stability borders and knowing the amplitude of the response at these locations is not of interest.

Up until now, the results from JBA are shown via frequency response plot, and for a single value of $k_1 = 5000\left(\frac{\text{N}}{\text{m}}\right)$. It has been observed that by introducing the "test forces" whose frequencies are tuned according to the frequency of the responses at the unstable zones, the new frequency response curve would contain a U – shape part. Then, by comparing the values of η at the tips of the U – shape part and the ones at the intersection of the line of $k_1 = 5000\left(\frac{\text{N}}{\text{m}}\right)$ and the unstable region from Floquet theory, it is concluded that tips of the U – shape part of the frequency response locate the borders of the unstable zone.

Next, the JBA has been exploited to obtain the full stability plot where the unstable zones are illustrated for a range of (η, k_1) pairs. To do so, the following steps are taken:

a) Perform the JBA for different values of k_1 for a range of interest of η
b) For each k_1, build a frequency response plot like in Figure 10,
c) In the frequency response plot from step b, collect the maximum of the peaks characterizing the domains of instabilities i.e. the tips of the U – shape part
d) Plot the collected points from step c in the (η, k_1) plane

By performing the above procedure for different values of k_1, the stability plot presented in Figure 11 is obtained. According to this figure, the sequence of the points collected from the frequency response curve for each value of k_1 forms Transition Curves locating the unstable zone due to the parametric resonance. Furthermore, the extra lines in Figure 11 are due to the collection of the peaks

denoted by 1, 2, and 3 in Figure 10. Such results from JBA implementation were expected since the core of this method is HBM whose results were already presented and studied in section 2.3.1.

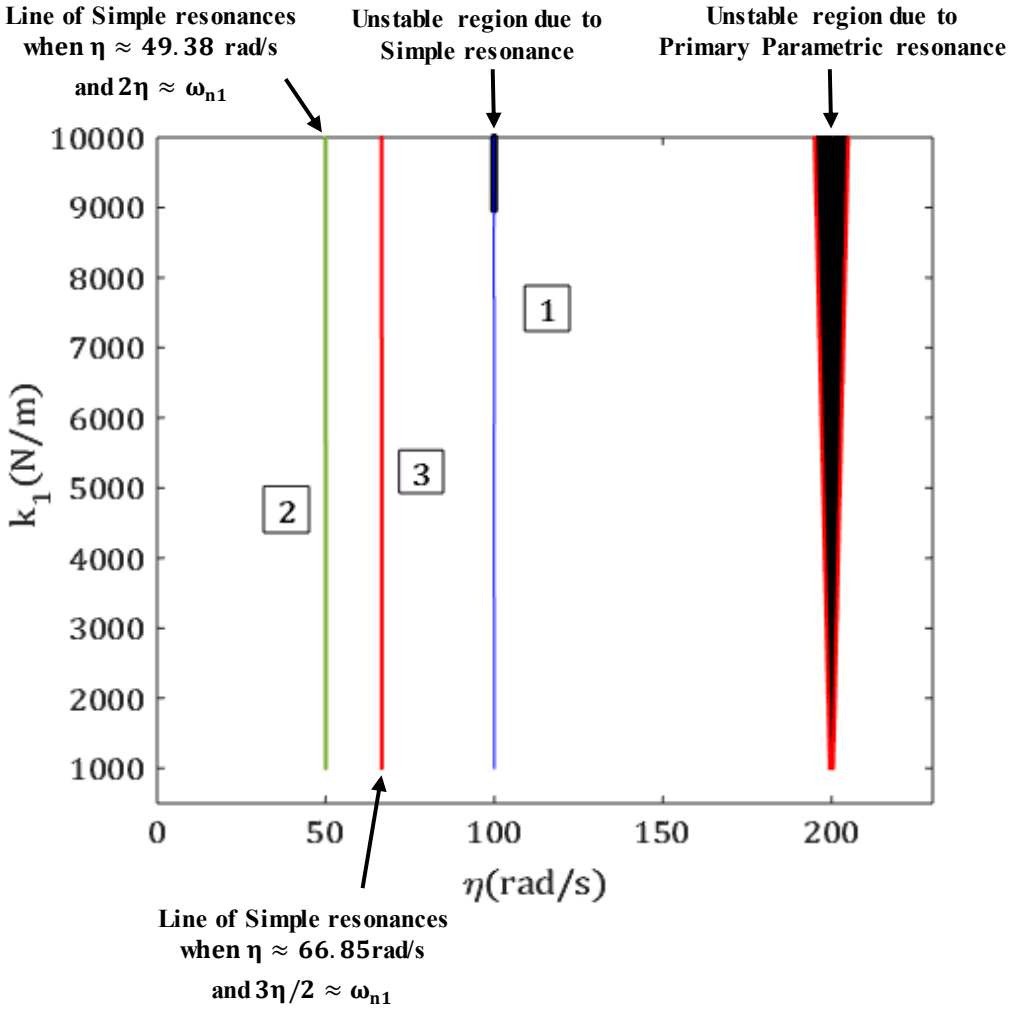

Figure 11: Stability plot of a parametrically excited 1-Dof mass – spring – damper model containing unstable zones obtained by Floquet Theory (black area) and the transition curves computed by implementing JBA

To evaluate the performance of all the stability analysis approaches in terms of the time of the computation, a trial study of their performance when $k_1 = 5000\left(\frac{\mathrm{N}}{\mathrm{m}}\right)$ & $10\left(\frac{\mathrm{rad}}{\mathrm{s}}\right) \leq \eta \leq 250\left(\frac{\mathrm{rad}}{\mathrm{s}}\right)$ is carried. The results of this trial study, presented in Table 2, indicate that JBA among all the methods is considerably time efficient.

Table 2: The computational time of the different stability analysis approaches for $k_1 = 5000\left(\frac{\mathrm{N}}{\mathrm{m}}\right)$ & $10\left(\frac{\mathrm{rad}}{\mathrm{s}}\right) \le \eta \le 250\left(\frac{\mathrm{rad}}{\mathrm{s}}\right)$

Stability analysis approach	Number of points	Time of computation
Floquet	50 samples of η	1.94 (s)
MMS	η is an unknown to be computed	1.46 (s)
HBM	η is an unknown to be computed	0.85 (s)
Hill	50 samples of η	0.04 (s)
JBA	50 samples of η	0.024 (s)

2.7 Case Study: 2-Dof mass – spring – damper model

Up until now, only instability due to the primary parametric resonance is observed. However, combination parametric resonance is a probable incident in structures under parametric excitation. Since combination parametric resonance occurs in systems with more than 1-Dof, in this section a 2-Dof coupled model of a mass – spring – damper presented in Figure 12 is adopted as a demonstrator. The governing equation of motion of this model is as follows:

$$\begin{bmatrix} m_1 & \\ & m_2 \end{bmatrix}\begin{Bmatrix} \ddot{x}_1 \\ \ddot{x}_2 \end{Bmatrix} + [C]\begin{Bmatrix} \dot{x}_1 \\ \dot{x}_2 \end{Bmatrix} + \begin{bmatrix} K_1(t)+K_c(t) & -K_c \\ -K_c & K_2(t)+K_c(t) \end{bmatrix}\begin{Bmatrix} x_1 \\ x_2 \end{Bmatrix} = \begin{Bmatrix} 0 \\ 0 \end{Bmatrix} \tag{2.96}$$

In Eq. (2.96), $K_1(t)$ and $K_2(t)$ are direct stiffness of the masses m_1 and m_2 respectively. Here $K_c(t)$ is the coupling between the two masses. For this study, $K_1(t)$, $K_2(t)$ and $K_c(t)$ are considered to be harmonic functions of time which generate parametric excitation. The mathematical expressions of these stiffnesses are as follows:

$$\begin{aligned} K_1(t) &= K_1 + k_1 \cos \eta t \\ K_2(t) &= K_2 + k_2 \cos \eta t \\ K_c(t) &= k_c \cos \eta t \end{aligned} \tag{2.97}$$

To obtain the stability plot of this model, the approaches explained in the preceding sections i.e. Floquet Theory, HBM, Hill's method, and the newly developed method JBA are employed. The values presented in Table 3 are used in the subsequent sections. It must be noted that the damping like the previous case study is a proportional damping. For this study, the parameters η and k_1 are taken as the control parameters.

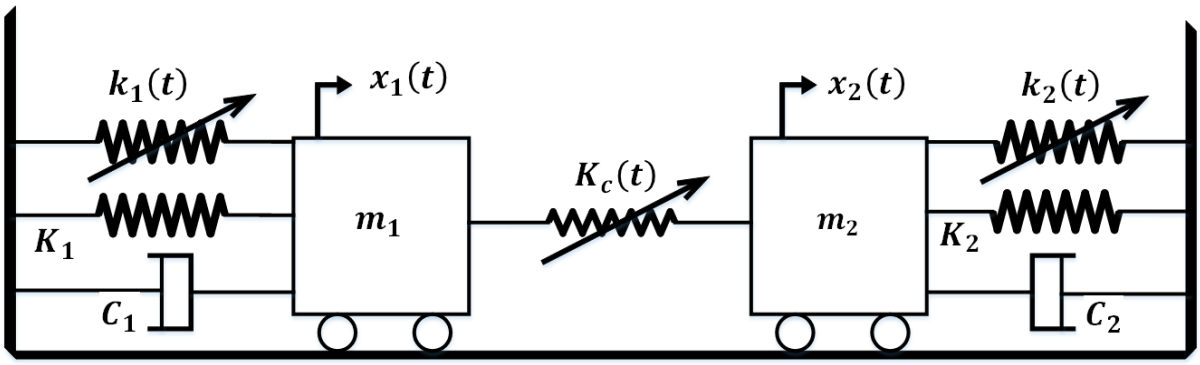

Figure 12: 2DOF coupled Mass – Damper – Spring system with time – varying stiffnesses

Table 3: Values of the parameters of the model in Figure 12

Parameters	Values
$m_1(\mathrm{kg})$	10
$m_2(\mathrm{kg})$	5
$K_1(\mathrm{N/m})$	10^5
$K_2(\mathrm{N/m})$	10^5
$\omega_{n1}(\mathrm{rad/s})$	$\sqrt{K_1/m_1} = 100$
$\omega_{n2}(\mathrm{rad/s})$	$\sqrt{K_2/m_2} = 141.5$
$k_2(\mathrm{rad/s})$	5×10^3
$k_c(\mathrm{rad/s})$	10^3
ζ	0.001

2.7.1 Floquet Theory

To obtain the stability plot, it is first the Monodromy matrix of the model is computed. Then, by examining the eigenvalues of the Monodromy matrix and

comparing their modulus against 1, the stability shown in Figure 13 would be obtained. According to Figure 13, the stability plot contains three zones of instability due to the parametric excitation. Reminding that:

$$\text{Primary Parametric Resonance Frequency: } \eta = \frac{2\omega_{ni}}{l}$$
$$\text{Combination Parametric Resonance Frequency: } \eta = \frac{\left|\omega_{ni} \pm \omega_{nj}\right|}{l}, (i \neq j) \tag{2.98}$$

where, ω_{ni} and ω_{nj} represent the natural frequencies of the system. For the current model $i, j = 1,2$. In Figure 13 and according to Eq. (2.98), the first unstable zone, formed around $\eta = 2\omega_{n1}$, is appeared due to the 1st order Primary Parametric resonance when $\omega_{ni} = \omega_{n1}$ and $l = 1$. Accordingly, the last unstable zone is arised as result of 1st order Primary Parametric resonance when $\omega_{ni} = \omega_{n2}$ and $l = 1$.

On the other hand, the middle unstable zone which was not previously observed is emerged due to the 1st order Combination Parametric Resonance of the summation type where in Eq. (2.98) $l = 1$ and $\eta = |\omega_{n1} + \omega_{n2}|$.

In Figure 13, a small unstable zone due to the simple resonance when $\eta = \omega_{n1}$ is observed while no instability at $\eta = \omega_{n2}$ is captured using Floquet Theory.

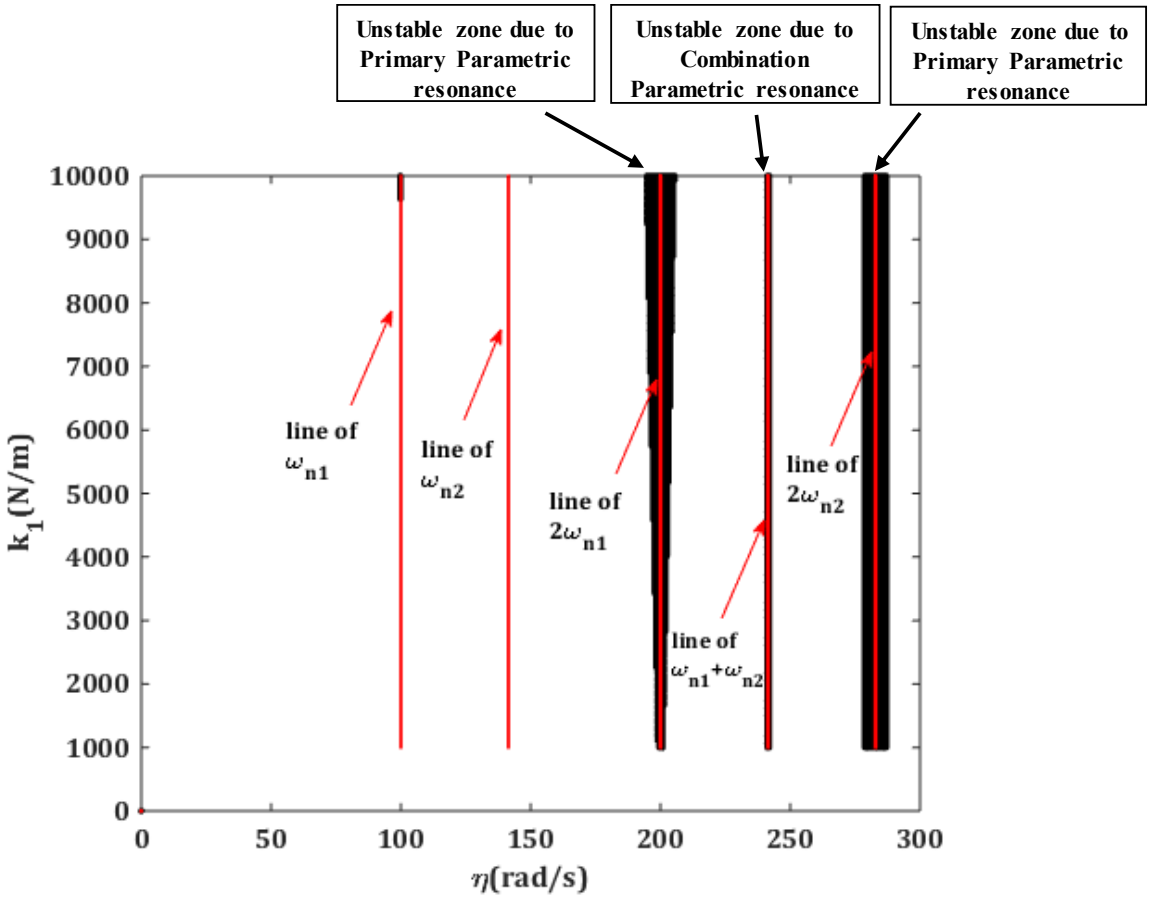

Figure 13: Stability plot of a parametrically excited 2-Dof mass – spring – damper model obtained by Floquet Theory

2.7.1.1 Effect of damping ratio ζ & Cross – Coupling parameter k_c

In this section, the influences of the damping ratio and cross – coupling stiffness on the stability plot are separately investigated.

By setting the value of $\zeta = 0.01$ and fixing the rest of the parameters as given in Table 3, the stability plot using Floquet theory is presented in Figure 14. According to the results, the damping value has a reverse effect on the domain of instability which means the greater the damping the smaller the domain of instability will be. As is observable in Figure 14, by considering the higher damping ratio the unstable zones due to the simple and combination parametric resonances are disappeared. In addition, the unstable regions resulted from the Primary parametric resonances became smaller and more limited in their domain.

The effect of the cross – coupling stiffness is investigated by increasing the value of k_c. Here by considering k_c to be equal to 3×10^3 and keeping the rest of the parameters the same as in Table 3, the stability plot using the Floquet theory is displayed in Figure 15. As shown in this figure, the influence of the cross – coupling on the domain of the unstable regions, due to both the simple and parametric resonances, is linear. In other words, the increase of the cross – coupling stiffness results in the appearance of the more unstable responses and consequently growth of the instability regions.

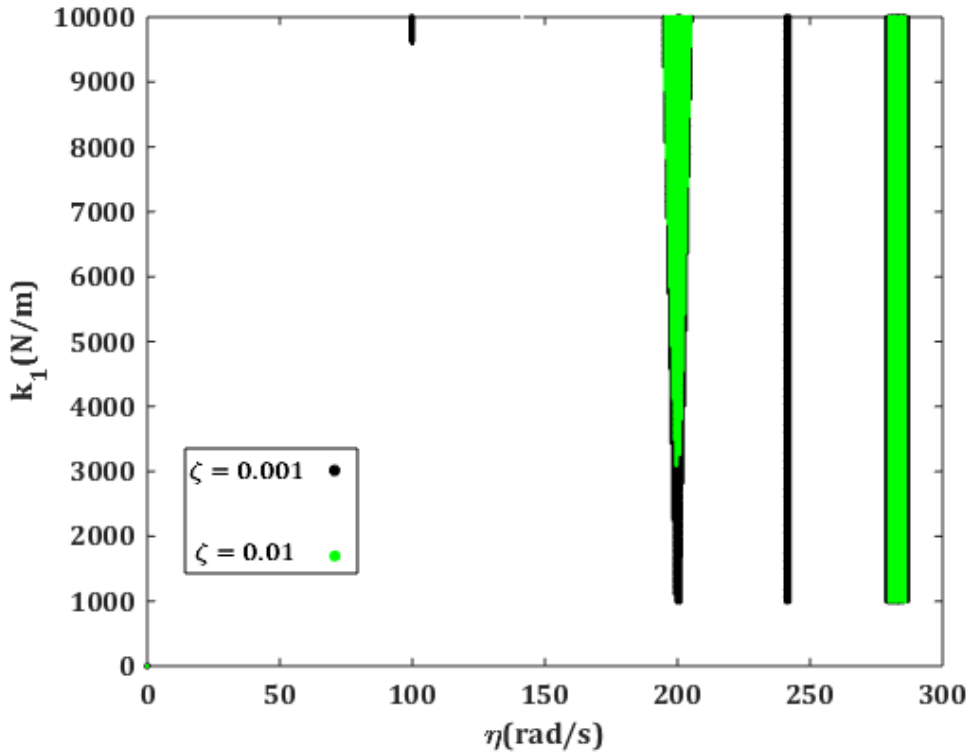

Figure 14: Effect of the damping on the instability regions

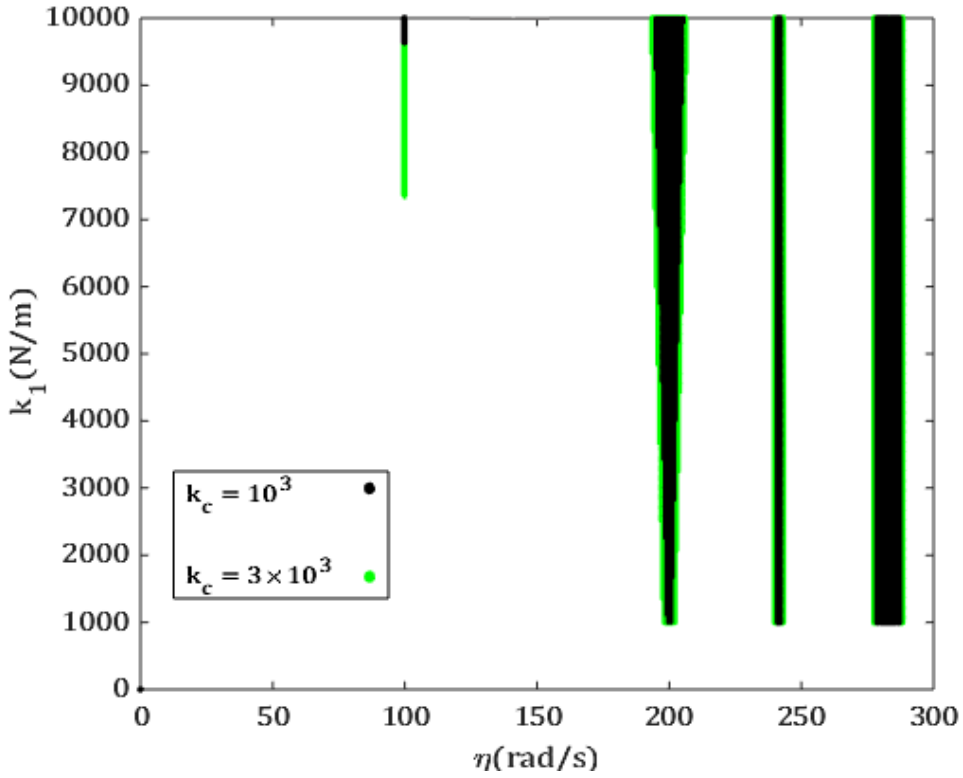

Figure 15: Effect of the cross – coupling on the instability regions

2.7.2 HBM

As was discussed in section 2.3, to obtain the stability plot using HBM, the response of the system must be expressed by the T and $2T$ periodic responses via Fourier series. It is worth noting that T is the period of the parametric excitation and is equal to $2\pi/\eta$. To proceed with HBM, first the coordinates x_1 and x_2 are written as follows:

$$x_{1_T} = \sum_{z=0,2,4}^{N_1} \left(a_z \sin\frac{z\eta t}{2} + b_z \cos\frac{z\eta t}{2} \right)$$
$$x_{2_T} = \sum_{h=0,2,4}^{N_1} \left(c_h \sin\frac{h\eta t}{2} + d_h \cos\frac{h\eta t}{2} \right) \quad (2.99)$$

$$x_{1_{TT}} = \sum_{z=1,3}^{N_2} \left(a_z \sin\frac{z\eta t}{2} + b_z \cos\frac{z\eta t}{2} \right)$$
$$x_{2_{TT}} = \sum_{h=1,3}^{N_2} \left(c_h \sin\frac{h\eta t}{2} + d_h \cos\frac{h\eta t}{2} \right) \quad (2.100)$$

And, truncating Eq. (2.99) and Eq. (2.100) by two harmonics i.e. $N_1 = N_2 = 2$ and substituting them in Eq. (2.96), and balancing the resultant equations, yields the following equations:

$$[J_T] \begin{Bmatrix} b_0 \\ d_0 \\ a_2 \\ c_2 \\ b_2 \\ d_2 \\ a_4 \\ c_4 \\ b_4 \\ d_4 \end{Bmatrix} = 0 \ , \quad (2.101)$$

$$[J_{TT}] \begin{Bmatrix} a_1 \\ c_1 \\ b_1 \\ d_1 \\ a_3 \\ c_3 \\ b_3 \\ d_3 \end{Bmatrix} = 0 \quad (2.102)$$

To obtain the Transition Curves, the frequency of the parametric excitation η is considered to be an unknown. This leads the Jacobian matrices in Eq. (2.101) and Eq. (2.102) to become functions of η. For non – trivial solutions, the determinants of $[J_T]$ and $[J_{TT}]$ must be equated to zero. By solving the determinants for different values of k_1, the corresponding values of η where non – trivial solutions exist would

be acquired. By collecting the values of η for each value of k_1 and plotting them, a stability plot presented in Figure 16 would be found.

As depicted in Figure 16, the consideration of the harmonic components corresponding to the $2T$ periodic response in the Fourier series (please check Eq. (2.99) and Eq. (2.100)), results in the transition curves locating the instabilities due to the Primary Parametric Resonances, shown by purple dots. Furthermore, adopting the harmonic components corresponding to the T periodic response in the Fourier series gives the transition curves, the green dots, detecting the unstable responses due to the Simple Resonance. In Figure 16, all the transition curves obtained by HBM implementation accurately locate the unstable zones found by Floquet Theory.

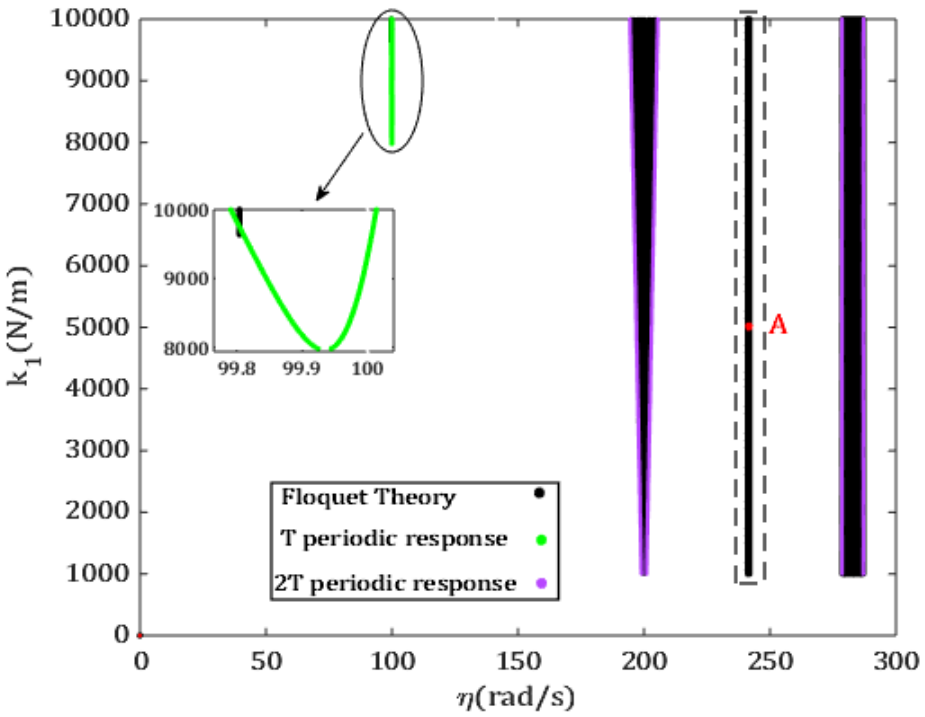

Figure 16: Stability plot of a parametrically excited 2-Dof mass – spring – damper model containing the transition curves obtained by HBM

According to Figure 16, HBM is efficient in locating the unstable zones due to the primary parametric resonance while it misses the unstable arisen as a result of the Combination Parametric Resonance. This issue is observable in Figure 16 where the unstable region due to the combination parametric resonance, highlighted by the dashed rectangular, does not contain any transition curves.

To investigate this deficiency, the FFT of a trial point, point A in Figure 16, inside the unstable zone due to the combination parametric resonance, is depicted in Figure 17. This figure shows that the responses x_1 and x_2 at the unstable region resulted from the combination parametric resonance are quasi – periodic and possess two frequency components at ω_{n1} and ω_{n2} whose summation is equal to the value of η.

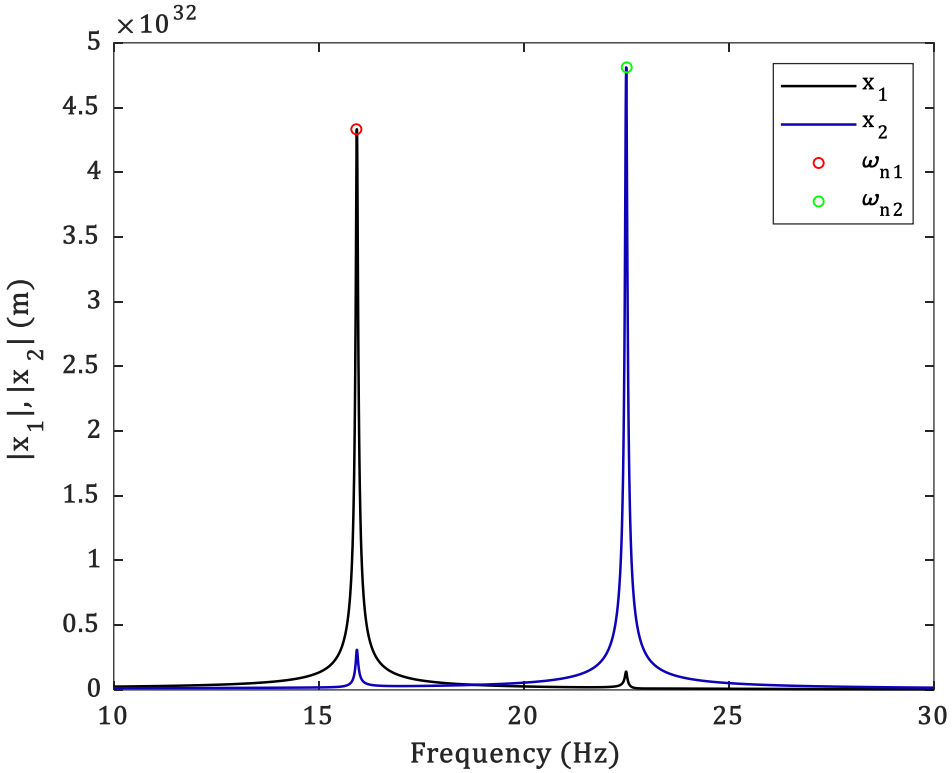

Figure 17: FFT of the response of point A in Figure 16 where k_1=5000$\left(\frac{N}{m}\right)$ and $\eta = \omega_{n1} + \omega_{n2}$

To propose a general formula, the dominant frequencies in Figure 17 are denoted by ω_1 and ω_2 which have the following characteristic:

$$\omega_1 + \omega_2 = \eta \tag{2.103}$$

Using Eq. (2.103), the responses x_1 and x_2 are expressed by the following Fourier series:

$$x_{1_C} = \sum_{s=1,2,\ldots}^{N_3} \left(\left(w_{1s} \sin s\omega_1 t + q_{1s} \cos s\omega_1 t \right) + \left(v_{1s} \sin s\omega_2 t + u_{1s} \cos s\omega_2 t \right) \right) \tag{2.104}$$

$$x_{2_C} = \sum_{s=1,2,\ldots}^{N_3} \left(\left(w_{2s} \sin s\omega_1 t + q_{2s} \cos s\omega_1 t \right) + \left(v_{2s} \sin s\omega_2 t + u_{2s} \cos s\omega_2 t \right) \right) \tag{2.105}$$

Truncating Eq. (2.104) and Eq. (2.105) by one harmonic, substituting them in Eq. (2.96) taking into account Eq.(2.103), and balancing the resultant equation, yields the following:

$$[J_C] \begin{Bmatrix} e_1 \\ g_1 \\ f_1 \\ p_1 \end{Bmatrix} = 0 \tag{2.106}$$

As pointed out earlier, to implement HBM to find the transition curves, it is necessary to keep one of the control parameters as an unknown. Then, to compute it, the determinant of the Jacobian matrix equated to zero must be solved by changing the other parameter. Here, η is taken as the unknown. To find the transition curves, the determinant of $[J_C]$ in Eq. (2.106). However, in the determinant of this specific Jacobian matrix, there is another unknown which is ω_1.

Accordingly, solving the determinant of $[J_C]$ does not suffice to find both η and ω_1. Therefore, another equation is required to compute both of the unknowns. As discussed in section 2.3 by Eq. (2.34), the additional equation is the highest minor of $[J_C]$. Hence, to find the transition curves following Equations mus be solvbed simultaneously:

$$\begin{aligned} |J_C| &= 0 \\ |J_C|_m &= 0 \end{aligned}, \tag{2.107}$$

results in the stability plot depicted in Figure 18. As shown in this figure, by adopting the dominant frequencies of the quasi – periodic response at the unstable zone due to the combination parametric resonance, HBM can accurately detect all the unstable regions.

It must be noted that in the next chapters, the general form of the Fourier Series given by Eq. (2.33) is adopted to mathematically demonstrate the coordinates by their harmonics. In this chapter, on the other hand, the Fourier expressions of each

harmonic are demonstrated individually to present the contribution of each harmonic in the stability plot.

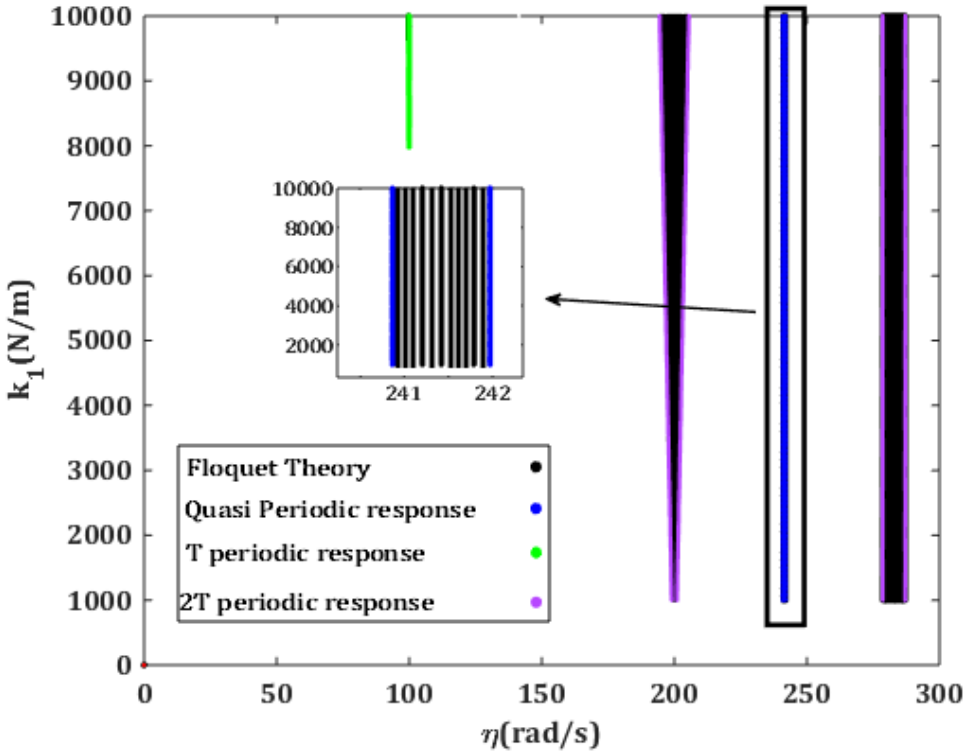

Figure 18: Full stability plot of a parametrically excited 2-Dof mass – spring – damper model containing the transition curves obtained by HBM

2.7.3 Hill's method

In this section, the stability analysis of the 2-Dof model, given in Figure 12, using Hill's method is performed. To proceed with this method the coordinates x_1 and x_2 are first perturbed as explained in section 2.4 where the perturbing term is expressed by the Floquet Form signified in Eq. (2.42). Afterwards, the periodic vector $\mathrm{X}(t)$ of each coordinate is expressed by the Fourier series associated to the $2T$ and T periodic responses:

$$\mathrm{X}_i = \sum_{z=0,1,2,\ldots}^{N_h} \left(a_{iz} \sin \frac{z\eta t}{2} + b_{iz} \cos \frac{z\eta t}{2} \right) \tag{2.108}$$

The same procedure explained in section 2.4.1 is followed subsequently. After computing the Floquet Exponents, $2n$ of them with the smallest imaginary parts in

modulus are retained. Then, by checking the real parts of the retained Floquet Exponents against zero, the pairs of (k_1, η) at which the real parts are greater than zero are collected. Next, by plotting the collected pairs of (k_1, η), the stability plot presented in Figure 19 is found.

To investigate the accuracy of the results from Hill's method, the results from HBM implementation i.e. transition curves which were already approved by Floquet theory are adopted. As illustrated in Figure 19 the instabilities due to the Parametric and Simple resonances are perfectly acquired by Hill's method.

It must be noted that the frequency component related to the $2T$ periodic response in Eq. (2.108) allows Hill's method to find the instability due to the combination parametric resonance which was not the case in HBM implementation.

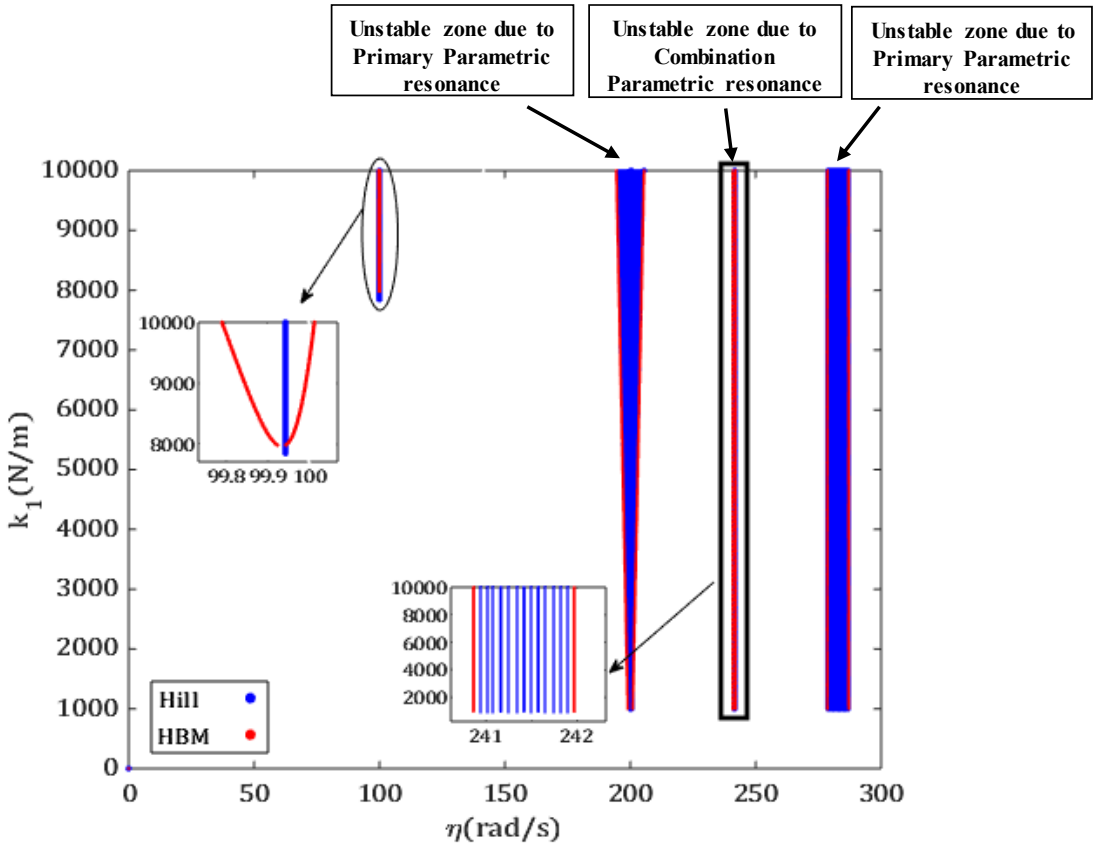

Figure 19: Stability plot of a parametrically excited 2-Dof mass – spring – damper model containing the transition curves obtained by Hill's method

2.7.4 Jacobian Based Approach (JBA)

In this section, the aim is to obtain the stability plot via the proposed method in this thesis. To start, consider external harmonic forces for each mass as follows:

$$\begin{bmatrix} m_1 & \\ & m_2 \end{bmatrix}\begin{Bmatrix} \ddot{x}_1 \\ \ddot{x}_2 \end{Bmatrix}+\begin{bmatrix} C_1 & \\ & C_2 \end{bmatrix}\begin{Bmatrix} \dot{x}_1 \\ \dot{x}_2 \end{Bmatrix}+ \begin{bmatrix} K_1(t)+K_c(t) & -K_c \\ -K_c & K_1(t)+K_c(t) \end{bmatrix}\begin{Bmatrix} x_1 \\ x_2 \end{Bmatrix}=\begin{Bmatrix} f_1(t) \\ f_2(t) \end{Bmatrix} \tag{2.109}$$

Where $f_1(t) = F_1 \cos \Omega t$ and $f_2(t) = F_2 \cos \Omega t$. Using the information acquired by HBM about the frequency components in the unstable zone due to the combination resonance i.e. ω_1 and ω_2, the coordinates of the system are expanded by the following Fourier series:

$$x_i = \sum_{l=0,1,2,\dots}^{N_{h1}} \left(a_{iz}\, sin\, l\Omega t + b_{iz}\, cos\, l\Omega t\right) + \sum_{z=1,2,\dots}^{N_{h2}} \left(c_{iz}\, sin\, \frac{z\eta t}{2} + d_{iz}\, cos\, \frac{z\eta t}{2}\right) + \sum_{s=1,2,\dots}^{N_{h3}} \left(\left(w_{is}\, sin\, s\omega_1 t + q_{is}\, cos\, s\omega_1 t\right) + \left(v_{is}\, sin\, s\omega_2 t + u_{is}\, cos\, s\omega_2 t\right)\right) \tag{2.110}$$

For this study $N_{h1} = N_{h3} = 1$ and $N_{h2} = 4$. It must be noted that the condition given by Eq. (2.103) holds here and accordingly $\omega_1 = \eta - \omega_2$. By expressing x_1 and x_2 according to Eq. (2.110), then substituting them in Eq. (2.109), balancing the resultant equation, the following residual equation would be obtained:

$$\{R\} = [J]\{U\} - \{F\} \tag{2.111}$$

Then, by minimizing the residual vector $\{R\}$ (equate it to zero) the vector $\{U\}$ could be computed by the subsequent equation:

$$\{U\} = [J]^{-1}\{F\} \tag{2.112}$$

For this study $\Omega = \eta$. By solving Eq. (2.112) for $k_1 = 6000\left(\frac{\mathrm{N}}{\mathrm{m}}\right)$ and different values of η, the frequency reponse of the sysem for each coordinate is shown in Figure 20. According to the frequency response plots, the system has high amplitudes just at its resonances when $\eta = \omega_{n1}, \omega_{n2}$ in spite of the fact that instabilities were observed previously at other values of η. In Figure 20, the

contributions of the frequency components correspoding to the instability due to the parametric excitation are null. The legends in Figure 20 denote each frequency component used in Eq. (2.110).

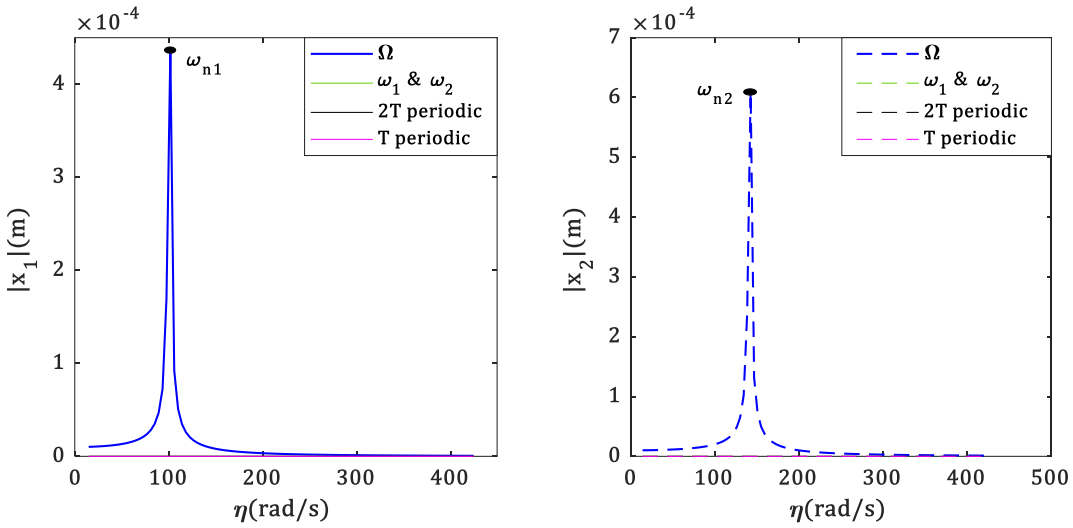

Figure 20: Frequency response of coordinates x_1 (on the left) & x_2 (on the right) at $\boldsymbol{k}_1 = 6000\left(\frac{\mathrm{N}}{\mathrm{m}}\right)$

To address the deficiency of the frequency response in Figure 20, like before, the spy plot presented in Figure 21 is taken into account. Here, the frequency contents characterizing the unstable zones due to the parametric excitation are highlighted by the red rectangles. It can be understood from Figure 21 that in order not to have null contributions of these frequencies within the frequency response plot, the components of the vector force inside the red rectangle on the right – hand side must not contain zeros.

To solve this problem the so – called harmonic "test forces" whose frequencies are tuned according to the frequencies indicated in the red box in Figure 21 are added to the force vector of Eq. (2.109):

$$\begin{bmatrix} m_1 & \\ & m_2 \end{bmatrix}\begin{Bmatrix} \ddot{x}_1 \\ \ddot{x}_2 \end{Bmatrix}+\begin{bmatrix} C_1 & \\ & C_2 \end{bmatrix}\begin{Bmatrix} \dot{x}_1 \\ \dot{x}_2 \end{Bmatrix}+ \\ \begin{bmatrix} K_1(t)+K_c(t) & -K_c \\ -K_c & K_1(t)+K_c(t) \end{bmatrix}\begin{Bmatrix} x_1 \\ x_2 \end{Bmatrix}=\begin{Bmatrix} f_1+f_C+f_{TT}+f_T \\ f_2+f_C+f_{TT}+f_T \end{Bmatrix} \tag{2.113}$$

Where:

$$f_{TT} = F_{TT}\left(\sin\frac{\eta t}{2}+\cos\frac{\eta t}{2}+\sin\frac{3\eta t}{2}+\cos\frac{3\eta t}{2}\right)$$
$$f_{T} = F_{T}\left(\sin\eta t+\cos\eta t+\sin 2\eta t+\cos 2\eta t\right) \quad (2.114)$$
$$f_{C} = F_{C}\left(\sin\omega_1 t+\cos\omega_1 t+\sin\left(\eta t-\omega_1 t\right)+\cos\left(\eta t-\omega_1 t\right)\right)$$

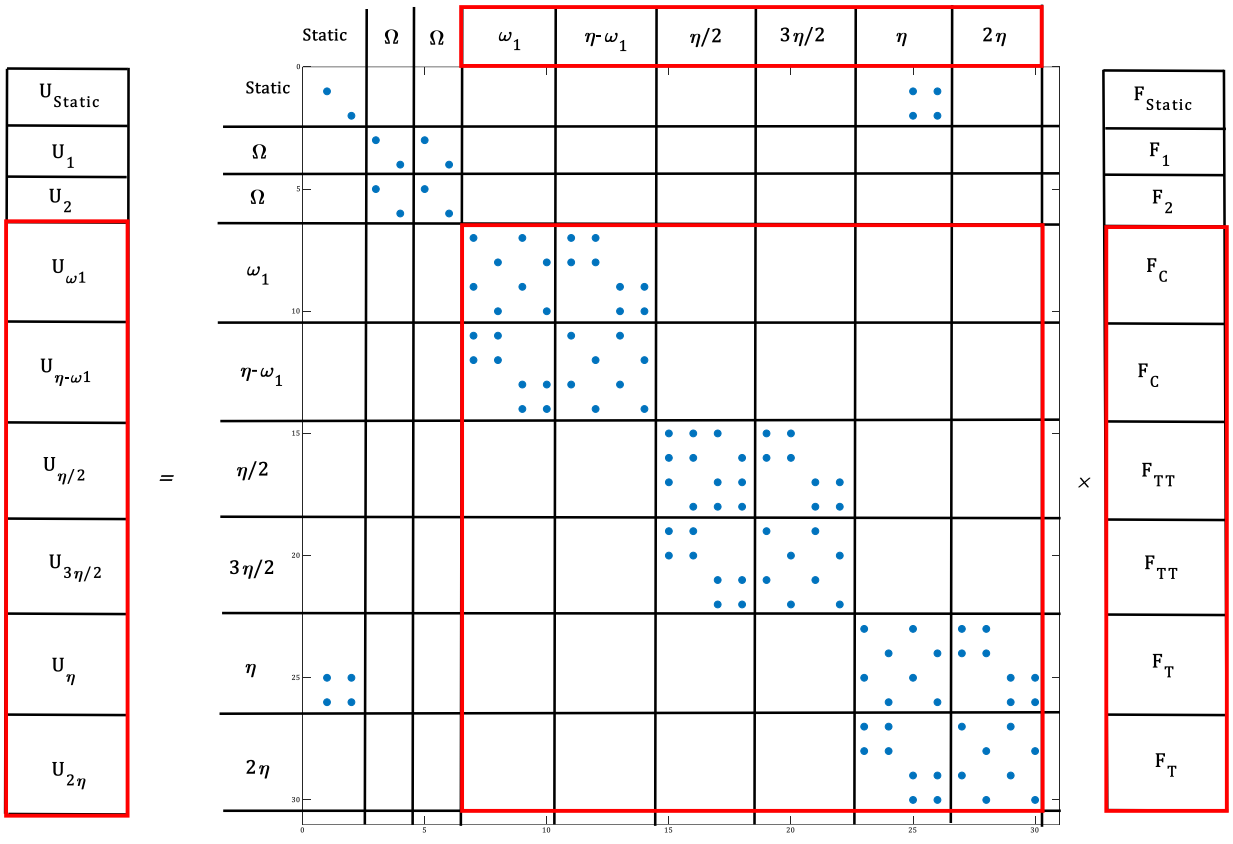

Figure 21: spy plot of the $[J]^{-1}$

Unlike HBM implementation where ω_1 was considered to be an unknown, here it is necessary to know the value of this parameter in Eq. (2.114). To do so, in the lower portion of Figure 22, the FFTs of points A and B (check the Upper portion of Figure 22) which are the intersections between the line of $k_1 = 6000\left(\frac{\mathrm{N}}{\mathrm{m}}\right)$ and transition curves associated to the unstable zone due to combination parametric resonance are presented. In this figure the following mathematical relations are observed:

$$\left(\omega_{1A}+\omega_{1B}\right)/2\cong\omega_{n1} \tag{2.115}$$

$$\left(\omega_{2A}+\omega_{2B}\right)/2\cong\omega_{n2} \tag{2.116}$$

$$\omega_{2B}-\omega_{1B}\cong\omega_{2A}-\omega_{1A} \tag{2.117}$$

By subtracting Eq. (2.115) from Eq. (2.116):

$$\omega_{2A}-\omega_{1A}\cong\omega_{n2}-\omega_{n1}\ , \tag{2.118}$$

and using Eq, (2.117) and Eq. (2.118):

$$\omega_{2B}-\omega_{1B}\cong\omega_{n2}-\omega_{n1} \tag{2.119}$$

The following relations hold on the transition curves corresponding to the unstable region due to the parametric combination resonance:

$$\omega_{1A}+\omega_{2A}=\eta_A \tag{2.120}$$

$$\omega_{1B}+\omega_{2B}=\eta_B \tag{2.121}$$

Subtraction of Eq. (2.120) and Eq. (2.121) from respectively Eq. (2.118) and Eq. (2.119) results in the following:

$$\omega_{1A}\cong\left(\eta_A+\omega_{n1}-\omega_{n2}\right)/2\ ,\ \omega_{2A}\cong\eta_A-\omega_{1A} \tag{2.122}$$

$$\omega_{1B}\cong\left(\eta_B+\omega_{n1}-\omega_{n2}\right)/2\ ,\ \omega_{2B}\cong\eta_B-\omega_{1B} \tag{2.123}$$

Then, by adopting Eq. (2.122) and Eq. (2.123) the following general formula is proposed to compute ω_1 and ω_2 for a system with discrete natural frequencies:

$$\omega_1=\frac{\left|\left(\eta+\omega_{n1}-\omega_{n2}\right)\right|}{2}\ ,\ \omega_2=\eta-\omega_1 \tag{2.124}$$

This equation will also be obtained for a more complex system in chapter 4 and its credibility will be further approved.

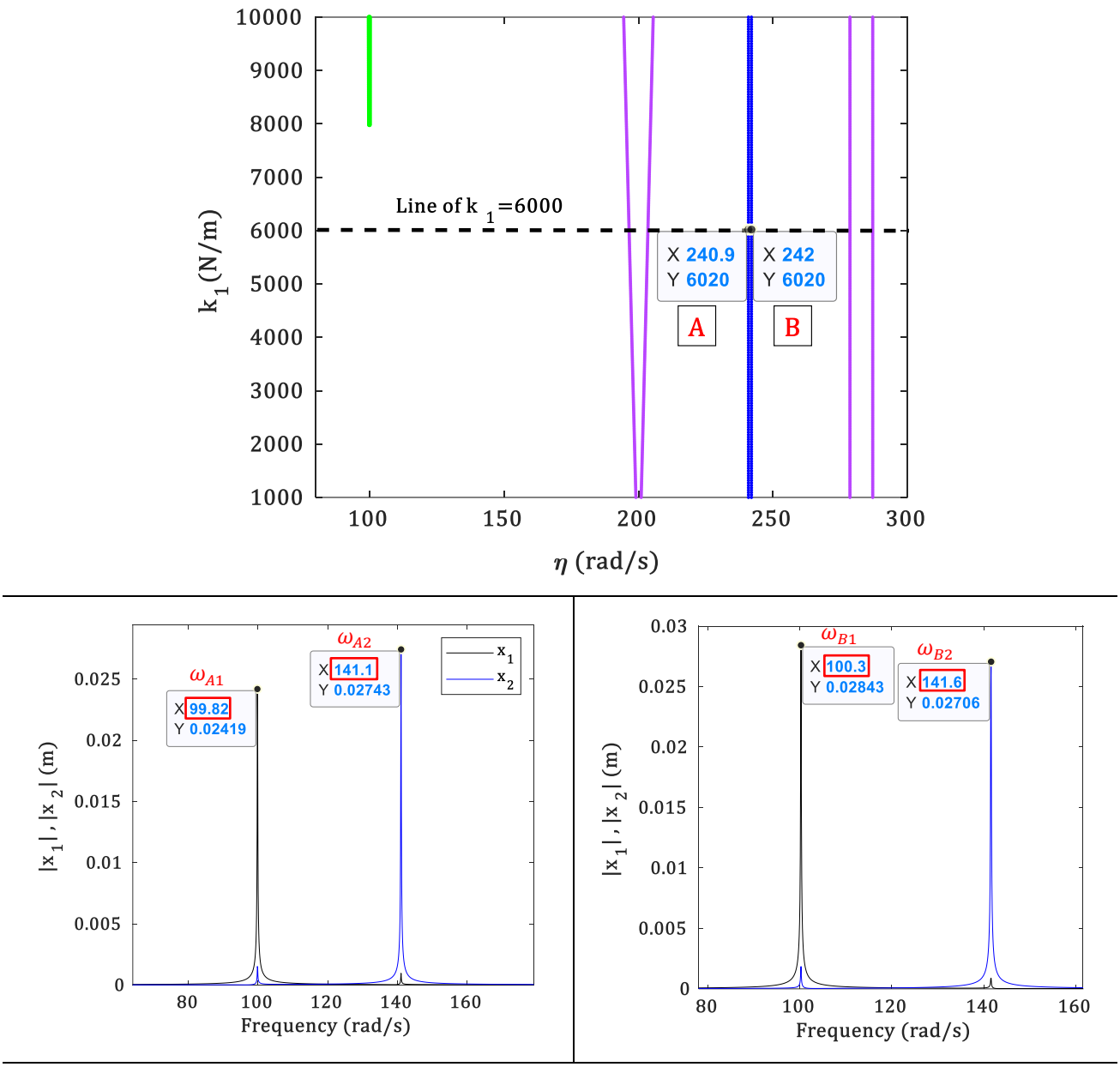

Figure 22: **Upper portion)** Stability plot from HBM showing the intersections (points A & B) of the line of $\boldsymbol{k}_1 = 6000\left(\frac{\mathrm{N}}{\mathrm{m}}\right)$ and the transition curves encompassing the area of unstable responses due to the combination parametric resonance. **Lower right portion)** FFT of the response at points A. **Lower left portion)** FFT of the response at point B

By inserting Eq. (2.124) in Eq. (2.114), employing the Fourier series of the coordinates given by Eq. (2.110), and solving Eq. (2.112), the new frequency response plot is displayed in Figure 23. By adding the test forces, the frequency

response curve shown in Figure 23, contains multiple U - shape parts, represented by ①, ②, and ③ whose peaks indicate the border of the unstable zones caused by the parametric resonances. By comparing the values of η on the peaks of the U – shape part of the frequency response curve, denoted by the labels, and comparing them with their correspondence in the stability plot from Floquet theory, also represented by the labels, it can be understood that JBA specified the borders of the unstable zones at each value of k_1. The values of η in ① at peaks on the frequency response curve of the $2T$ periodic components of the coordinate x_1 (please check the black solid line in the legend bar on the lower right portion of Figure 23), specify the borders of the unstable zone due to the Primary parametric resonance when $\eta \cong 2\omega_{n1}$. On other hand, the values of η at the peaks in area ③ associated with the frequency response of the $2T$ periodic components of coordinate x_2 (please check the black dashed line in the legend bar on the lower right of portion Figure 23), indicate the borders of the unstable region as a result of the Primary parametric resonance when $\eta \cong 2\omega_{n2}$.

The values of η at peaks in the zone ② boundary of the instability appeared because of the Combination parametric resonance when $\eta \cong \omega_{n1} + \omega_{n2}$. According to the zoomed view of ② shown in the upper right portion of Figure 23, the frequency response curves corresponding to the ω_1 & ω_2 components of both of the coordinates i.e. x_1 and x_2 (please check respectively the green solid and dashed lines in the legend bar) contain the two pairs of peaks at the same values of η but with different amplitudes. Where the values of η at each pair specifies the border of the unstable region due to the combination parametric resonance. What could be understood here is that at the combination parametric resonance zone, each coordinate of the system is responding/oscillating at two frequencies at the same time whose summation is equal to the frequency of the parametric excitation.

In Figure 23, the single peaks, excluding the peaks at ①, ②, and ③, are appeared when the frequencies of the test forces become equal to one of the natural frequencies ω_{n1} or ω_{n2}. For instance the peak at ④ where $\eta = 50\left(\frac{\text{rad}}{\text{s}}\right)$ is emerged since the frequency component 2η of test force f_T in Eq. (2.114) generates resonance at $\omega_{n1} = 101\left(\frac{\text{rad}}{\text{s}}\right)$.

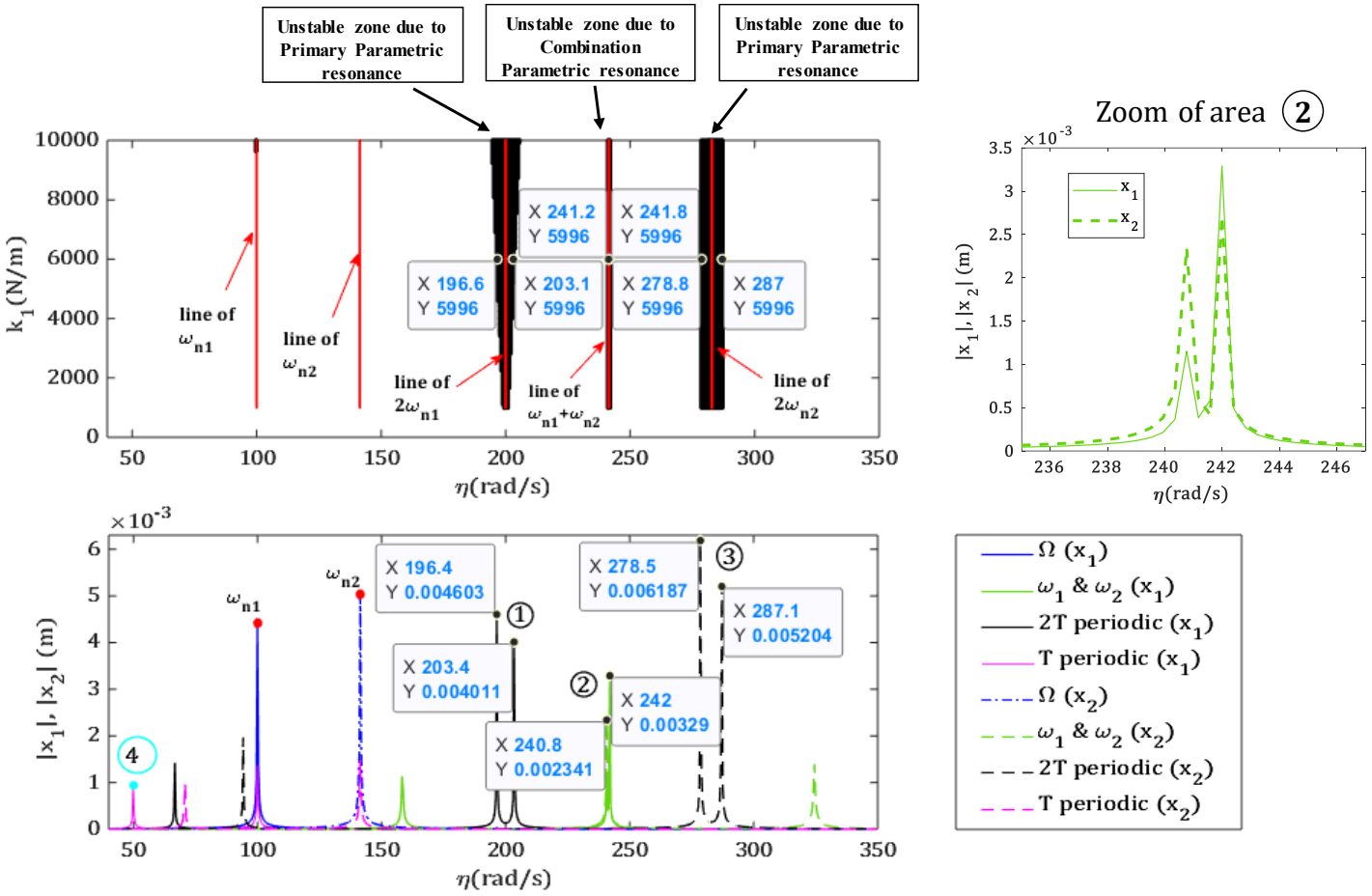

Figure 23: Comparison of the results obtained by JBA (Lower plot) and the ones from Floquet Theory (Upper plot) at $\boldsymbol{k}_1 = 6000\left(\frac{\mathrm{N}}{\mathrm{m}}\right)$

To compute the full stability plot using JBA the subsequent steps are performed sequentially:

a) Perform the JBA for different values of k_1 for a range of interest of η
b) For each k_1, build a frequency response plot like in Figure 23
c) In the frequency response plot from step b, collect the maximum of the peaks characterizing the domains of instabilities i.e. the tips of the U – shape part i.e. peaks at ①, ②, and ③
d) Plot the collected points from step c in the (η, k_1) plane

By iterating the steps from a to d, as mentioned above, the stability plot shown in Figure 24 is acquired. As shown in this figure, the results from JBA perfectly locate the areas of instabilities due to the Primary and Combination parametric

resonances. Here, unlike Figure 11, due to the numerous line of simple resonances for the current model, they were disregarded from the stability plot in Figure 24 by suppressing the corresponding frequencies.

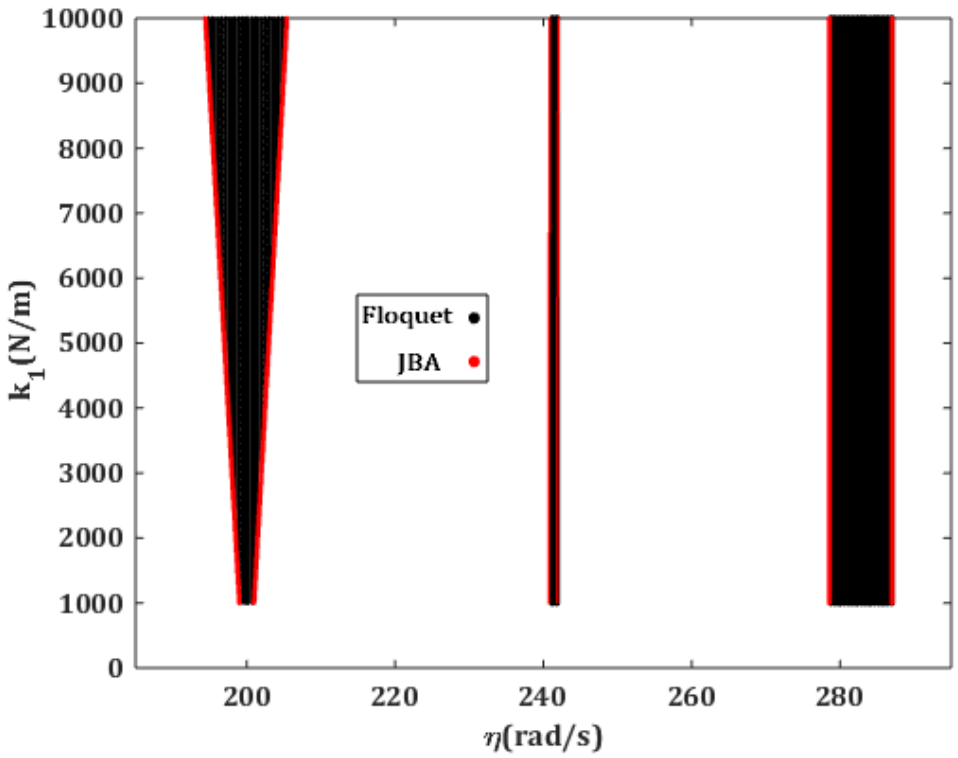

Figure 24: The full stability plot obtained by JBA implementation and approved by the results from Floquet theory

2.8 Conclusion

This chapter has been dedicated to detailed explanations of the state-of-the-art stability analysis approaches of a parametrically excited system i.e. Floquet Theory, Hill's method, Harmonic Balance Method (HBM), and Method of Multiple Scales (MMS). In this study, a new method named Jacobian Based Approach (JBA) to study the stability of a system under parametric excitation is proposed. To study and demonstrate the implementation procedure of each approach mentioned above, a model of a mass – spring – damper system is adopted as a demonstrator. In this model, the spring is considered to have a time – varying stiffness which introduces the parametric excitation to the system. By computing and comparing the stability plots from each approach, the following remarks are made:

- General remarks:
  - The effects of the cross – coupling stiffness and the damping on the unstable zones are contrary to each other. The increase of the cross – coupling stiffness leads to an increase in the domain of the unstable regions while the damping decreases the domain of the unstable zones.
  - Implementations of the Floquet theory and Hill's method result in stability plots highlighting the unstable/unbounded responses.
  - The application of HBM and MMS leads to the computation of the transition curves indicating the border of the stable – unstable zones.
  - Adopting the T periodic frequency components in Hill's method results in finding the unstable regions due to the Simple resonances.
  - Adopting the T periodic frequency components in HBM and JBA results in finding the transition curves encompassing the unbounded responses due to the Simple resonances.
  - JBA obtains accurately the transition curves in a very low computational time in comparison to other approaches.
  - JBA enables the study of the stability of a system under parametric excitation within the frequency response plot. Such a study was not found in the literature.
- 1-Dof parametrically excited model:
  - The stability plot of a 1-Dof system under parametric excitation contains two unstable zones due to the Primary Parametric and Simple resonances.
  - Hill's method finds instabilities due to the Primary parametric resonances by employing the $2T$ periodic frequency components.
  - In implementing HBM and JBA, the consideration of the $2T$ periodic frequency components results in the transition curves enclosing the unstable responses due to the Primary parametric resonance.
- 2-Dof parametrically excited model:
  - In addition to Simple and Primary parametric resonances, there exist instabilities due to the Combination parametric resonance.
  - Hill's method finds instabilities due to the Combination and Primary parametric resonances by employing the $2T$ periodic frequency components.
  - In implementing HBM and JBA, the consideration of the $2T$ periodic frequency components results in the transition curves enclosing the unstable responses due to the Primary parametric resonance.
  - To compute the transition curves locating the unstable responses due to the Combination parametric resonance using HBM and JBA, the Fourier series of the coordinates must contain two frequency components whose

ratio is irrational and their summation is equal to the frequency of the parametric excitation.

For stability analysis of a linear system under parametric excitation, JBA is highly advantageous and efficient over other approaches since it deals with a linear residual equation (please refer to Eq. (2.89)) which could be easily solved. JBA is beneficial for studying globally the stability of a parametrically excited system since:

- It functions in the frequency domain unlike Floquet theory
- It does not deal with any eigenvalue problem like Hill's method
- Unlike the direct implementation of HBM, JBA does not require solving a polynomial with an unknown to obtain the stability plot
- It does have as many mathematical difficulties as MMS specifically when the number of degrees of freedom increases.

Chapter 3

Application of the State-of-the-art and New Stability Analysis Methods on a Realistic Case Study

3.1 Introduction

Rolling element bearing (REB) is one of the most important components in rotating machineries whose undesirable vibrations can lead to serious damages or even failures. Parametric excitation induced by REB as a result of the so – called "Varying Compliance Vibration" could be one of the sources of such unwanted vibrations. This phenomenon i.e. "Varying Compliance Vibration" generates time – dependent stiffness which introduces the parametric excitation in rotating systems.

In section 3.2, the mathematical modeling of a Jeffcott rotor supported by the rolling bearings is explained. In this model, the bearings are modeled as springs whose stiffness changes with time. This results in a generation of parametric excitation within the system.

Then, in section 3.3, the stability analysis of the parametrically excited Jeffcott rotor is carried out. Here, a modified and improved version of the HBM used for the computation of the transition curves in the previous chapter (denoted in this chapter as Simple HBM or SHBM), is given.

The applicability of JBA, which is developed based on the forced response, to obtain the stability plot is investigated in section 3.4.

3.1 Jeffcott Rotor

In this section, a Jeffcott rotor model supported by the Rolling Element Bearing (REB) is taken into account. The scheme of the model is depicted in Figure 25A. In this figure M_d and R_d denotes the mass and the radius of the disk. Ω is the rotational speed of the shaft and the geometric and mass centers of the disk are indicated by o_{dc} and o_{dg} respectively. The disk's displacement coordinates are shown in Figure 25B. The following assumptions are adopted for this model (Tehrani, Gastaldi, and Berruti, 2021b)**:**

- The shaft is assumed to be massless;
- The axial displacement is neglected;
- The disk has no tilting motion hence the gyroscopic effect is negligible;
- The mass of the disk is lumped at its mass center;
- The system is symmetric with respect to the disk;
- The outer race of the REB is rigid and fixed within a rigid casing;
- The effective mass of the REB is negligible compared to the disk's mass;
- The REB's inner race displacement is negligible compared to the displacement of the disk

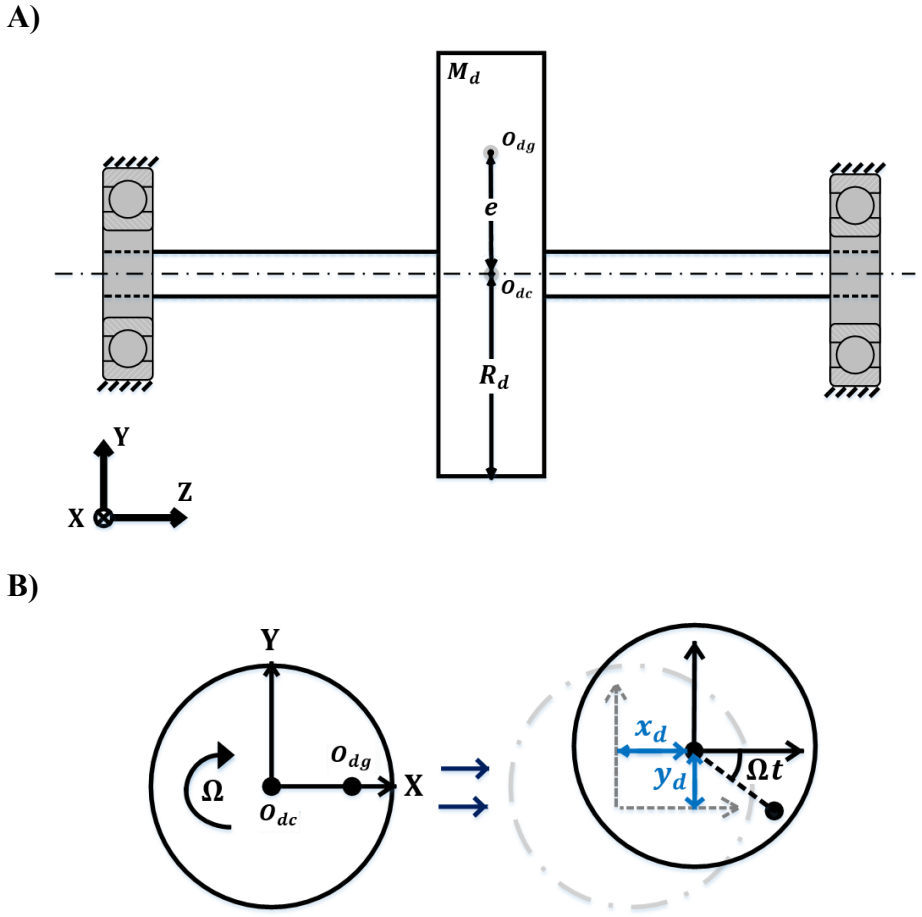

Figure 25: A) Jeffcott rotor model supported by REB, B) Displacement coordinates of the unbalance disk during rotation

In the following sections, the nonlinear contact forces of the REB using the well – known Hertz contact theory are first obtained. Then, through a proposed linearization procedure, the nonlinear contact forces are modeled as time – varying stiffnesses.

3.2.1 REB modeling (Hertz Contact Theory)

A model of REB with a fixed outer race and rotating inner race is shown in Figure 26. When the rotating inner race is loaded, some of the balls are put under compression. And, during the rotation (through time) of the inner race the position as well the number of the balls vary in the loading zone and results in alteration of the total contact force. This results in the change of the configuration in the loading zone, illustrated by Figure 26A, known as ‘Varying Compliance’, which induces

the so – called 'Varying Compliance Vibrations'. In the loading zone, depicted in Figure 26B, the balls at their lower position are under maximum force (pressure), denoted by F_{max}. The domain of the loading zone depends on the amount of the clearance and here it is considered to be zero which results in 180° loading distribution. At the line of 180°, shown by F_{min}, minimum load would be exerted on the balls. In Figure 26B, Ω represents the angular velocity of the inner race that is the same as the shaft, $(x_b\ , y_b)$ is the displacement coordinate of the inner race, ψ_i denotes the angular position of the ith ball with respect to the loading line (y axis). Here δ_i indicates the deformation of the ith ball due to the contact force which is expressed as (Harris, 2001):

$$\delta_i = k\left(x_b \sin\psi_i + y_b \cos\psi_i\right) , \tag{3.1}$$

where the contact (restoring) force based on Hertz theory is (Tiwari, Gupta, and Prakash, 2000):

$$F_{\psi_i} = k\delta_i^n = k\left(x_b \sin\psi_i + y_b \cos\psi_i\right)^n \tag{3.2}$$

Here k is the contact stiffness between the ball and races and for the sphere – sphere contact the Hertzian exponent n is equal to $3/2$ (Harris, 2001). The angular position is defined by (Metsebo *et al.*, 2016):

$$\psi_i = \frac{2\pi}{N_b}\left(i-1\right) + \theta_c , \tag{3.3}$$

where θ_c is the amount of angular rotation of the cage and is related to the rotational speed of the shaft Ω:

$$\theta_c = \Omega_c t = \left(\frac{D_I}{D_I + D_O}\right)\Omega t \tag{3.4}$$

In Eq. (3.4) Ω_c is the cage rotational speed and D_I and D_O represent the diameters of the inner and outer races respectively. According to the Hertz theory, the contact area between the balls and races has an ellipsoidal shape as depicted in Figure 26C (Harsha, 2005a).

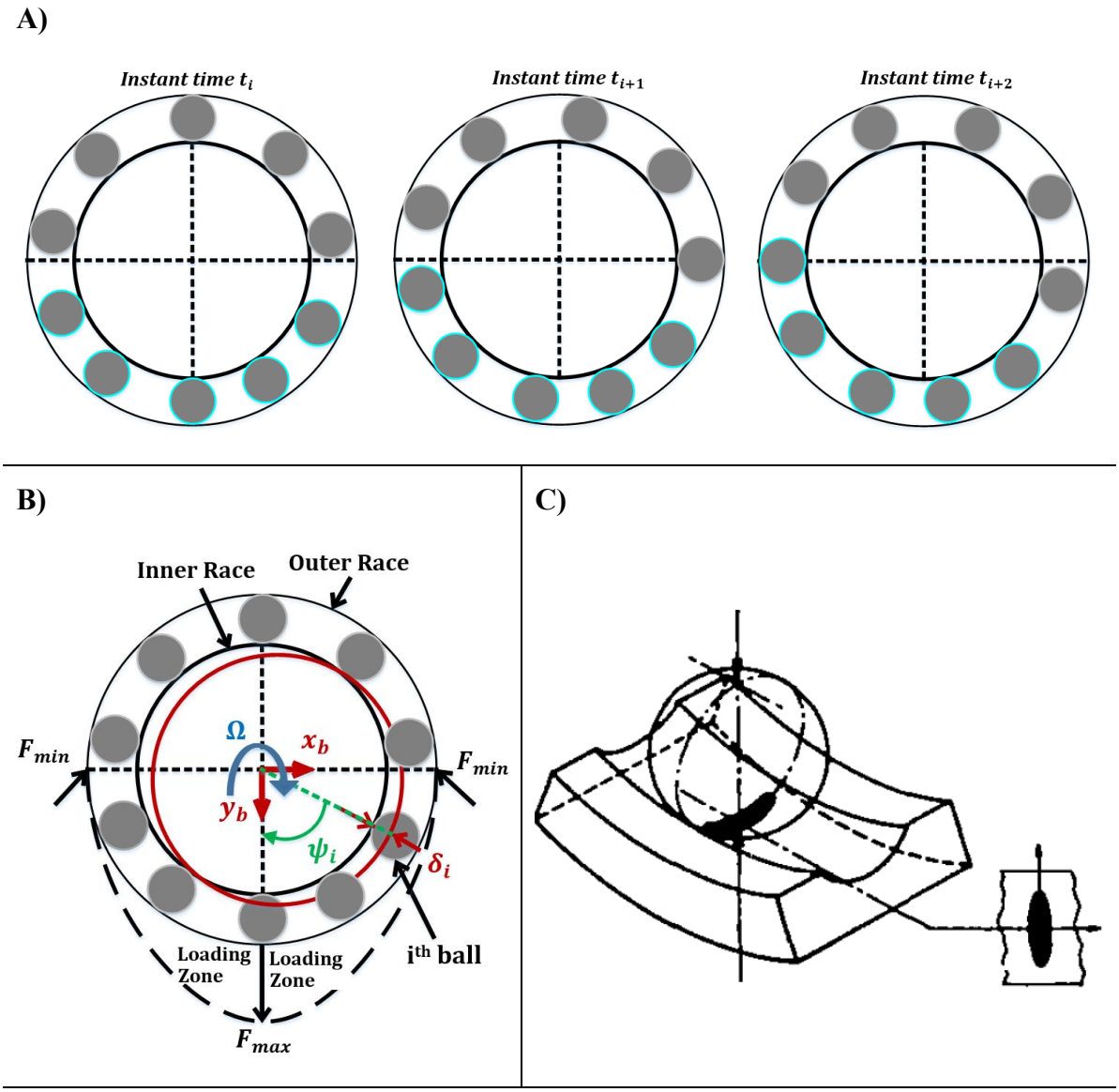

Figure 26: A) Loaded REB model, B) Varying compliance, C) Elliptical contact demonstration[1]

Computation of the contact stiffness k requires knowing the curvatures in the contact area and the curvature sum. To this end, the following steps are performed (Tehrani, Gastaldi, and Berruti, 2021b):

[1] The figure from B. J. Hamrock & W.J. Anderson, 'Rolling-Element Bearings', NASA REFERENCE PUBLICATION 1105, 1983

a) The local curvatures corresponding to the ball, inner and outer races are defined as (Harris, 2001):

$$\text{ball: } \alpha_X = \alpha_Y = \frac{1}{d_s} , \tag{3.5}$$

$$\text{inner race: } \beta_{XI} = \frac{1}{D_I}, \ \beta_{YI} = -\frac{1}{1.05 d_s} , \tag{3.6}$$

$$\text{outer race: } \beta_{XO} = -\frac{1}{D_O}, \ \beta_{YO} = -\frac{1}{1.05 d_s} , \tag{3.7}$$

where d_s is the diameter of the ball. The representation of the curvatures is given in Figure 27.

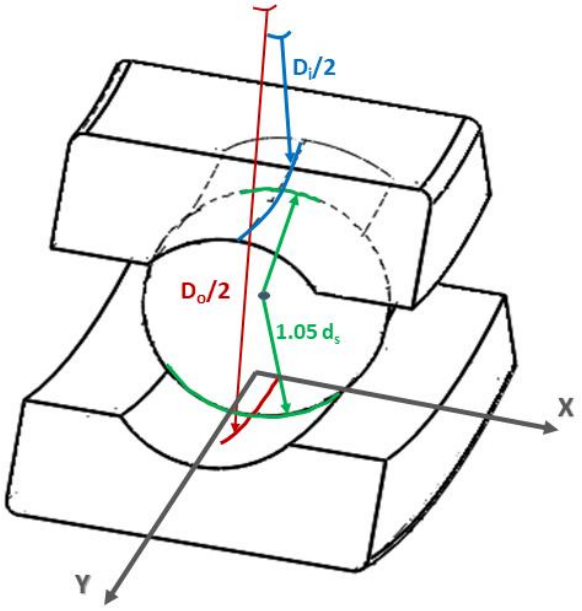

Figure 27: Corresponding curvatures of the contact area between one ball and races

According to (Hamrock and Anderson, 1983), the concave surface has the negative curvature sign while the convex one has the positive sign. The curvature sum is:

$$\sum \rho = \alpha_X + \alpha_Y + \beta_X + \beta_Y , \tag{3.8}$$

and is dependent on which contact to be considered. If for instance, the ball – inner race contact area is taken into account then Eq. (3.8) would be $\sum \rho = \alpha_X + \alpha_Y + \beta_{XI} + \beta_{YI}$.

b) To compute the deformation of the i[th] ball δ_i, the formula proposed by (David E. Brewe and Hamrock, 1977) is adopted:

$$\delta_i = 2.878\times10^{-8} F_i^{2/3} \left(\sum \rho\right)^{1/3} \delta^* \tag{3.9}$$

Here F_i is the contact force between the i[th] ball and the inner/outer race (neglecting the contribution of the centrifugal force). The formula of the dimensionless parameter δ^* is given in APPENDIX D.

c) Using Eq. (3.2), the contact stiffnesses corresponding to ball – inner/outer races are as follows:

$$\begin{aligned} K_{in} &= 3.587\times10^{7} \left(\sum \rho_{in}\right)^{-1/2} \left(\delta_{in}^*\right)^{-3/2} \\ K_{out} &= 3.587\times10^{7} \left(\sum \rho_{out}\right)^{-1/2} \left(\delta_{out}^*\right)^{-3/2} \end{aligned} \tag{3.10}$$

d) And, the equivalent stiffness at the ball – races contact is (Harsha, 2005b):

$$k = \left(\frac{1}{\frac{1}{K_{in}^{2/3}} + \frac{1}{K_{out}^{2/3}}} \right)^{3/2} \tag{3.11}$$

Then, using (3.2), the total contact forces in the orthogonal directions would be:

$$F_x = \sum_{i=1}^{N_b'} k\delta_i^{3/2} \sin\psi_i \tag{3.12}$$

$$F_y = \sum_{i=1}^{N_b'} k\delta_i^{3/2} \cos\psi_i \tag{3.13}$$

It must be noted that the contact forces are computed based on the balls under compression. In other words, only the balls in the loading zone would be in contact

while the rest do not have any contribution to the contact force. Therefore, in Eq. (3.12) and Eq. (3.13), N_b' denotes the number of the balls in the loading zone.

The contact forces are nonlinear in terms of the displacement coordinate as well as time – dependent due to the presence of ψ_i. In the following section, by proposing a linearization process, the contact forces are linearized around a constant preload.

3.2.2 Linearization of the contact force

In this section, it will be shown that by linearizing the contact forces in Eq. (3.12) and Eq. (3.13) around a constant preload $\bar{F}_y$, the nonlinear forces could be modeled as time – varying stiffnesses which introduce parametric excitation into the system. As a result, a linear relationship between the displacements of the inner race and contact forces is acquired which leads to less computational cost.

First, it is assumed that the bearing is just under the vertical displacement of the inner race designated by y_b which reduces Eq. (3.1) to (considering zero clearance):

$$\delta_i = y_b \cos\psi_i \tag{3.14}$$

Inserting Eq. (3.14) in Eq. (3.12) and Eq. (3.13) yields the following contact forces in the orthogonal directions:

$$F_x = y_b^{3/2}\left(\frac{1}{\frac{1}{K_{in}^{1/n}}+\frac{1}{K_{out}^{1/n}}}\right)^{3/2}\sum_{i=1}^{N_b'}\left(\cos\psi_i\right)^{3/2}\sin\psi_i = y_b^{3/2}K_{xy} \tag{3.15}$$

$$F_y = y_b^{3/2}\left(\frac{1}{\frac{1}{K_{in}^{1/n}}+\frac{1}{K_{out}^{1/n}}}\right)^{3/2}\sum_{i=1}^{N_b'}\left(\cos\psi_i\right)^{3/2}\cos\psi_i = y_b^{3/2}K_{yy} \tag{3.16}$$

By rotating the inner race and computing the contact forces from Eq. (3.15) and Eq. (3.16) at different times like t_{j-1}, t_j, t_{j+1} … the force – displacement plot could be obtained as depicted in Figure 28. It is worth mentioning that the contact forces are obtained based on the number of balls within the loading zone. According to

Figure 28, at the instant time t_j, the contact forces are plotted against an interval of inner ring displacement y_b. Then the subsequent procedure is followed:

I. First, an upper and lower bound of the preload, based on the working range of the bearing, are chosen, this corresponds to a range for y_b denoted as $\bar{y}_b$ in Figure 28.

II. Then, a first – order polynomial is fitted to the force – displacement curve based on the ranges of preload and displacement determined in step I.

III. Finally, the slope of the first – order polynomial fitted curve, representing the stiffness, is computed.

As depicted in Figure 28, the slopes of the fitted curve at the $F_Y - y_b$ and $F_X - y_b$ plots are direct and cross – coupling stiffnesses denoted respectively by K_{yy_L} and K_{xy_L} which are time – dependent.

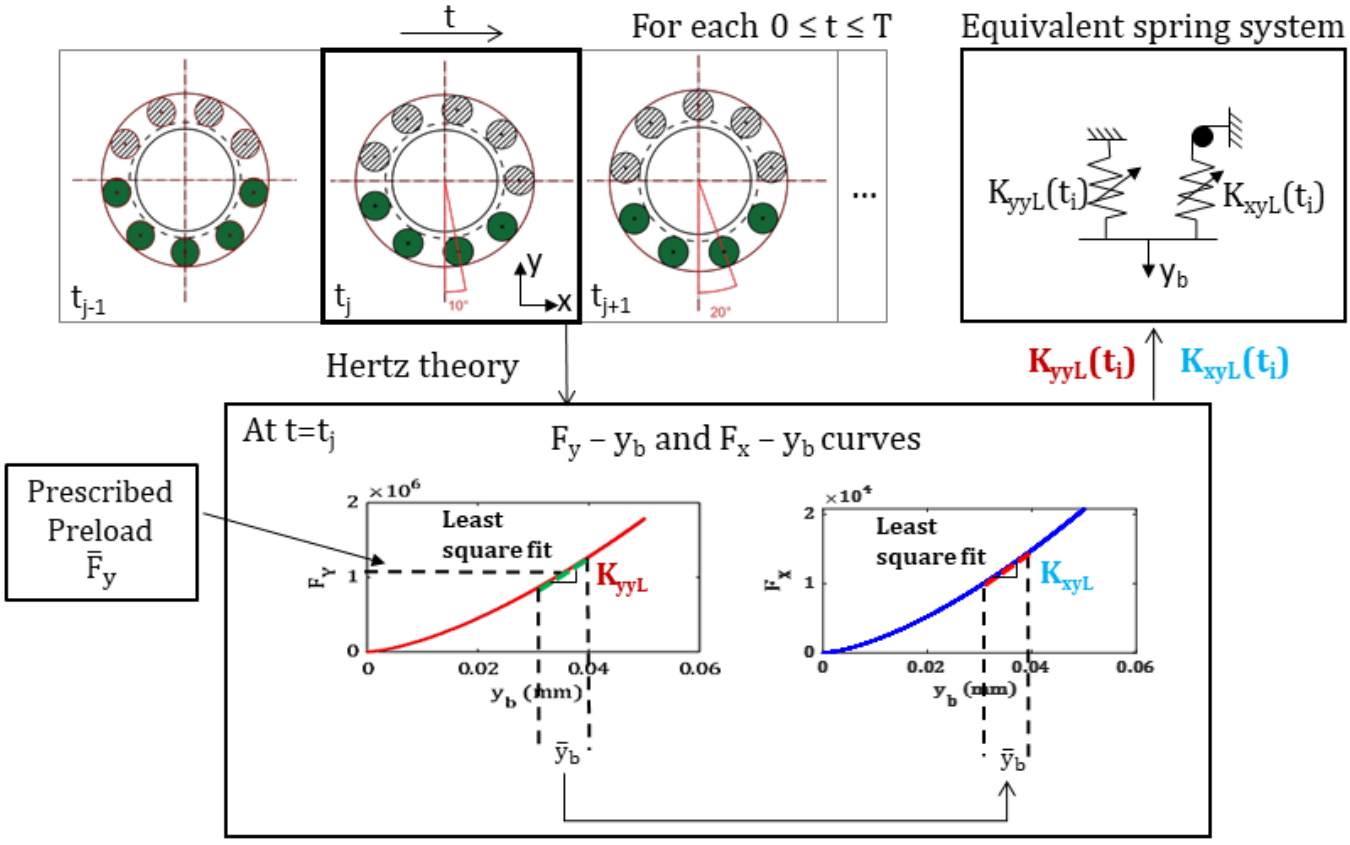

Figure 28: Equivalent time – varying stiffness by linearizing contact forces

Using the bearing values in Table 4 and collecting all the K_{yy_L} and K_{xy_L} for a timespan equivalent to 2π rotation of the inner race, the time signals and the corresponding FFTs of the resultant K_{yy_L} and K_{xy_L} are plotted and shown in Figure 29. According to Figure 29A, the direct stiffness is purely sinusoidal, a cosine signal, and its FFT in Figure 29B contains a zero harmonic/static term and a predominant harmonic denoted by K_{bm} and K_{bh}. According to this figure, the cross – coupling term is quasi sinusoidal with a sine – like signal and with regard to the FFT, it includes one predominant harmonic designated by K_{bc}. According to the FFT plots in Figure 29B, the period of the signals is $2\pi/N_b$ where N_b is the number of balls. The expression for the direct and cross – coupling stiffnesses are:

$$K_{yy_L} = K_{myy} - K_{dyy} \cos N_b \theta_c \tag{3.17}$$

$$K_{xy_L} = K_{dxy} \sin N_b \theta_c \tag{3.18}$$

By substituting θ_c from Eq. (3.4), $N_b \Omega_c$ is known as the 'varying compliance frequency' and here would be denoted by $\Omega_{vc} = N_b \Omega_c = \left(\frac{D_i}{D_i + + D_0}\right) \Omega$.

A)

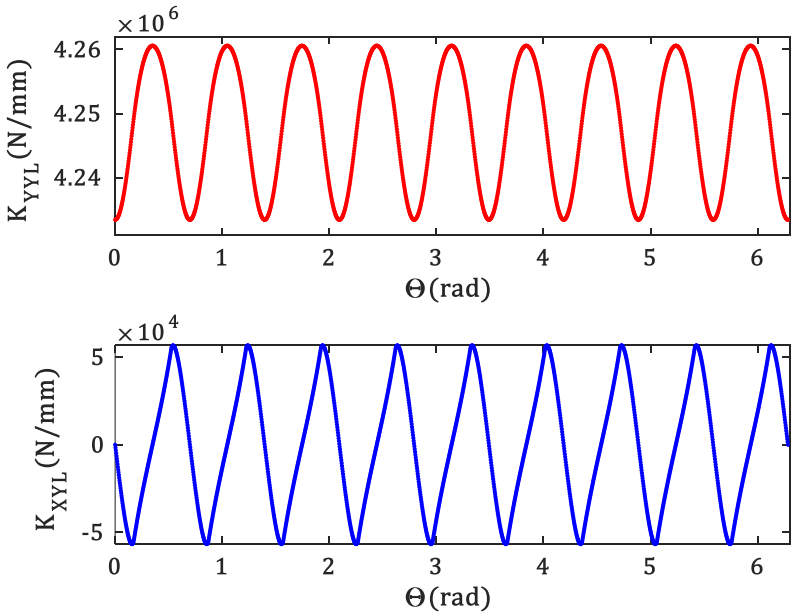

B)

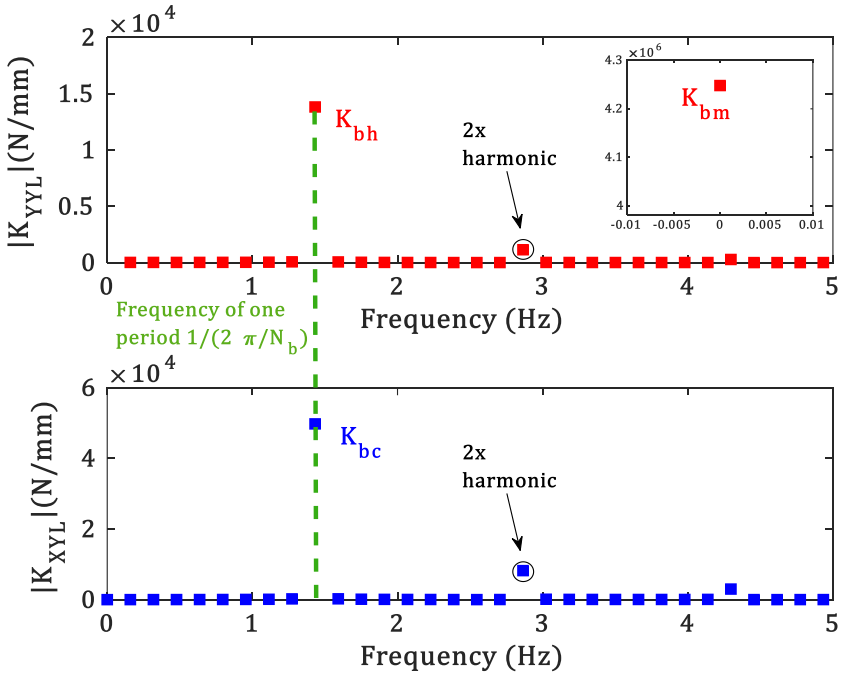

Figure 29: A) The sinusoidal behavior of the time – varying stiffness during a complete rotation of the inner race, B) FFT of the time – varying stiffness

Since there is a 90° of phase shift between the orthogonal directions i.e. x & y, the corresponding periodic siffnesses in the x direction would be acquired by $\pi/2$ rotation of Eq. (3.17) and Eq. (3.18). Then, the stiffness matrix of the REB could be expressed as:

$$K_b = \begin{bmatrix} K_{bm} + K_{bh}\sin\Omega_{vc}t & -K_{bc}\sin\Omega_{vc}t \\ -K_{bc}\cos\Omega_{vc}t & K_{bm} - K_{bh}\cos\Omega_{vc}t \end{bmatrix} \tag{3.19}$$

In the following section, the stability analysis of a Jeffcott rotor supported by REB, modeled as springs whose stiffness matrix is indicated by (3.19), would be carried out.

Table 4: Bearing specifications

REB	**Values**
D_I(m)	35.18×10^{-3}
D_O(m)	58.03×10^{-3}
d_s(m)	$\frac{D_O - D_I}{2}$
N_b	9

3.2.2 Governing Equations of motion of the Jeffcott rotor

Adopting the stiffness matrix in Eq. (3.19), the governing equations of motion are:

$$\begin{aligned} &M_d\ddot{x}_d + 2C\dot{x}_d + 2\left(K_{bM} + K_{bH}\sin\Omega_{vc}t\right)x_d + 2\left(-K_{bC}\sin\Omega_{vc}t\right)y_d \\ &= M_d e\Omega^2\cos\Omega t \end{aligned} \tag{3.20}$$

$$\begin{aligned} &M_d\ddot{y}_d + 2C\dot{y}_d + 2\left(K_{bM} - K_{bH}\cos\Omega_{vc}t\right)y_d + 2\left(-K_{bC}\cos\Omega_{vc}t\right)x_d \\ &= M_d e\Omega^2\sin\Omega t \end{aligned} \tag{3.21}$$

Here, the parameter C represents the overall damping of the system and parameters K_{bM}, K_{bH} and K_{bC} are given in APPENDIX E. It is worth mentioning that since the system is symmetric with respect to the disk, the stiffness and damping parts i.e. $(K_{bM} + K_{bH}\sin\Omega_{vc})$, $(-K_{bC}\sin\Omega_{vc})$, $(K_{bM} + K_{bH}\sin\Omega_{vc})$,

$(-K_{bC}\cos\Omega_{vc})$ and C in Eq. (3.20) and Eq. (3.21) refer to half of the system; therefore, their contribution is multiplied by a factor of two.

In the subsequent sections, first, the stability of the rotor system under parametric excitation is investigated and a modification of HBM is proposed. Here, the disk is assumed to have zero eccentricity ($e = 0$). Then, the forced response ($e \neq 0$) is taken into account where a new approach for stability analysis is developed.

3.3 Trained Harmonic Balance Method (THBM)

In this section, the stability of the rotor system under parametric excitation generated by the time – varying stiffnesses of the REB is investigated. For this study, the eccentricity of the disk is neglected i.e. $e = 0$. Here, M_d and Ω are adopted as the control parameters and the stability plot is presented on the (Ω, M_d) plane. In some cases, for clarifications, the varying compliance frequency Ω_{vc} is substituted by Ω. The values of the parameters in Table 4 and Table 5 are adopted for numerical calculations.

Table 5: the values of the parameters of the Jeffcott rotor

$\boldsymbol{K_{bm}}(\mathbf{N/m})$	$\boldsymbol{K_{bh}}(\mathbf{N/m})$	$\boldsymbol{K_{bc}}(\mathbf{N/m})$
4.23×10^9	1.35×10^7	5.65×10^7
$\boldsymbol{E}(\mathbf{GPa})$	$\boldsymbol{L}(\mathbf{m})$	$\boldsymbol{K_s}(\mathbf{N/m})$
200	$6D_O$	$\frac{48EI}{\left(\frac{L}{2}\right)^3}$

By implementing the state-of-the-art stability analysis approaches explained in chapter 2, i.e. Floquet theory, Hill's method, and HBM, a stability plot containing the results from these three approaches is obtained and depicted in Figure 30.

According to the results from Floquet theory, there are two unstable zones where the system's responses are unbounded. It is worth pointing out again that the Floquet theory analyses the system in the time domain by examining the modulus of the Floquet multipliers (eigenvalues of the Monodromy matrix) against 1, according to Eq. (2.19). It must be noted that the results obtained by Floquet theory are considered as the reference here.

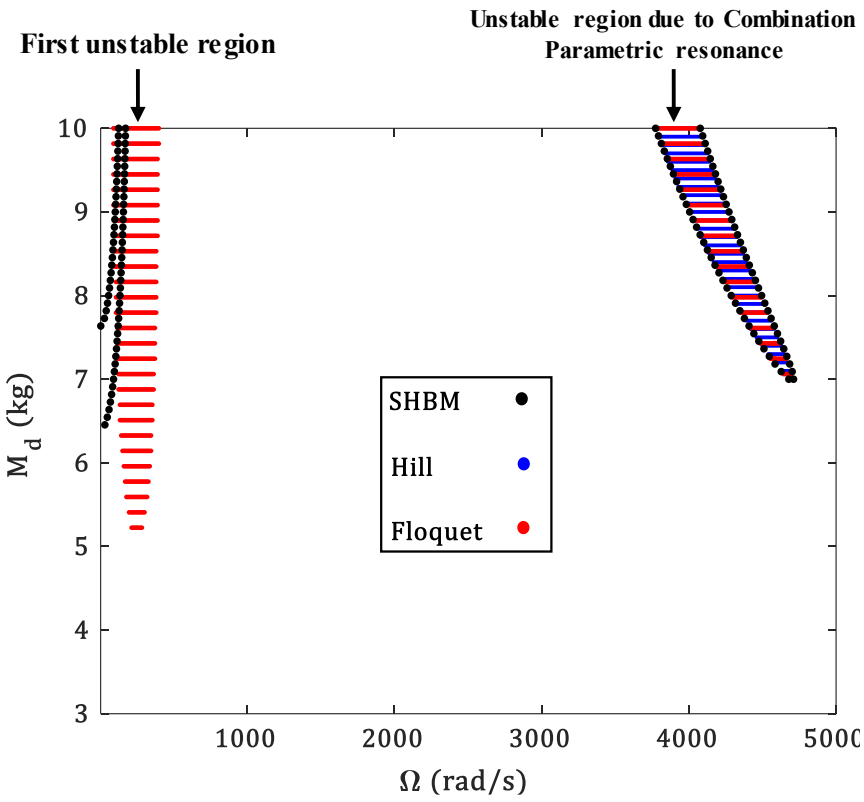

Figure 30: Stability plot of the Jeffcott rotor shown in the disk's mass (M_d) – disk's rotational speed (Ω) plane for $C = 2500$ N.m/s

Since the rotor system has two Dof, the occurrence of the instabilities due to both the Combination and Primary parametric resonances are expected. Therefore, the implementation of HBM is carried out by expressing the system's coordinates according to Eq. (2.33) and solving the determinants of Eq. (2.34) simultaneously. Doing so, the transition curves denoted by the black dots in Figure 30 are obtained. These transition curves are acquired due to the consideration of the frequency contents corresponding to ω_1 and ω_2 in Eq. (2.33) while the contribution of the T and $2T$ periodic components are null. It indicates that the second unstable zone is appeared as a result of the Combination parametric resonance. It can be concluded that in a parametrically excited system with two equal natural frequencies i.e. two identical mode shapes, here first two bending modes, the instability due to the combination parametric resonance is probable. According to Figure 30, in applying HBM, an inaccurate prediction of the first unstable region is given. Due to this, this approach is named 'Simple HBM (SBHM)'. Such inaccuracy is addressed later in this section.

Employing Hill's method where the system's coordinates are expressed by Eq. (2.46) and examining the modulus of the resultant Floquet exponents obtained by Eq. (2.52) results in finding an unstable zone presented by the blue dots in Figure 30. It is observable here that Hill's method accurately detects the second unstable zone while does not give any information about the first one. As pointed out earlier, in Figure 31, the second unstable zone is arisen due to the combination parametric resonance. As was observed and concluded in chapter 2, the presence of the $2T$ (here $T = 2\pi/\Omega_{vc}$) periodic frequency components allows Hill's method to find the second unstable zone in Figure 31.

According to the results in Figure 30, SHBM is not efficient enough to find the first unstable zone which does not attribute to any kind of parametric resonances. Detecting this area of unbounded responses is of importance since it occurs at low rotational speeds. In the following, the reason that SHBM fails in finding the first unstable has been investigated. Using this information, the SHBM has been trained and the Trained HBM (THBM) procedure is introduced.

According to the transition curves obtained by SHBM corresponding to the first unstable zone in Figure 30, one possibility of such inaccuracy could be because of considering wrong or imprecise frequency components in Eq. (2.33). To investigate this issue, a procedure described in Figure 31 is proposed. In this procedure, first, several trial points at the domain of interest, here the unstable regions, are selected. Then, by obtaining time responses and FFTs of those trial points, the domain of HBM formulation is identified. According to the FFT plots presented in Figure 32, the scope of HBM's applicability in obtaining the transition curves is recognized and demonstrated as a flow chart shown in Figure 31. According to this figure, the 'Simple Formulation' limits the HBM to find the transition curves corresponding to the second unstable zone. This zone is highlighted in red and corresponds to SHBM. On the other hand, by training the HBM by the 'General Formulation', represented by the blue area, both the unstable zones can be detected. The latter procedure, which is proposed in this study, is named 'Trained HBM (THMB)'.

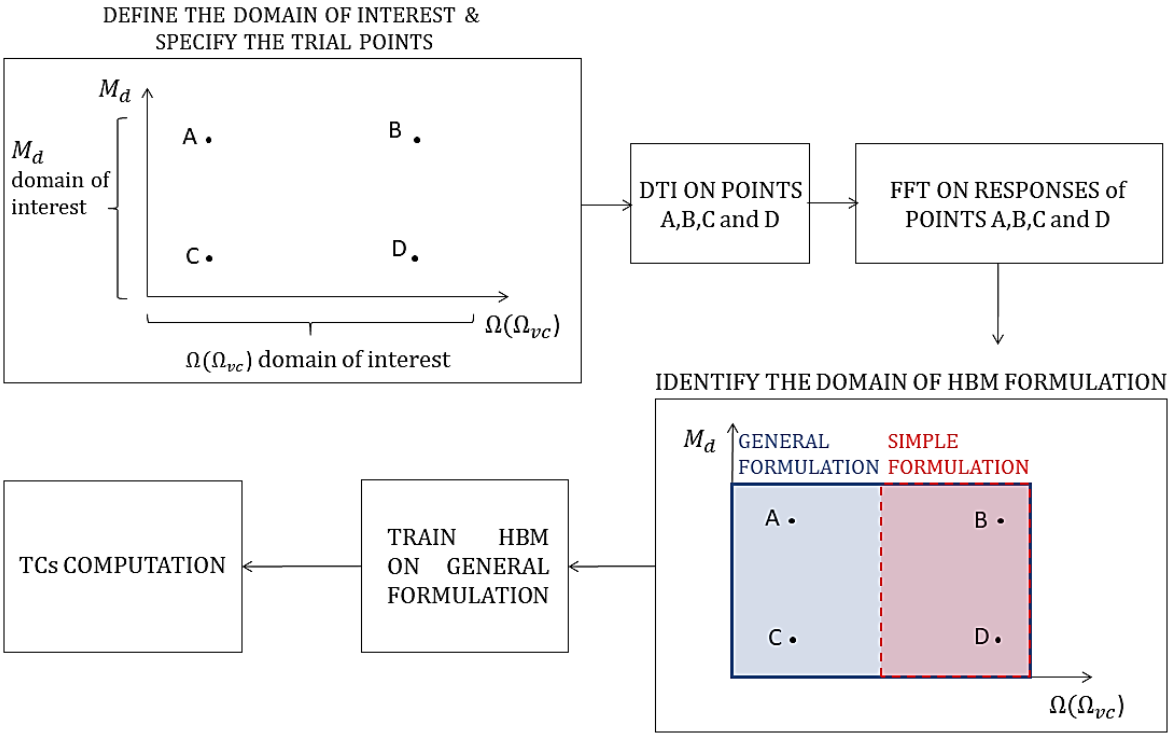

Figure 31: Investigation of the extra harmonics to adapt the SHBM for stability computation

To explore the frequency components of THBM, the FFT plot of two randomly chosen unbounded responses at the unstable regions are obtained and shown in Figure 32. According to Figure 32A, the FFT of the response has two sideband frequencies at a distance of Ω_{vc} from a leading frequency ω_c. In Figure 32B on the other hand, the response has two dominant frequencies whose summation is equal to Ω_{vc}. As already observed in chapter 2, such a FFT plot is typical of unstable responses resulted from combination parametric resonances. In THBM, the coordinates of the system are expressed by Fourier series containing the frequency components taken from the 1st unstable zone given in Figure 32A:

$$x_d = a_1 \cos \omega_L t + b_1 \sin \omega_L t + a_2 \cos \omega_c t + b_2 \sin \omega_c t + a_3 \cos \omega_R t + b_3 \sin \omega_R t \qquad (3.22)$$

$$y_d = c_1 \cos \omega_L t + d_1 \sin \omega_L t + c_2 \cos \omega_c t + d_2 \sin \omega_c t + c_3 \cos \omega_R t + d_3 \sin \omega_R t \ , \qquad (3.23)$$

where:

$$\begin{aligned} \omega_L &= \omega_c - \Omega_{vc} \\ \omega_R &= \omega_c + \Omega_{vc} \end{aligned} \qquad (3.24)$$

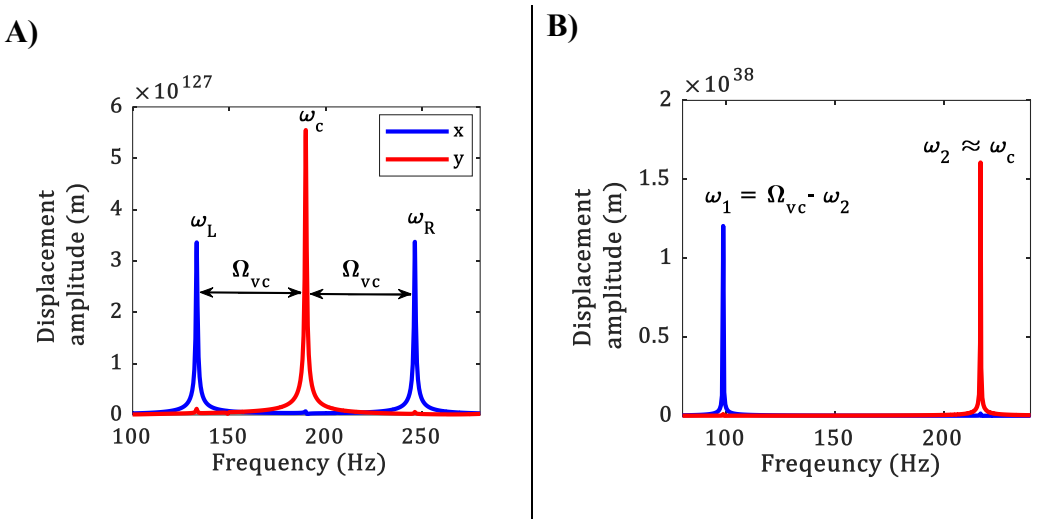

Figure 32: Sample FFT of the responses for $C = 2500$ N.m/s and at **A)** First and **B)** Second unstable zones

Considering Figure 32, since the frequency component ω_c is more significant with respect to frequencies ω_L and ω_R for y_d and less notable comparing to ω_L and ω_R for x_d, it is possible to simplify Eq. (3.22) and Eq. (3.23) by setting the coefficients $a_2 = b_2 = c_1 = d_1 = c_3 = d_3 = 0$.

By injecting the resultant coordinates from Eq. (3.22) and Eq. (3.23), considering $a_2 = b_2 = c_1 = d_1 = c_3 = d_3 = 0$, in the governing equations of motion and balancing the terms of the same harmonics, an algebraic equation similar to Eq. (2.31) would be obtained. Here, the Jacobian matrix $[J]$ is considered to be a function of ω_c and Ω_{vc}. By solving the two determinants of Eq. (2.34) simultaneously, the transition curves would be acquired as demonstrated in Figure 33. Compared to the Floquet results, the first transition curve has the same shape as the corresponding unstable zone but encompasses a wider area. In other words, THBM is conservative in predicting the first unstable zone. The result for the second unstable zone is the same as the one obtained by applying SHBM.

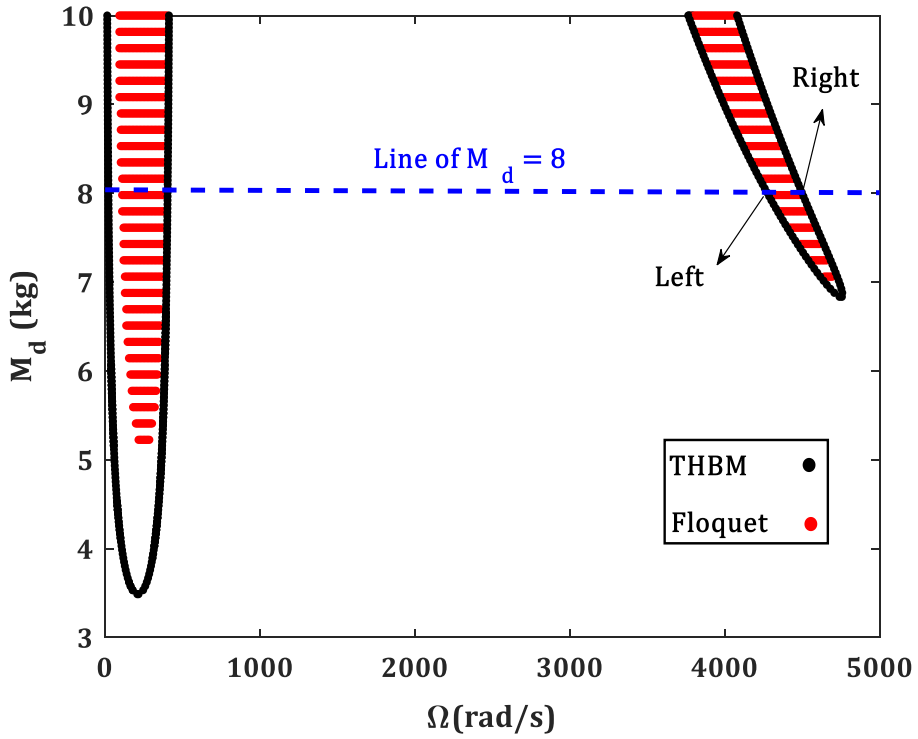

Figure 33: Comparison of the unstable zones computation using THBM and Floquet Theory for $C = 2500$ N.m/s

In Figure 32B, referring to the second unstable zone, the frequency ω_2 is claimed to be almost equal to ω_c. To confirm this, the values of ω_1, ω_2 and ω_c are obtained for a specific case at $M_d = 8$ kg on the second transition curve, as shown by the dashed blue line in Figure 33. The intersections of this line with the transition curves are called 'Left' and 'Right'. The values of ω_1 and ω_2 are computed by SHBM (using Eq. (2.33) given in Chapter 2), while the value of ω_c is computed by THBM (using Eq. (3.22) and Eq. (3.23) given in the current Chapter). These values are presented in Figure 34. It is observable that the frequencies ω_2 and ω_c are almost equal to each other at the 'Left' and 'Right' intersections. This implies that $\omega_1 = |\Omega_{vc} - \omega_2|$ can be written as $\omega_1 \approx |\Omega_{vc} - \omega_c|$. This is the reason why, even without knowing the frequencies ω_1 and ω_2, THBM allows to find, in addition to the first unstable zone, the second area of instability characterized by the frequencies ω_c and $\Omega_{vc} - \omega_c$ (please refer to Figure 32B).

It is worth noting that using THBM allows the computation of the transition curves even with unknown frequency content(s) while it is not the case in utilizing Hill's method.

On the other hand, the main drawback of applying THBM is the high computational time specifically when the numbers of harmonics and Dof increase. The main motivation of the next section is to overcome this issue by proposing a new approach based on the forced response analysis.

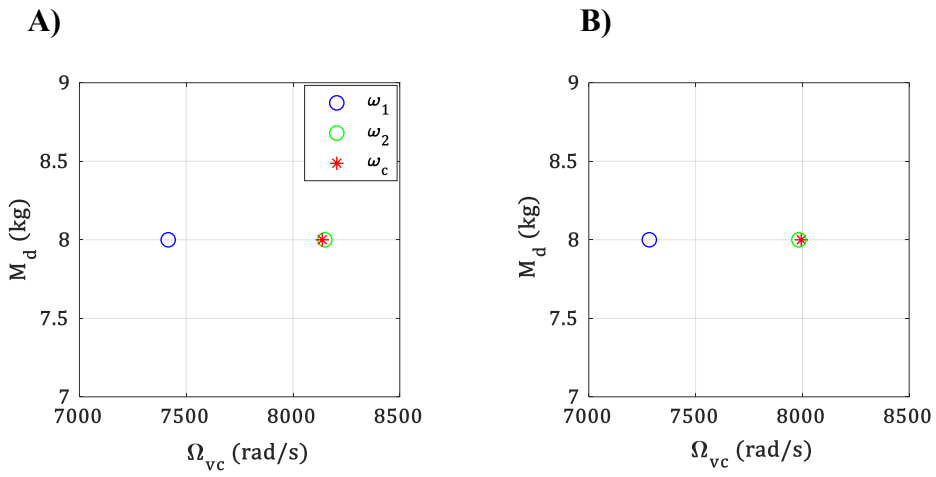

Figure 34: the values of the frequencies ω_1 ,ω_2 obtained by SHBM and ω_c obtained by THBM for $C = 2500$ N.m/s and at the intersection of the line of $M_d = 8$ kg and the left transition curve corresponding to the labels(intersections) **A)** "Left" and **B)** "Right" shown in Figure 33

3.4 Jacobian Based Approach (JBA)

As was observed previously, to obtain the transition curves using THBM, the determinants of the Jacobian matrix and its highest minor must be solved. Since the determinants are polynomials, increasing the numbers of harmonics or Dofs results in the increment of the order of the polynomials and higher computational time.

In this section, the implementation of JBA to obtain the stability plot associated to the Jeffcott rotor is explained in detail. To initiate, the Jeffcott rotor induced by the eccentric force of the disk ($e \neq 0$ in Eq. (3.20) and Eq. (3.21)) is taken into account. The analysis is performed for $M_d = 8$ kg and $e = 3 \times 10^{-3}$m. Since the system is under two exciting forces, parametric excitation and eccentricity force, the frequency content of the system is based on Table 6.

Table 6: Frequency contents

Dominant Frequency components	ω_c	$\omega_c - \Omega_{vc}$	$\omega_c + \Omega_{vc}$	Ω	Ω_{vc}	$\Omega - \Omega_{vc}$	$\Omega + \Omega_{vc}$
Unstable zone	×	×	×				
Stable zone				×	×	×	×

In Table 6, the frequency components at the unstable zone relate to the frequency contents of the unbounded responses due to the parametric excitation as was noticed in the previous section. While the stable zone comprises the converging responses whose frequency contents are associated with the forcing frequencies and their combination (Haslam, Schwingshackl, and Rix, 2020). Adopting these frequencies, the system's coordinates are expressed as follows:

$$\begin{aligned} x_d = &\begin{bmatrix} a_1\cos\Omega t + b_1\sin\Omega t + a_2\cos\Omega_{vc}t + b_2\sin\Omega_{vc}t + a_3\cos\left(\Omega_{vc}-\Omega\right)t \\ +b_3\sin\left(\Omega_{vc}-\Omega\right)t + a_4\cos\left(\Omega_{vc}+\Omega\right)t + b_4\sin\left(\Omega_{vc}+\Omega\right)t \end{bmatrix} \\ &+\begin{bmatrix} a_5\cos\omega_c t + b_5\sin\omega_c t + a_6\cos\left(\omega_c-\Omega_{vc}\right)t + b_6\sin\left(\omega_c-\Omega_{vc}\right)t \\ +a_7\cos\left(\omega_c+\Omega_{vc}\right)t + b_7\sin\left(\omega_c+\Omega_{vc}\right)t \end{bmatrix} \end{aligned} \tag{3.25}$$

$$\begin{aligned} y_d = &\begin{bmatrix} a_8\cos\Omega t + b_8\sin\Omega t + a_9\cos\Omega_{vc}t + b_9\sin\Omega_{vc}t + a_{10}\cos\left(\Omega_{vc}-\Omega\right)t \\ +b_{10}\sin\left(\Omega_{vc}-\Omega\right)t + a_{11}\cos\left(\Omega_{vc}+\Omega\right)t + b_{11}\sin\left(\Omega_{vc}+\Omega\right)t \end{bmatrix} \\ &+\begin{bmatrix} a_{12}\cos\omega_c t + b_{12}\sin\omega_c t + a_{13}\cos\left(\omega_c-\Omega_{vc}\right)t + b_{13}\sin\left(\omega_c-\Omega_{vc}\right)t \\ +a_{14}\cos\left(\omega_c+\Omega_{vc}\right)t + b_{14}\sin\left(\omega_c+\Omega_{vc}\right)t \end{bmatrix} \end{aligned} \tag{3.26}$$

Inserting Eq. (3.25) and Eq. (3.26) in the equations of motion and balancing the terms with the same harmonics yields the following algebraic equations:

$$\{R\} = [J_1]\{U_1\} - \{F\}\ , \tag{3.27}$$

where $[J_1]$ is the Jacobian matrix, $\{U_1\} = \{a_1, a_2, \dots, b_{13}, b_{14}\}^T$ is the vector of each harmonic amplitude and $\{F\}$ and $\{R\}$ are the forcing and the residual vectors respectively. To obtain the frequency response, the residual must be close to zero; hence:

$$\{U_1\} = [J_1]^{-1}\{F\} \tag{3.28}$$

By determining the $\{U_1\}$ in Eq. (3.28) for each value of Ω and computing its modulus, the frequency response curve shown in Figure 35 is obtained. This plot contains one peak at Ω ≈ 7485 rad/s, denoted by point C, which corresponds to the natural frequency of the system according to the Campbell diagram in Figure 36. The difference in the values is because the peak C in Figure 35 designates the damped natural frequency whereas the undamped natural frequency is presented by the Campbell diagram in Figure 36.

Furthermore, the frequency response possesses two small peaks at lower frequencies denoted by points A and B. These extra modes that are generated due to the varying compliance phenomena (Yang *et al.*, 2018), and negligible compared to the main mode of the system, are not present in the Campbell diagram of Figure 36.

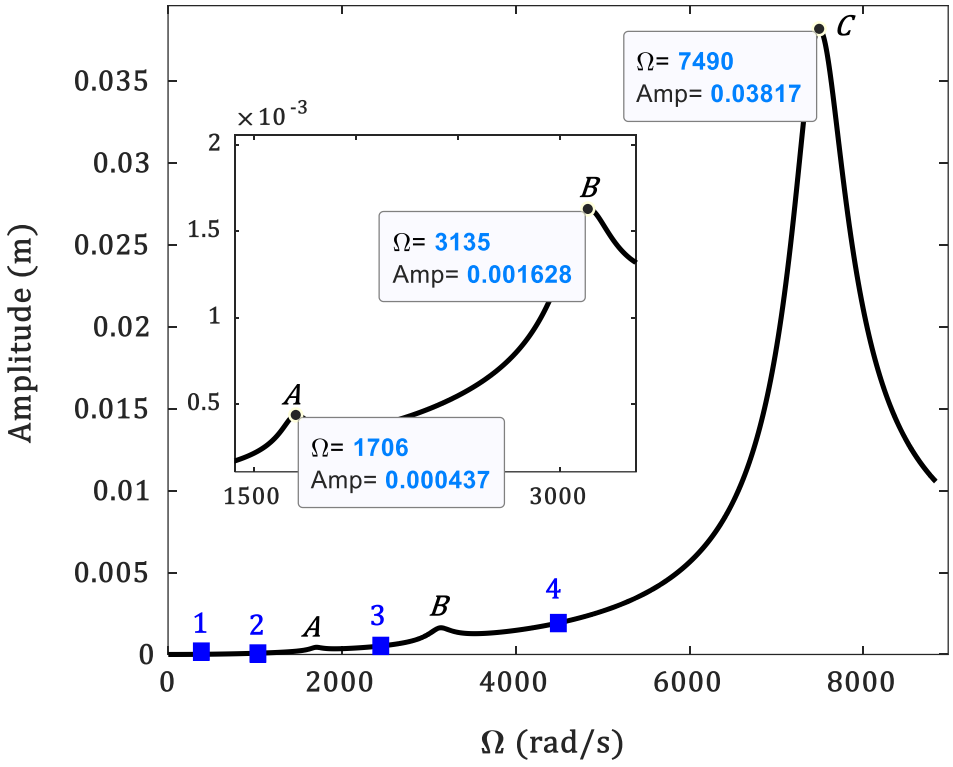

Figure 35: Frequency response of the system for $M_d = 8$ kg and $C = 2500$ N.m/s

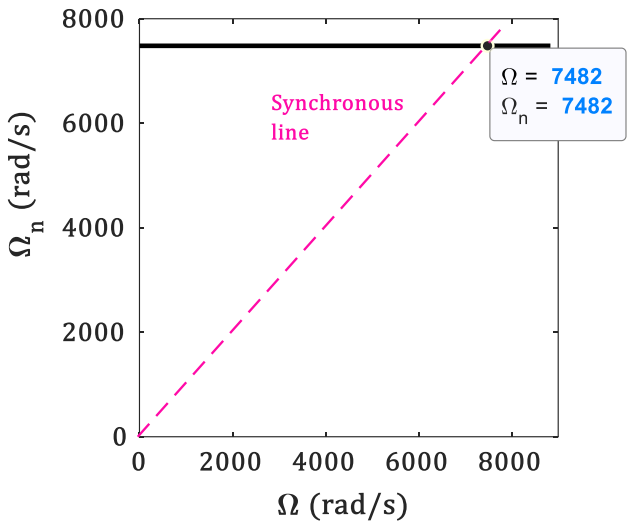

Figure 36: Campbell diagram for $M_d = 8$ kg and $C = 2500$ N.m/s

The Campbell diagram of Figure 36 has been obtained by computing the eigenvalues of the mass and stiffness matrices where the time – varying part of the stiffness was disregarded. As already observed, no horizontal lines corresponding to peaks A and B in Figure 23 are visible. To obtain a Campbell diagram giving all the possible modes, the time – dependent parts of the stiffness matrix must be taken into account. A practical way to include these time – dependent parts, is to make use of the Jacobian matrix $[J_1]$ (Tehrani, Gastaldi and Berruti, 2021a).

To proceed, first, the spy plot of Eq. (3.28) organized by its frequency components is presented in Figure 37. Here, the frequency contents indicated by the purple, orange, and green boxes correspond respectively to the static terms, stable and unstable responses. The governing equation of the orange block matrix including the responses at peaks A, B, and C is:

$$[J_S]^{-1}\begin{Bmatrix} U_{\Omega} \\ U_{\Omega_{vc}} \\ U_{\Omega_{vc}-\Omega} \\ U_{\Omega_{vc}+\Omega} \end{Bmatrix} = \begin{Bmatrix} F_{\Omega} \\ F_{\Omega_{vc}} \\ F_{\Omega_{vc}-\Omega} \\ F_{\Omega_{vc}+\Omega} \end{Bmatrix}, \tag{3.29}$$

where:

$$[J_S]^{-1} = -\Omega^2[M_S] + i\Omega[C_S] + [K_S] \tag{3.30}$$

Here, the mass $[M_S]$ and damping $[C_S]$ matrices are diagonal while the stiffness matrix $[K_S]$ contains off – diagonal elements due to the presence of the cross – coupling terms as shown in Eq. (3.19). The comprehensive Campbell diagram in Figure 38, including the modes due to the parametric excitation, is obtained through an eigenvalue analysis using the stiffness, damping, and mass matrices of Eq. (3.30) . According to Figure 38, the presence of the eigenfrequencies related to the parametric excitation i.e. point A and B in Figure 35, is due to considering the time-dependent stiffness terms. As observed earlier, since the difference between the damped and undamped natural frequencies are not significant, the undamped ones (those related to K_S, M_S) are plotted in Figure 38. The damped natural frequencies can be easily obtained by adopting a state-space representation where the matrix C_S is considered in the eigenvalue computation.

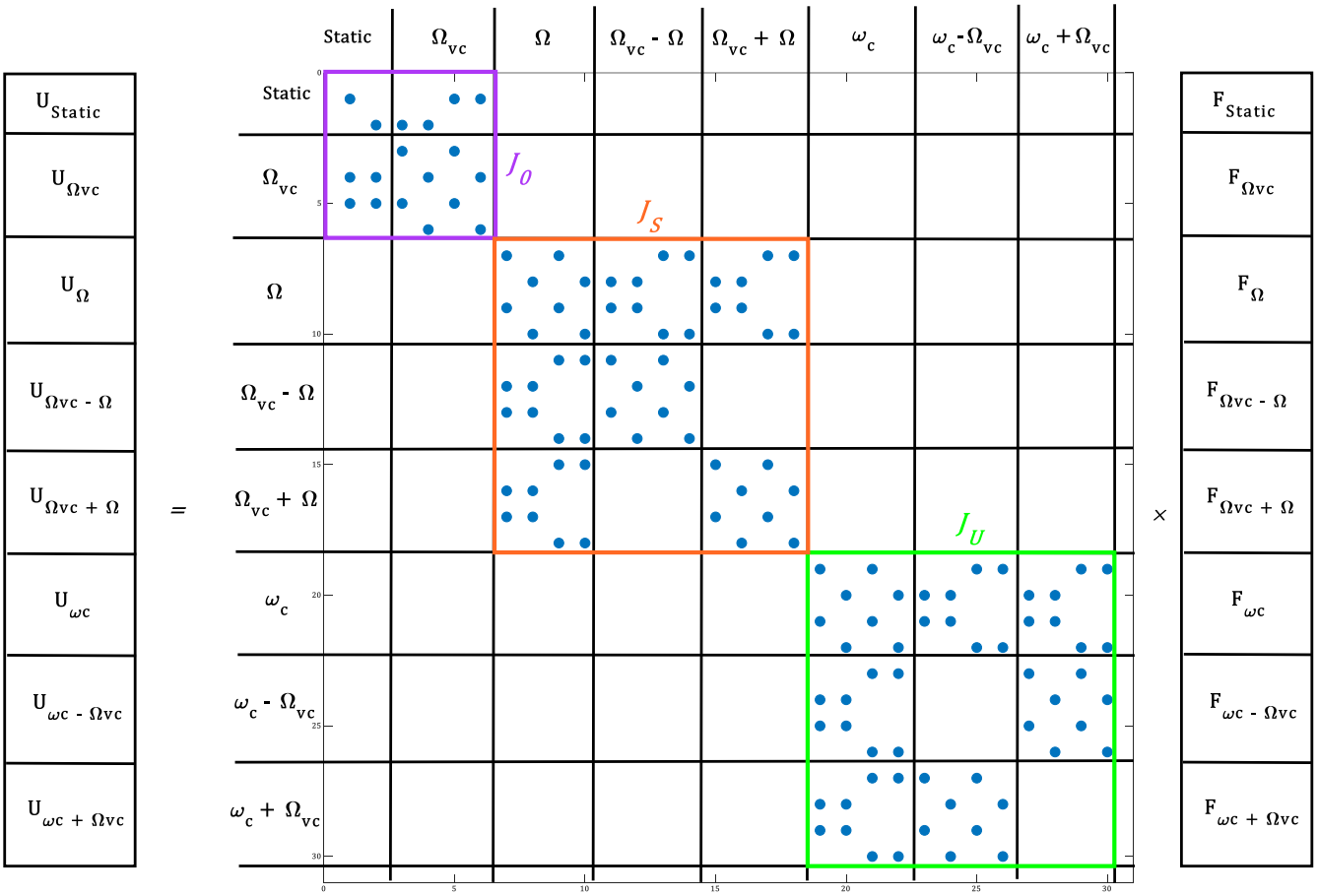

Figure 37: Spy plot of the inverse of the Jacobian matrix for $M_d = 8$ kg and $C = 2500$ N.m/s

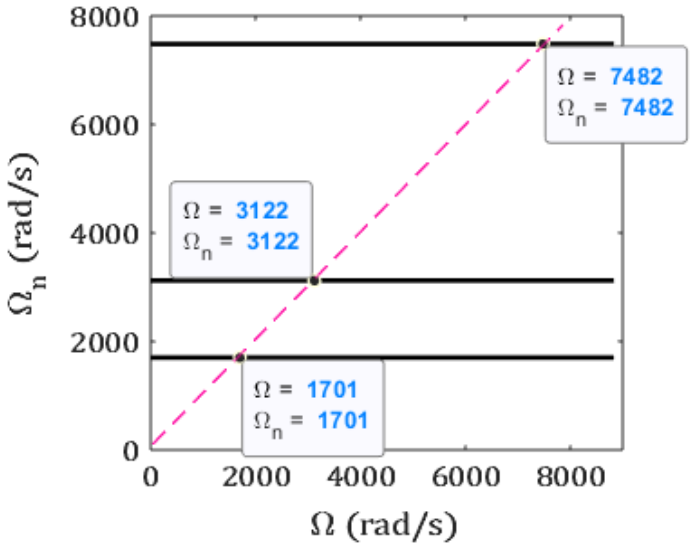

Figure 38: Campbell diagram obtained by using the mass and stiffness matrices from HBM for $M_d = 8$ kg and $C = 2500$ N.m/s

To check the accuracy of the HBM, the time responses of the trial points 1, 2, 3, and 4 picked from the frequency response in Figure 35, are obtained via HBM and DTI (direct time integration) and demonstrated in Figure 39. Here, at points 1 and 3 the time signals from HBM well match the ones obtained by DTI. On the other hand, the responses at points 2 and 4, intentionally chosen at the unstable zones, diverge according to DTI whereas based on HBM are bounded.

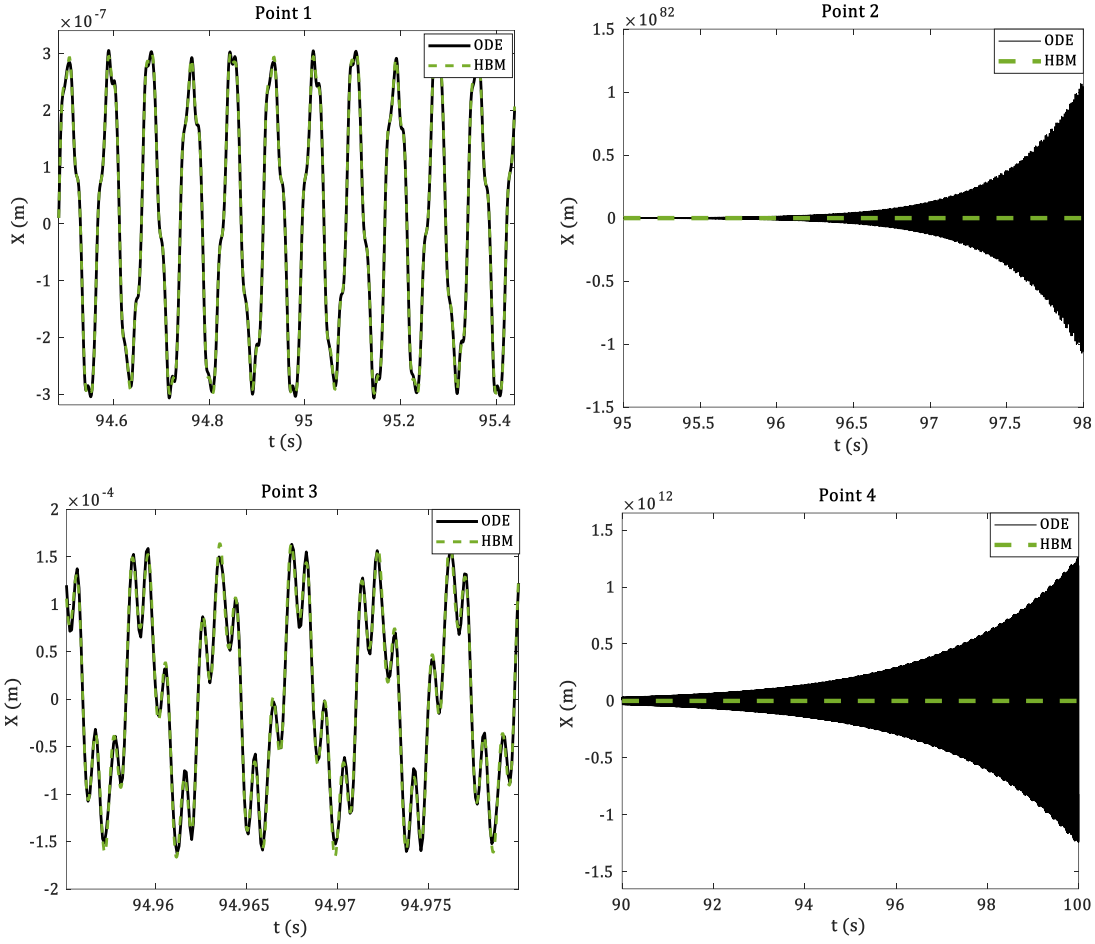

Figure 39: Time response of the sample points in Figure 35 obtained by direct time integration and HBM f for $M_d = 8$ kg and $C = 2500$ N.m/s

To better investigate such inaccuracy of HBM, the frequency response of the system in Figure 35 is presented based on its frequency components as shown in Figure 40. In this figure, the components representing the stable responses, Figure 40a and Figure 40b, are present; however, the ones corresponding to the unstable responses, Figure 40c, are null. This explains why the frequency response in Figure 35 and also the time responses of points 1 and 2 in Figure 39 do not contain any information about the instabilities induced by the parametric excitation. In the following, the solution to solve this deficiency is addressed.

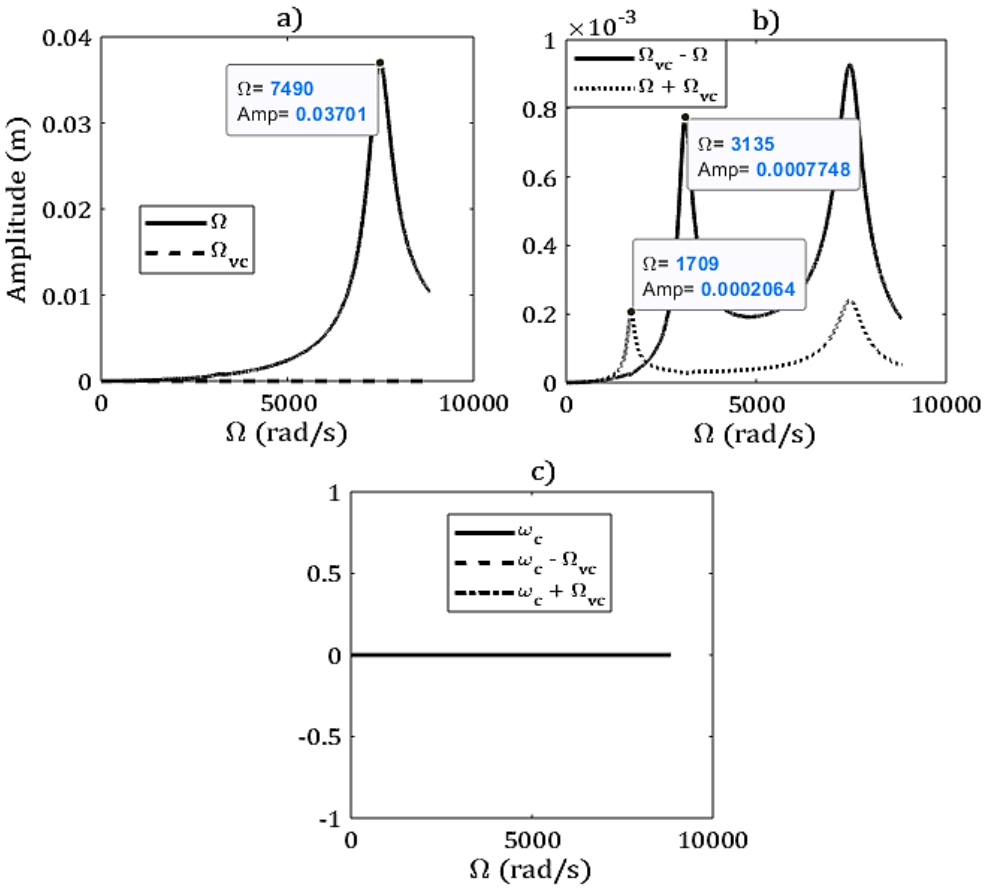

Figure 40: Discrete demonstration of the frequency response based on the frequency components **a)** Ω & Ω_{vc}, **b)** $\Omega_{vc}-\Omega$ & $\Omega_{vc}+\Omega$ and **c)** ω_c, ω_c - Ω_{vc} & $\omega_c+\Omega_{vc}$ considered in HBM given in Table 10 for $M_d = 8$ kg and $C = 2500$ N.m/s

It is worth mentioning that the peak in Figure 40a corresponds to the natural frequency of the system as denoted by point C in Figure 35. In addition, in Figure 40b the first peaks of the dotted and solid curves are associated respectively with peaks A and B in Figure 35.

To solve the issue related to the absence of instability due to the parametric excitation within the frequency response JBA is implemented. To do so, first, Eq. (3.28) is rewritten as:

$$\begin{Bmatrix} U_0 \\ U_S \\ U_U \end{Bmatrix} = \begin{bmatrix} J_0 & 0 & 0 \\ 0 & J_S & 0 \\ 0 & 0 & J_U \end{bmatrix} \begin{Bmatrix} F_0 \\ F_S \\ F_U \end{Bmatrix}, \tag{3.31}$$

where, the indices 0, S and, U represent the static terms and frequency components related to the stable and unstable responses respectively. Due to the null contribution of the Ω_{vc} component shown in Figure 40a, it is placed in the J_0 block. It is evident from Eq. (3.31) that stable and unstable responses are fully uncoupled; accordingly, the unstable responses U_U could not be excited by the force vector corresponding to the stable responses F_S. In order to be able to trigger the vector U_U, at least one of the entries of the vector F_U must be nonzero.

For the current system, the key information required to implement JBA is to know the value of the leading frequency ω_c. To this end, the values of ω_c on the transition curves computed by THBM are presented in Figure 41. According to this figure, ω_c has unique values on the transition curves corresponding to the first unstable zone while its values vary on the transition curves encompassing the second unstable zone. Here the purple dots represent the values of the natural frequency ω_n of the system without parametric excitation (Equivalent to point C in Figure 35). As is noticeable, the values of ω_c in the first unstable region is almost equal to ω_n; while in the second unstable region the values of the ω_c at the left side of the transition curve are close to ω_n. Accordingly, for this study ω_c is equated to the corresponding ω_n at $M_d = 8$kg.

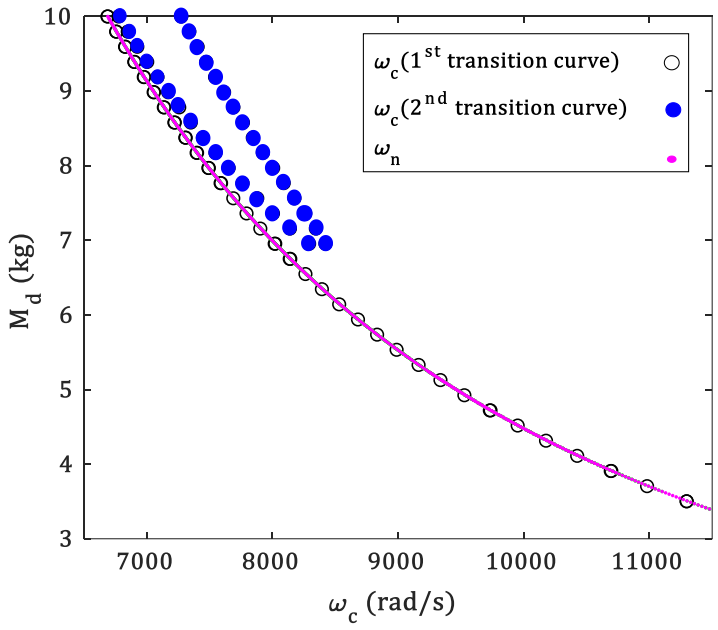

Figure 41: The values of ω_c at first and second transition curves using THBM for $C = 2500$ N.m/s

Applying JBA by assigning a sinusoidal force with the ω_c component and a unit amplitude to F_{ω_c}, the results are obtained and demonstrated in Figure 42. It must be noted that since the contributions of the frequency components Ω, Ω_{vc} and $\Omega \pm \Omega_{vc}$, shown in Figure 40, remain unchanged, they are not presented in Figure 42.

According to Figure 42a), the frequency response of the ω_c component contains two peaks at frequencies equal to the ones at the intersections of the $M_d = 8$kg line and the first transition curve obtained by THBM. These two peaks determine the borders of the first unstable zone, within the frequency response, whose inside area contains the unstable responses. Furthermore, as shown in Figure 42b), there are two other peaks at higher rotational speeds which correspond to the second unstable zone. Compared to THBM, here JBA is predicting a bigger area of instability (more conservative) at the second unstable zone; this is because the chosen value of ω_c, ω_n, is not precise at this region as stated in Figure 41. The domain of this area is represented by the dashed green lines while the ones corresponding to the actual domain of instability are demonstrated by the red dashed lines.

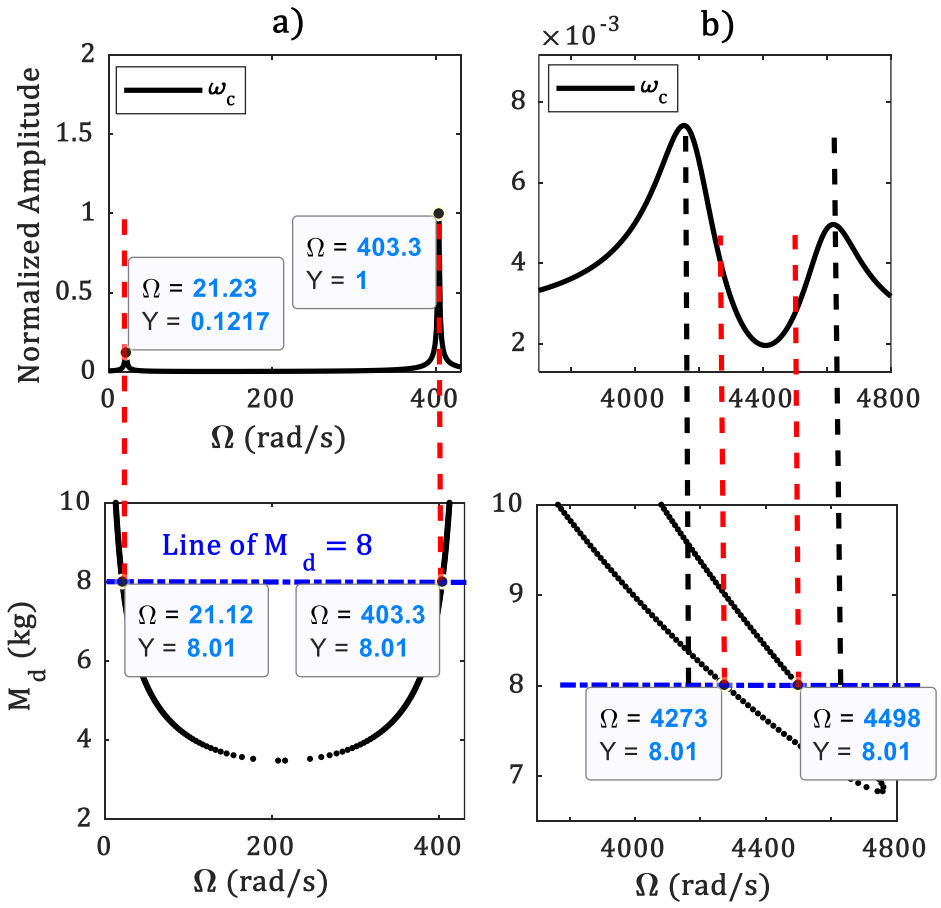

Figure 42: Illustration of the instability borders in the frequency response using JBA for $M_d = 8$ kg and $C = 2500$ N.m/s

As observed in this chapter and also in chapter 2, implementation of HBM allows to find just the transition curves where the responses are periodic and bounded; however, no information about the inside zone is given. Since JBA originates from HBM, implementing this approach results in obtaining a frequency response containing peaks at frequencies equal to the ones of the transition curves.

To obtain the full stability plot via JBA, the following steps must be taken:

a) Perform the JBA for different values of M_d for an interval of Ω
b) For each M_d, build the JBA plot (like in Figure 42)
c) Collect the frequency values corresponding to the peaks demonstrating the domains of instabilities
d) Plot the collected points from the previous step

By performing the procedure above, the transition curves acquired by JBA are demonstrated in Figure 43. According to this figure, the first transition curve obtained by JBA completely overlaps the one from THBM while is conservative compared to the result from Floquet theory. On the other hand, the second transition curve resulted from JBA predicts a wider area of instability which encompasses the domain of instability obtained by THBM and Floquet theory. This is because the value of the ω_c used here in JBA is accurate for the first unstable zone while not for the second unstable zone.

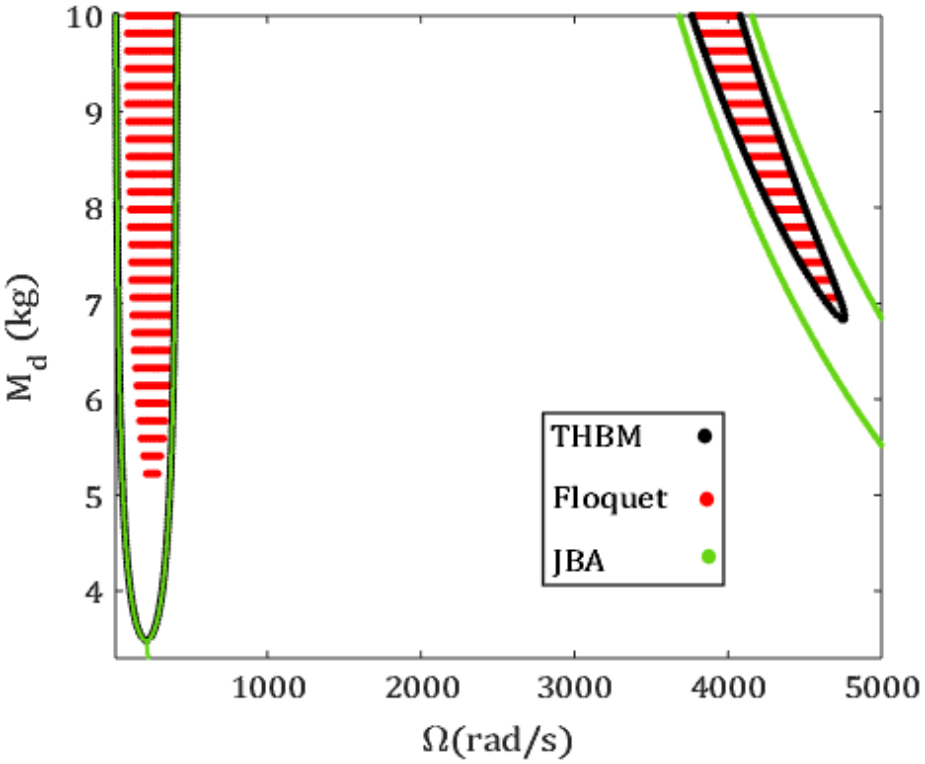

Figure 43: Stability plot of the rotor system obtained by the THBM, Floquet theory, and JBA for $C = 2500$ N.m/s

To provide an assessment of the applicability and efficiency of JBA in comparison to THBM and Floquet theory, all three approaches are performed for the 200 values of M_d and 200 values Ω_{vc} for: $1(\text{kg}) \leq \text{M}_\text{d} \leq 10(\text{kg})$ & $1(\text{rad/s}) \leq \Omega_{\text{vc}} \leq 2 \times 10^4(\text{rad/s})$. As shown in Table 7, the computational time of the JBA compared with the other approaches is extremely low. Considering the results from these three approaches, it could be claimed that by knowing the frequency contents, JBA is a powerful tool for stability analysis of a system under parametric excitation.

Table 7: Comparison of the computational time of the different stability analysis approaches to obtain the complete stability plot for $1(\mathrm{kg}) \le \mathrm{M_d} \le 10(\mathrm{kg})$ & $1\left(\frac{\mathrm{rad}}{\mathrm{s}}\right) \le \Omega \le 10^4\left(\frac{\mathrm{rad}}{\mathrm{s}}\right)$

Stability analysis approach	Number of points	Time of computation
Floquet	200 samples of $\mathrm{M_d}$ 200 samples of Ω	10800 (s)
THBM	200 samples of $\mathrm{M_d}$ Ω is an unknown to be computed	6540 (s)
JBA	200 samples of $\mathrm{M_d}$ 200 samples of Ω	3 (s)

3.5 Conclusion

In this chapter, the stability analysis of a Jeffcott rotor induced by the varying compliance of the supporting Rolling Element Bearing (REB) is taken into account. By linearizing the nonlinear contact forces generated due to the varying compliance, this phenomenon has been modeled by a set of time – varying stiffnesses which are sources of parametric excitation.

In this study, an improved procedure of HBM denoted by 'THBM' and a new procedure named 'JBA' to obtain the stability plot of the Jeffcott rotor system under parametric excitation are proposed. Here the stability plot, containing unstable regions, obtained from Floquet theory implementation is adopted as the reference. And, the accuracy and efficiency of THBM and JBA in computing the stability plots are examined by comparing them with the results from Floquet theory.

The following remarks are inferred for this study:

- The stability plot contains two unstable zones at low and high rotational speeds of the shaft.
- The domain of instabilities detected by implementing Hill's method is just valid at the second unstable zone.
- SHBM finds just the transition curves corresponding to the second unstable zone while it gives an insufficient prediction of the transition curves regarding the first unstable region.

- Using THBM, where the frequency components are chosen based on the frequency contents of the first unstable zone, acceptably determines the transition curves associated with both of the unstable regions.
- The Campbell diagram built by the eigenvalues of the Mass and Stiffness matrices without considering the time – varying parts, is not able to demonstrate the extra modes generated by the parametric excitation.
- Conducting the eigenvalue problem using mass and stiffness matrices extracted from the Jacobian matrix, where the time – varying stiffnesses are taken into account, results in a Campbell diagram illustrating the natural frequencies due to the parametric excitation.
- The spy plot of the Jacobian matrix shows that the absence of instabilities due to the parametric excitation in the frequency response plot is due to not considering any contribution of the frequency components related to the unstable regions within the force vector.
- Employing JBA, where some test harmonic forces possessing frequency components at the unstable zones are considered, the domain of instabilities in addition to the simple resonances are specified within the frequency response plot.
- The comparison of the stability plots produced by JBA, THBM, and Floquet theory implies that the JBA is a highly cost – efficient and accurate method to build the stability plot.

Chapter 4

Study of the JBA Applicability and Experimental Investigation of Instability due to Parametric Excitation

4.1 Introduction

In this chapter, the stability analysis of a continuous system under parametric excitation is taken into account.

The first part of this chapter focuses on further study of the JBA method, developed in the previous chapter, in obtaining the stability plot of the structure.

In the second part, an experimental study of instability due to parametric excitation is taken into consideration. The test case, adopted as a demonstrator, consists of a cantilever beam mounted on a spring with a time – varying stiffness.

4.2 Mathematical modeling

The schematic of a cantilever beam is depicted in Figure 44. In this figure, L represents the length of the beam with $b \times h$ rectangular cross – section. In this study, the beam has been modeled by seven Bernoulli – Euler beam elements with translational and rotational nodal DOFs. At the distance L_m from the clamped support, the system is supported by a spring whose stiffness is time – dependent and denoted by:

$$k(t) = -K_0\left(1+\cos\eta t\right) \tag{4.1}$$

Eq. (4.1) is a parametric excitation where K_0 and η designate respectively the amplitude and the frequency. The correspondence between the Eq. (4.1) and the experimental set – up will be further justified in section 5.3. The governing equations of motion of a cantilever beam shown in Figure 44 are as follows:

$$[M]_{n\times n}\{\ddot{y}\}_{n\times 1}+[C]_{n\times n}\{\dot{y}\}_{n\times 1}+\left([K]_{n\times n}+k(t)H\right)\{y\}_{n\times 1}=0 \tag{4.2}$$

Here n denotes the number of DOFs of the system and the matrices $[M]$, $[K]$ and $[C]$ represent the mass, stiffness, and damping of the system respectively. The damping is mass – stiffness proportional and computed by $\alpha[M]+\beta[K]$. According to Figure 44, the spring is placed at node E, indicated by the red dot, and just constraints the translational displacement y_E. To specify this point in Eq. (4.2) a vector of Heaviside functions H is multiplied by $k(t)$. The vector has a unitary value $H=1$ at node E only, while it is $H=0$ at all other nodes.

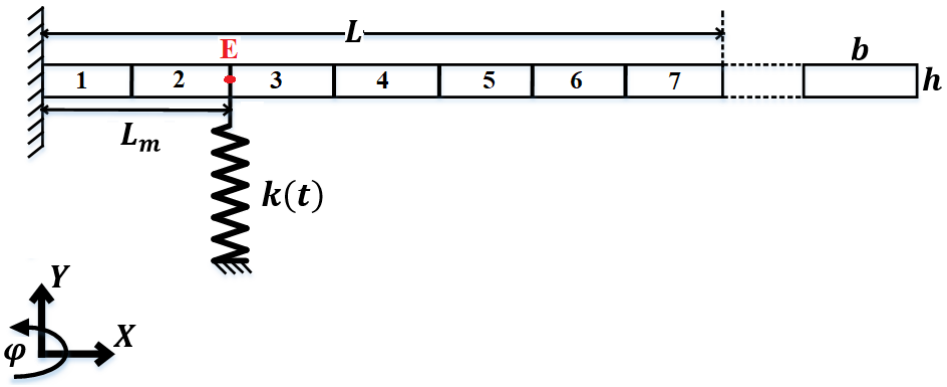

Figure 44: Schematic of a cantilever beam mounted on a time – varying spring

4.3 Stability analysis

In the previous chapters, the probability of instability (unbounded/unstable responses) occurrences at frequencies close to the parametric resonance frequencies, mentioned in Eq. (1.2), has been investigated. Here, due to the presence of time – dependent stiffness denoted by (4.1), there is a possibility of structure's instability emergence at specific parametric excitation frequencies η. Hence, obtaining the stability plot where the regions of the unstable responses are highlighted is of great importance. In this section, first, the stability plot obtained by Hill's method is given; then, in a separate subsection, a detailed procedure of JBA implementation to compute the stability diagram is presented. It must be noted

that for this study K_0 and η are taken as the control parameters and accordingly the stability plot is presented at the (η, K_0) plane. The values of the system's parameters are given in Table 8.

Table 8: System's parameters & Natural frequencies

h(m)	b(m)	L(m)	L_m(m)	E(Pa)	ρ(kg/m^3)	M_s(kg)
3×10^{-3}	30×10^{-3}	540×10^{-3}	155×10^{-3}	70×10^{9}	2700	10×10^{-3}

ω_{n1}	ω_{n2}
8.4 Hz (52.7 rad/s)	51.1 Hz (321 rad/s)

Eq. (4.2) is similar to a multi – Dofs Mathieu equation and to implement Hill's method, the coordinates of the system $\{y\}$ in Eq. (4.2) must be expressed according to Eq. (2.46) containing T and $2T$ periodic responses. Here, T is the period of the parametric excitation and is equal to $2\pi/\eta$. Solving the eigenvalue problem given by Eq. (2.49) and adopting the proper Floquet exponents based on the criteria given at the end of section 2.4, results in the stability plot shown in Figure 45.

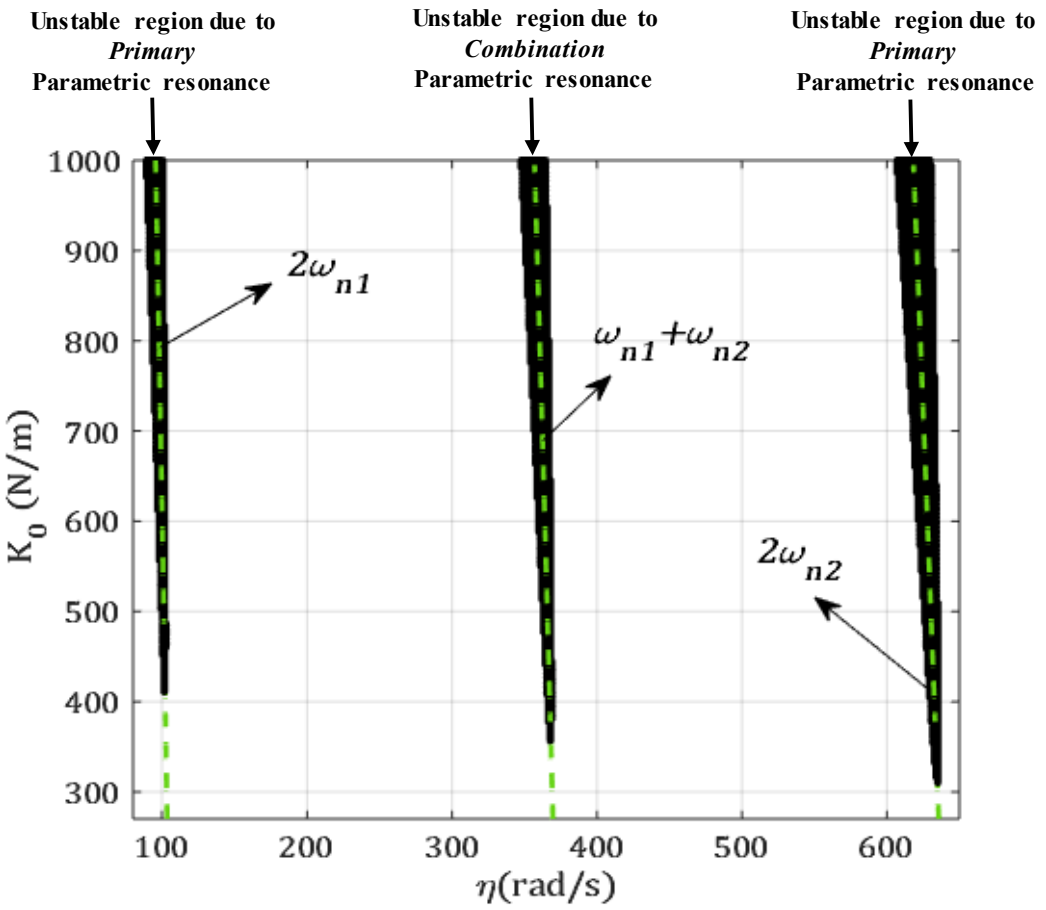

Figure 45: Stability plot of the cantilever beam using Hill's method

The stability plot in Figure 45 comprises three unstable regions highlighted by the black areas. To specify the type of each unstable zone, first, for all the values of K_0, the values of twice the first two natural frequencies ($2\omega_{n1}$ & $2\omega_{n2}$) and their summation ($\omega_{n1} + \omega_{n2}$) are computed. These values are depicted by the green dashed lines in Figure 45. As shown here, the green dashed lines corresponding to $2\omega_{n1}$ and $2\omega_{n2}$ respectively pass through the 1st and 3rd unstable regions which implies that these instabilities are trigged due to the Primary Parametric Resonances. Correspondingly in Figure 45, the unstable region in the middle where the line of $\omega_{n1} + \omega_{n2}$ passes, is appeared by the Combination Parametric Resonances. It must be noted that the results obtained by Hill's method were already justified by the one from Floquet theory (Please refer to APPENDIX F).

Although Hill's method has high accuracy and is computationally more efficient than Floquet theory, it still takes a considerable amount of time to provide

the stability plot for high Dof systems; For this reason, the JBA method is proposed as an alternative to Hill. In the following section, the implementation of JBA is explained and the efficiency and accuracy of this new method in comparison to Hill's method are further investigated.

4.3.1 Jacobian Based Approach (JBA)

As was discussed in chapter 3, unlike Hill's method and Floquet theory which detect the unstable zone, the JBA method computes the transition curves corresponding to an unstable zone. In addition, for specific values of the system's parameters, JBA implementation results in a frequency response plot where the borders of instability are specified.

To implement JBA, the lateral motion of each node y_i is expressed by the Fourier series:

$$y_i = \sum_{z=0,1,\dots}^{N_{h1}} \left(a_{iz} \sin\frac{z\eta t}{2} + b_{iz} \cos\frac{z\eta t}{2} \right) + \sum_{s=1,2,\dots}^{N_{h2}} \left(\left(c_{is} \sin(s\omega_1 t) + d_{is} \cos(s\omega_1 t) \right) + \left(e_{is} \sin(s\omega_2 t) + f_{is} \cos(s\omega_2 t) \right) \right), \tag{4.3}$$

where i denotes the nodes' number. In Eq. (4.3) the first set of Fourier series corresponds to T and $2T$ periodic responses (with frequencies $\frac{z\eta t}{2}$) and the second part (with unknown frequencies $s\omega_1$ and $s\omega_2$) associates with the responses at the combination parametric resonance zone.

In the same way, the external test force at the desired node (here the tip of the beam) is stated in terms of the same harmonic components adopted in Eq. (4.3):

$$f_{ex_i} = F_{TT} \sum_{z=0,1,3,\dots}^{N_{h1}} \left(\sin\frac{z\eta t}{2} + \cos\frac{z\eta t}{2} \right) + F_T \sum_{z=2,4,\dots}^{N_{h2}} \left(\sin\frac{z\eta t}{2} + \cos\frac{z\eta t}{2} \right) + F_C \sum_{s=1,2,\dots}^{N_{h3}} \left(\left(\sin s\omega_1 t + \cos s\omega_1 t \right) + \left(\sin s\omega_2 t + \cos s\omega_2 t \right) \right) \tag{4.4}$$

To compute the unknown frequencies ω_1 and ω_2, the same procedure given in section 2.7.4 is followed. To proceed, first, an optional value of K_0, here 800 N/m, is chosen. Then, a horizontal dashed line at $K_0 = 800$ N/m as shown in the upper plot of Figure 46 is depicted. The intersections denoted by points A and B, at the

border of the middle unstable zone corresponding to the combination resonance are then obtained. The FFTs of the responses computed at these two points are depicted in the lower part of Figure 46.

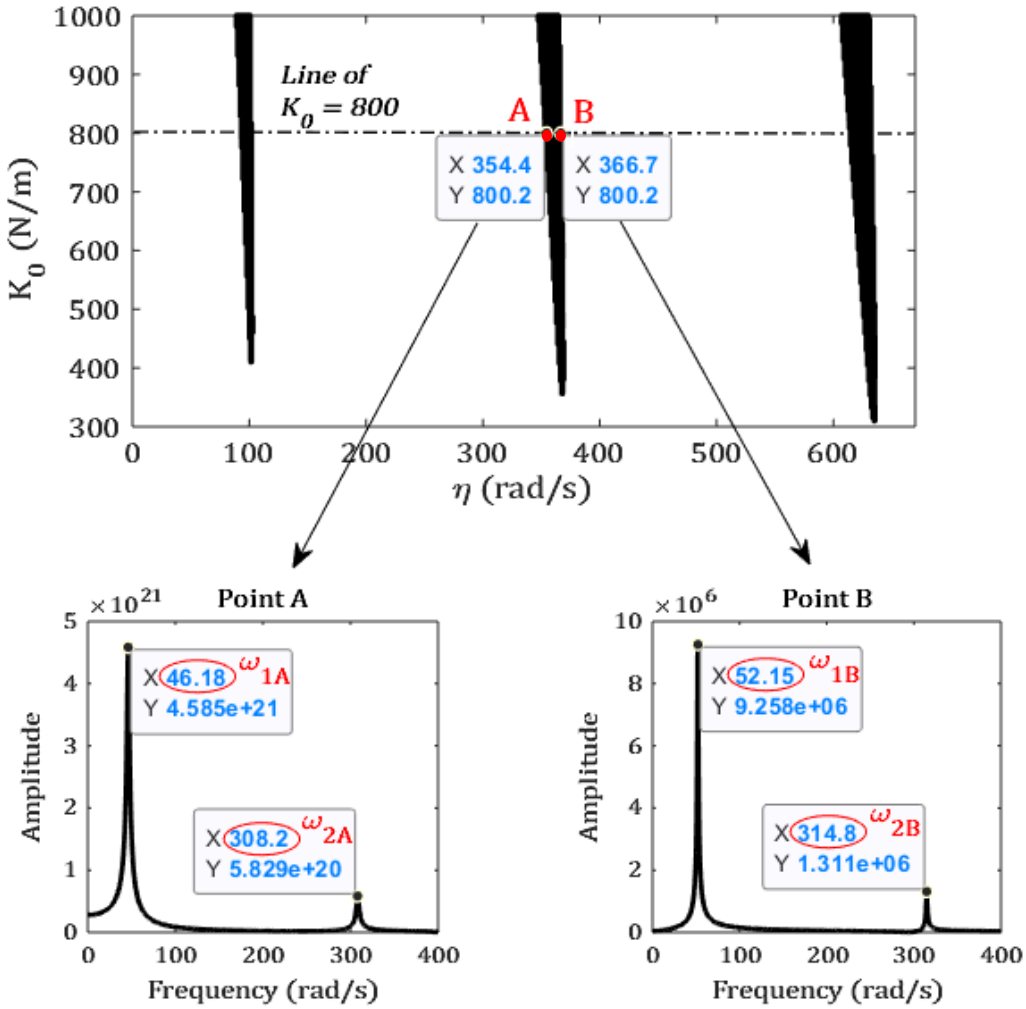

Figure 46: FFT of points A & B shown on the stability plot in the upper portion

By observing Figure 46, the following relationships between the frequencies components are deduced:

$$\left(\omega_{1A} + \omega_{1B}\right)/2 \cong \omega_{n1} \tag{4.5}$$

$$\left(\omega_{2A} + \omega_{2B}\right)/2 \cong \omega_{n2} \tag{4.6}$$

$$\omega_{2B} - \omega_{1B} \cong \omega_{2A} - \omega_{1A} \tag{4.7}$$

Subtracting Eq. (4.5) from Eq. (4.6) and using Eq. (4.7):

$$\omega_{2A} - \omega_{1A} \cong \omega_{n2} - \omega_{n1} \ , \tag{4.8}$$

and from Eq. (4.7) and Eq. (4.8):

$$\omega_{2B} - \omega_{1B} \cong \omega_{n2} - \omega_{n1} \tag{4.9}$$

The following relations are valid at the unstable zone resulting from the parametric combination resonance:

$$\omega_{1A} + \omega_{2A} = \eta_A \tag{4.10}$$

$$\omega_{1B} + \omega_{2B} = \eta_B \tag{4.11}$$

Subtracting Eq. (4.10) from Eq. (4.8) and, Eq. (4.11) from Eq. (4.9) would result in the subsequent expressions of ω_{1A}, ω_{1B}, ω_{2A} and ω_{2B}:

$$\omega_{1A} \cong \left(\eta_A + \omega_{n1} - \omega_{n2}\right)/2 \ , \ \omega_{2A} \cong \eta_A - \omega_{1A} \tag{4.12}$$

$$\omega_{1B} \cong \left(\eta_B + \omega_{n1} - \omega_{n2}\right)/2 \ , \ \omega_{2B} \cong \eta_B - \omega_{1B} \tag{4.13}$$

Considering Eq. (4.12) and Eq. (4.13), the general following expressions for the frequencies ω_1 and ω_2 are proposed:

$$\omega_1 = \frac{\left|\left(\eta + \omega_{n1} - \omega_{n2}\right)\right|}{2} \ , \ \omega_2 = \eta - \omega_1 \tag{4.14}$$

Substituting Eq. (4.3) and Eq. (4.4) in Eq. (4.2) and using Eq.(4.14) and following the HBM process, yields the subsequent residual equation:

$$\{R\} = \{F_{ex}\} - [J]\{U\} \ , \tag{4.15}$$

where $\{F_{ex}\}$ and $\{U\}$ are respectively the vectors of external forces and amplitudes of the Fourier expressions in Eq. (4.3) and $[J]$ is the Jacobian matrix. Considering $N_{h1} = 4$ and $N_{h2} = 1$ in Eq. (4.3) and Eq. (4.4), the frequency components adopted in Eq. (4.15) are as follows:

$$\frac{\eta}{2}, \eta, \frac{3\eta}{2}, 2\eta, \omega_1, \omega_2 \tag{4.16}$$

By minimizing the residual $\{R\}$ in Eq. (4.15) a frequency response shown in Figure 47 containing peaks corresponding to the borders of the instabilities would be obtained. In this figure, the blue curve is the response of the system to the external test forces with the frequencies associated with the unstable regions due to primary parametric resonances i.e. frequencies $z\eta t/2$ in Eq. (4.4); conversely, the purple curve corresponds to the system's response to the external test forces having the frequency components related to unstable zones as a result of the parametric combination resonances i.e. frequencies $s\omega_1$ and $s\omega_2$ in Eq. (4.4).

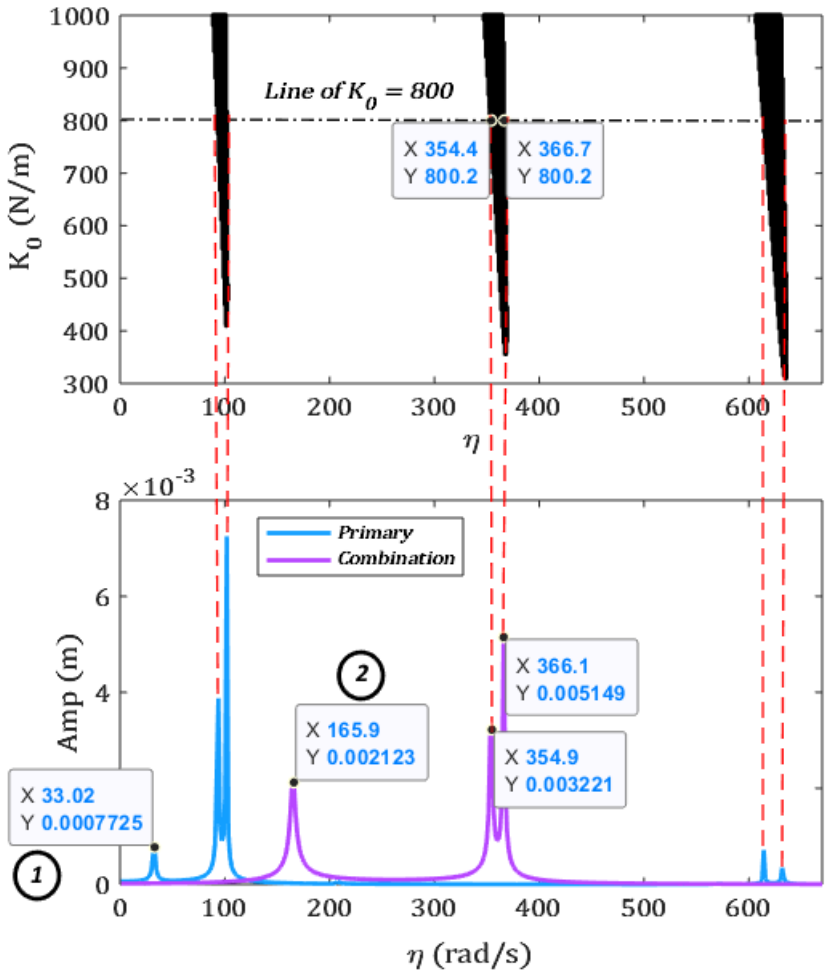

Figure 47: Investigation of the instability borders using JBA

According to the stability plot, shown in the upper portion of Figure 47, there are two regions of instability due to the primary parametric resonances; accordingly, the blue curve, resulted from the frequency contents present in this region, contains two sets of dual peaks which specifies accurately the borders of these regions. This is shown in Figure 47 by dashed red lines connecting each pair of dual peaks to the stability plot (obtained using Hill's method) at $K_0 = 800$ N/m and the corresponding values of η. Correspondingly, in Figure 47, the purple curve is obtained by considering the frequency components associated with the unstable regions due to the combination parametric resonances. This curve contains one set of dual peaks which accurately specifies the limit of this unstable region.

In Figure 47, it is noticeable that the results from the JBA implementation contain two extra peaks, denoted by ① & ②, which have nothing to do with instability detection. The emergence of such peaks is a by-product of the method itself. The reason is that, when the external test force vector in Eq. (4.4) inserted into the equations of motion is swept for a range of η, it may happen that the exciting frequency coincides with one of the natural frequencies causing a resonance. For instance, the first peak of the blue curve at $\eta = 33$ rad/s, marked by ①, makes the system resonate. This is because at $\eta = 33$ rad/s one of the frequencies in Eq. (4.4) , $3\eta/2$, will be equal to $\omega_{n_1} = 52.7$ rad/s. Accordingly, for the peak ② of the purple curve, when $\eta = 165.9$ rad/s and considering Eq. (4.14), it holds $\omega_1 = \omega_{n_1}$ which also results in the resonance of the system. It should be noted that these extra contributions can be easily filtered out a priori and they are shown here only to demonstrate a full implementation of the JBA method.

As mentioned in the previous chapter, to build the stability plot using JBA, the following procedure must be followed:

a) Perform the JBA for different values of K_0 for an interval of η
b) For each K_0, build a plot like in Figure 47
c) Collect the frequency values corresponding to the peaks demonstrating the domains of instabilities
d) Plot the collected points from the previous step

Doing so, the stability plot obtained by JBA is given in Figure 48. In this figure, it can be observed that the transition curves computed by JBA accurately locate all the unstable regions obtained through Hill's method. Here, the blue transition curves determine the border of the instabilities due to the primary parametric resonances while the purple one characterizes the unstable zone induced by

combination parametric resonances. In addition, the first and second lines of simple resonances shown in Figure 48 (see the labels at the bottom left), are the collection of the peaks ① and ② shown in Figure 47 for different values of K_0.

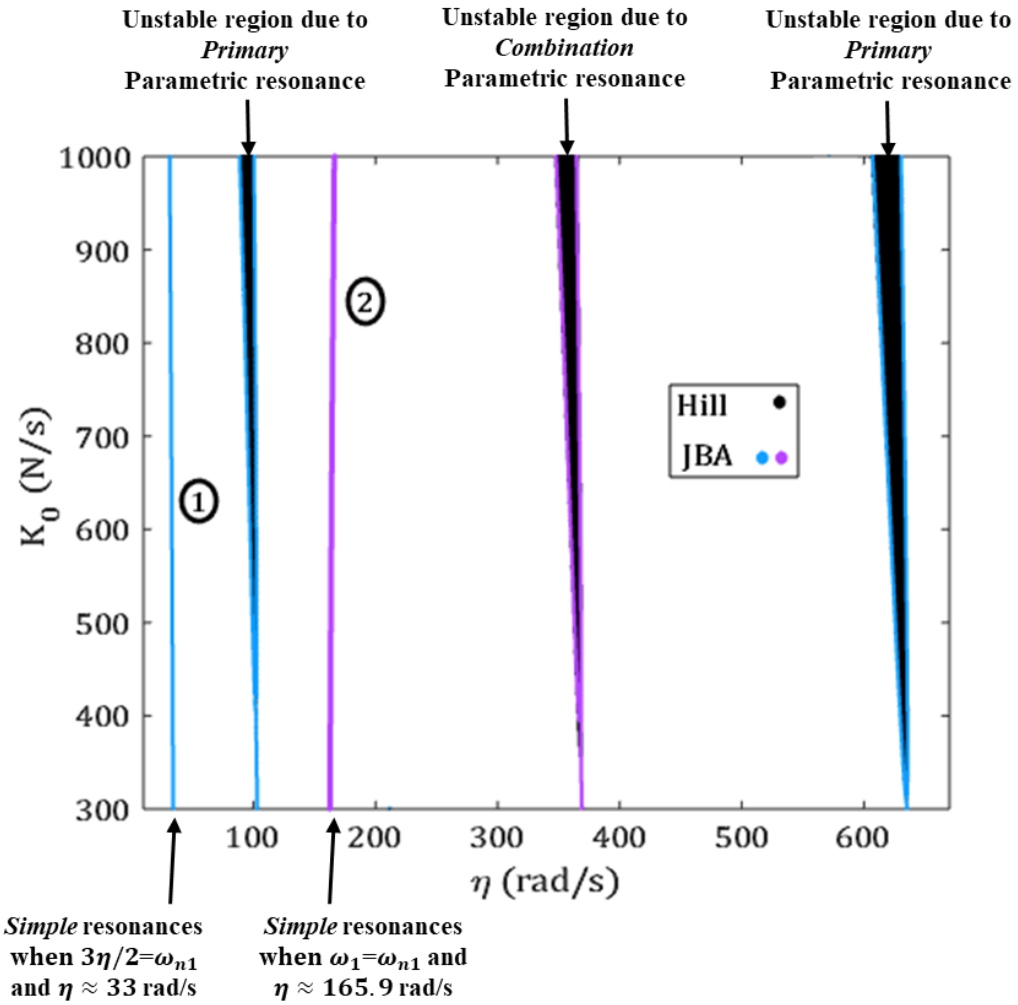

Figure 48: Comparison of the stability plots obtained JBA & Hill's method

To make a comparison, in terms of computational time, between JBA and Hill's method, a portion of the stability plot at 600 N/m $\leq K_0 \leq$ 800 N/m and 0 rad/s $\leq \eta \leq$ 700 rad/s considering 500 values for each parameter, is recomputed where the duration of the computation is presented in Table 9. It must be noted that the reason for choosing this portion of the stability plot is that this part contains just the unstable regions which could be computationally time – consuming to obtain. In this way, the efficiency of the two methods can be examined more precisely.

According to Table 9, JBA is almost 45 times faster than Hill in obtaining the stability plot.

Table 9**:** The computational time for obtaining the complete stability plot via Hill's method and JBA for $600\left(\frac{\mathrm{N}}{\mathrm{m}}\right) \le K_0 \le 800\left(\frac{\mathrm{N}}{\mathrm{m}}\right)$ & $0\left(\frac{\mathrm{rad}}{\mathrm{s}}\right) \le \eta \le 700\left(\frac{\mathrm{rad}}{\mathrm{s}}\right)$

Stability analysis approaches	**Number of samples**	**Time of computation**
Hill's method	500 samples of K_0 500 samples of η	5807 (s)
JBA	500 samples of K_0 500 samples of η	127 (s)

Based on the studies on JBA in the current and previous chapters, a guideline for the implementation of this method, according to the number of Dof, is provided in Table 10.

Table 10**:** Summary of the frequency contents of the unstable responses due to parametric resonance for systems of increasing complexity (the output of this table is used for the JBA implementation)

Dof of the System under parametric excitation with frequency η	*Primary Parametric Resonance (PPR)*	*Combination Parametric Resonance (CPR)*	*Dominant Frequency contents*	
1-Dof system with single eigenfrequency	✓		**PPR:** $2T$ periodic responses ($T = \frac{2\pi}{\eta}$): $\frac{z\eta}{2}$, $z = 1 \dots, n_h$	**CPR:** Null
2-Dof system with identical eigenfrequencies: ($\omega_{n1} = \omega_{n2} = \omega_n$)		✓	ω_n , $\omega_n \pm \eta$	
N-Dof system ($N \geq 2$) considering the first two modes with different eigenfrequencies	✓	✓	**PPR:** $\frac{z\eta}{2}$, $z = 1 \dots, n_h$	**CPR:** $\omega_1 = \frac{\lvert\eta + \omega_{n1} - \omega_{n2}\rvert}{2}$ $\omega_2 = \eta - \omega_1$

4.4 Experimental rig set-up

In order to experimentally evidence the presence of instabilities due to the parametric excitation, a test rig was designed as a demonstrator. As depicted in Figure 49, to generate the parametric excitation, an electromagnet unit and a permanent magnet, attached to the beam, are utilized. The force generated by the electromagnet simulates a spring with time – varying stiffness which will be justified and formulated in the next section. In Figure 49, the gap between the electromagnet and the permanent magnet is designated by L_0; it will be shown that the gap is the key parameter in calculating the magnetic force and consequently the time – varying stiffness. The magnet apparatus (electromagnet and permanent magnet) is placed at a distance L_m from the clamped support which is the same as the mathematical model shown in Figure 44. The electromagnet is activated by an amplified AC current generated by a NI ConpactRIO system. To measure the vibrations, a measuring point denoted by the green dot in Figure 49, close to the tip of the beam, is selected. The response is measured by a Polytec Laser vibrometer.

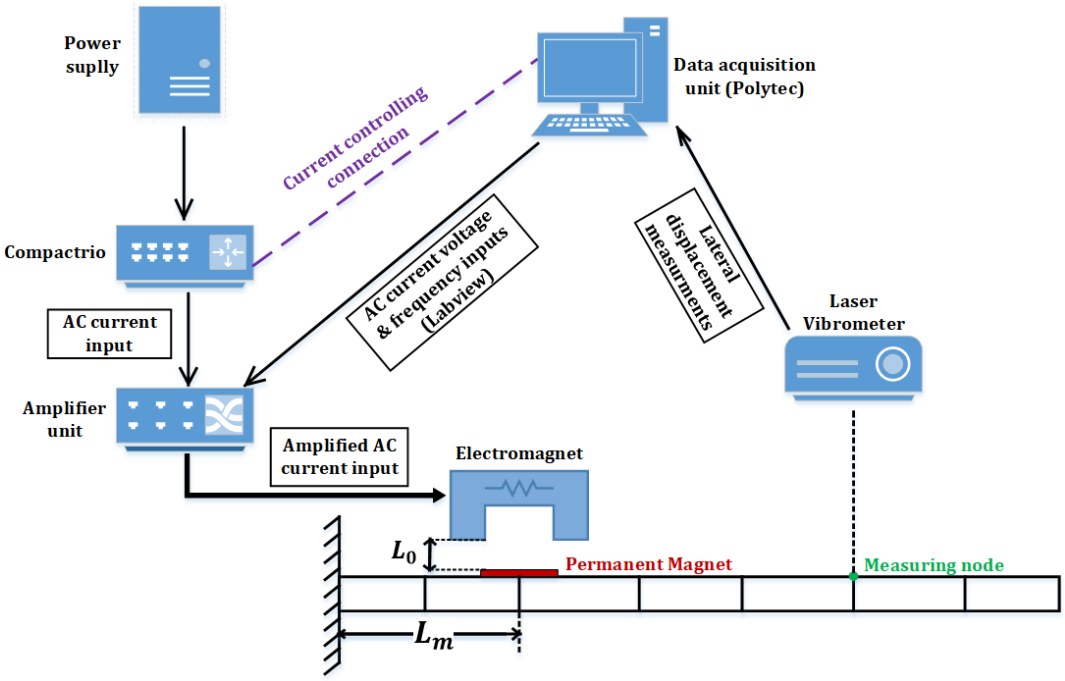

Figure 49: Schema of the experimental setup

The real view of the rig is presented in Figure 50. According to this figure, an electromagnet made of two coils wrapped around a U -shaped core of ferromagnetic packed plates is used. To induce the beam by a magnetic field (and as a consequence an excitation force), two prismatic extensions are attached to the end sides of the

U-shape core. Since the beam is made of aluminum, a thin steel plate as the permanent magnet is attached to the beam. As indicated in Figure 50 and Figure 51, the electromagnet is mounted on a force transducer which directly measures the magnetic force denoted by F_m. This is highly advantageous since the computation of the magnetic force is possible without knowing the electrical parameters. It must be noted that to compute the real magnetic force generated by the electromagnet, F_0, the measured force F_m must be multiplied by a calibration factor at the corresponding frequency. The calibration plot will be explained and shown in the next section.

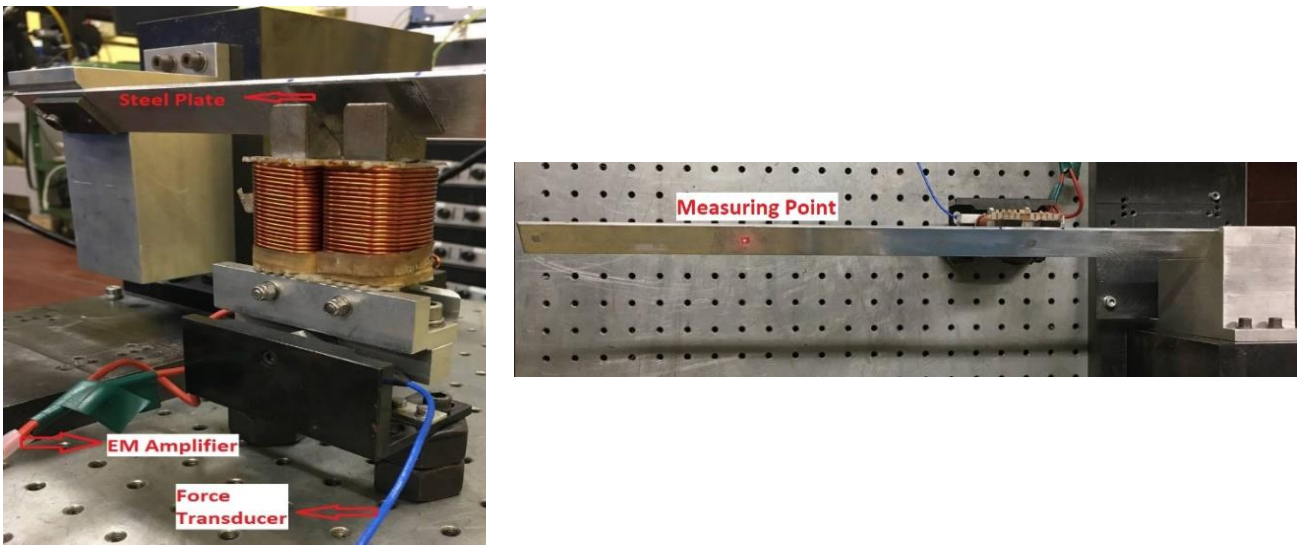

Figure 50: Test rig

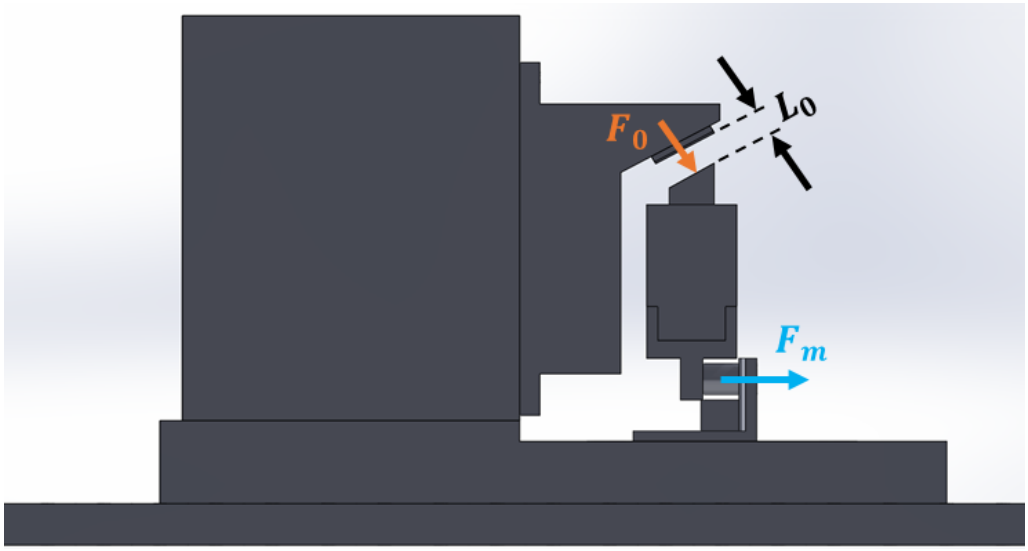

Figure 51: Actual magnetic force generated by the magnet (F_0) and the force measured by the transducer (F_m)

4.4.1 Time – varying stiffness generated by the electromagnet

According to (Firrone, Berruti and Gola, 2013), the magnetic force is expressed by the following formula:

$$f(t) = \frac{A}{(L_0 - y_m)^2}(1 - \cos \eta t) \tag{4.17}$$

The procedure to obtain Eq. (4.17) is given in APPENDIX G. Here, y_m represents the displacement of the measuring point, illustrated in Figure 51, recorded by the laser vibrometer, η is the frequency of the electromagnet and A is defined as (Berruti, Firrone and Gola, 2011):

$$A = \frac{N^2 \mu_{air} S' I^2}{2} \tag{4.18}$$

Here, the parameters N, μ_{air}, S' and I represent respectively the number of turns of the coils, the air permeability, the area of each coil facing the permanent magnet, and the amplitude of the AC current.

At frequencies far from the resonance, the displacement of the beam is almost negligible with respect to the gap L_0. In other words, the beam has infinitesimal

oscillation around its equilibrium $y_m = 0$. To this end, the magnetic force in Eq. (4.17) could be expanded, using the Taylor series, around the equilibrium (Zaghari, Rustighi, and Ghandchi Tehrani, 2018). Collecting just the first – order terms of the expansion, the force would in Eq. (4.17) becomes:

$$\begin{aligned} f(t) &= \frac{A}{L_0^2}(1-\cos\eta t) + \frac{2A}{L_0^3}(1-\cos\eta t)\, y_m \\ &= F_0(1-\cos\eta t) + K_0(1-\cos\eta t)\, y_m \end{aligned} \tag{4.19}$$

Eq. (4.19) comprises two terms: a periodic force denoted by $F_0(1-\cos\eta t)$ and a force due to a time – varying stiffness denoted by $K_0(1-\cos\eta)y_m$. In Eq. (4.19), the constant A is:

$$A = F_0 L_0^2 \ , \tag{4.20}$$

and would be obtained by knowing F_0which is connected to the measured force F_m.

As was mentioned earlier and is also observable from Eq. (4.20), the constant A could be obtained without the need of Eq. (4.18). Eq. (4.20) could be then used in Eq. (4.19) to compute $K_0 = 2A/L_0^3$ and as a result $f(t)$. As pointed out before, the gap L_0 is the key parameter and its different values result in different amplitudes of both the external force and the time – varying stiffness.

In the following section, the presence of instability in the rig will be proven experimentally and the results would be verified by the numerical model.

4.5 Stability analysis of the test rig (Experimental – Numerical verification)

The aim of this experimental study is to prove the presence of instability at the combination parametric resonance frequency. For this purpose, the parametric frequency is tuned close to the summation of the first two natural frequencies i.e. $\eta \approx \omega_{n1} + \omega_{n2}$. The first two natural frequencies of the numerical and the experimental models are given in Table 11. According to this table, there is a small difference between the eigenfrequencies of the numerical and experimental models; therefore, the numerical model is reasonably accurate.

Table 11: First two Natural Frequencies of the cantilever beam

Numerical Model	Test Rig
$\omega_{n1} = 8.4$ Hz (52.7 rad/s)	$\omega_{n1} = 8.36$ Hz (52.5 rad/s)
$\omega_{n2} = 51.1$ Hz (321 rad/s)	$\omega_{n2} = 50.47$ Hz (317.1 rad/s)

It must be noted that the frequency fed to the electromagnet from the control system is an electrical frequency which is half of the mechanical frequency.

The electromagnet is fed by an alternate current with an Electrical frequency η_e. This corresponds to an alternate excitation force on the beam given by Eq.(4.17) whose frequency η is two times the electrical frequency η_e, as demonstrated in (Firrone, Berruti, and Gola, 2013). Therefore:

$$\eta_e = \eta / 2 \tag{4.21}$$

For this study, the beam is excited close to the parametric combination resonance frequency $\approx \omega_{n1} + \omega_{n2} = 58.8$ (Hz), which corresponds to the electromagnet "electrical" frequency $\eta_e \approx \frac{\omega_{n1}+\omega_{n2}}{2} \approx 29.4$ (Hz).

According to Eq. (4.19), to compute the parameter A and correspondingly K_0, the amplitude of the periodic force F_0 at the frequency η must be determined. As referred earlier, F_0 depends on F_m(see Figure 51). To find the relationship between actual and measured forces i.e. F_0 and F_m respectively, a calibration process is performed in (Berruti, Firrone and Gola, 2011). In this study, the authors designed a calibration bench unit shown in Figure 52A that comprises an inertial mass made of aluminum (4) holding a force transducer (2) which is attached to another inertial mass (1). In this configuration, the force transducer carries a ferromagnetic anchor (3) which is placed parallel to the anchor of the electromagnet. By feeding the electromagnet by the alternating current with the electrical frequency η_e, the resulting harmonic magnetic force F_0 on the ferromagnetic anchor (3) has a frequency η which is twice η_e. By measuring the amplitude of the input force F_m and the amplitude of the force F_0 exerted on the anchor and computing their ratio for different electrical frequencies, the calibration diagram depicted in Figure 52B is obtained.

According to Figure 52B, the measuring point for the current test rig, shown by the orange dot, is out of the calibration curve. To be able to find the calibration

coefficient of the working frequency of this experiment i.e. $\eta_e \approx \frac{\omega_{n1}+\omega_{n2}}{2} \approx 29.4$ (Hz), an extrapolation between the two labeled frequencies at 50 and 55 Hz in Figure 52, which are the closest frequencies to the measured one, is performed. Then the measured force F_m at 29.4 (HZ) is divided by the corresponding calculated calibration coefficient to obtain the associated F_0.

A) B)

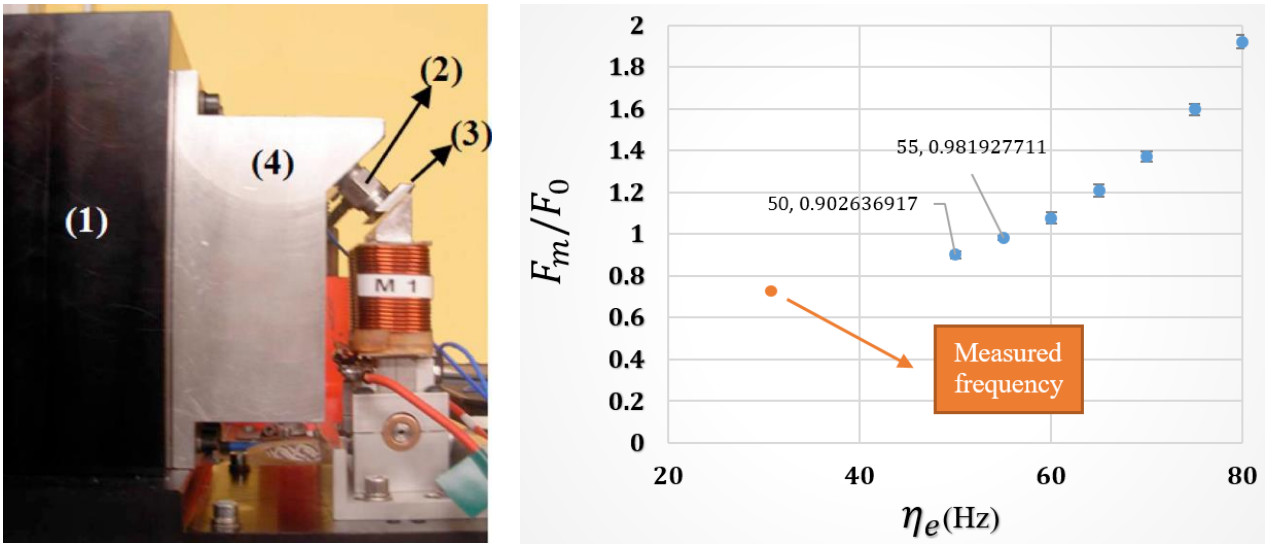

Figure 52: **A)** Calibration bench. **B)** Calibration curve of the electromagnet unit (Firrone, Berruti, and Gola, 2013)

By knowing how to compute the parameter F_0, it is now possible to compare the experimental and the numerical results. To this end, first, the behavior of the test rig for three values of the gap $L_0 = 7\text{ mm}, 8\text{ mm}, 9\text{ mm}$ is studied. The electrical frequency of the magnet η_e is kept close to the combination parametric resonance frequency i.e. $\eta_e \approx \frac{\omega_{n1}+\omega_{n2}}{2}$, where the high amplitude oscillations are observed. The displacement of the beam and the force are measured in the time domain. The FFTs of the measured signals are shown in Figure 53 by solid blue lines (force in the upper part and displacement in the lower part). The amplitude of the force at the excitation frequency η is the targeted force F_0. It is worth mentioning that the value of F_0 shown in the upper portion of Figure 53 is obtained from the measured force F_m by using the calibration coefficient, corresponding to the orange point, shown in Figure 52. According to Figure 53, for all the gap values, the FFT of the actual magnetic force exerted on the beam, F_0, contains a high peak at the frequency close to $\omega_{n1} + \omega_{n2}$ and two other small peaks corresponding to ω_{n1} and

ω_{n2}. The presence of the frequency component at $\omega_{n1}+\omega_{n2}$ is due to the frequency of the electromagnet exciting at this frequency; while the contributions of the first two natural frequencies, ω_{n1} and ω_{n2}, in the FFT of the force are due to the presence of these frequency contents in the response of the beam, shown in the lower portion of Figure 53. The FFT of the response contains two higher peaks at frequencies ω_{n1} and ω_{n2} which is typical of responses at the combination parametric resonances and a smaller peak at the forcing frequency. The presence of the two high peaks at ω_{n1} and ω_{n2} in the FFT of the response, typical of the combination parametric resonance, approves the generation of the parametric excitation by the electromagnetic force.

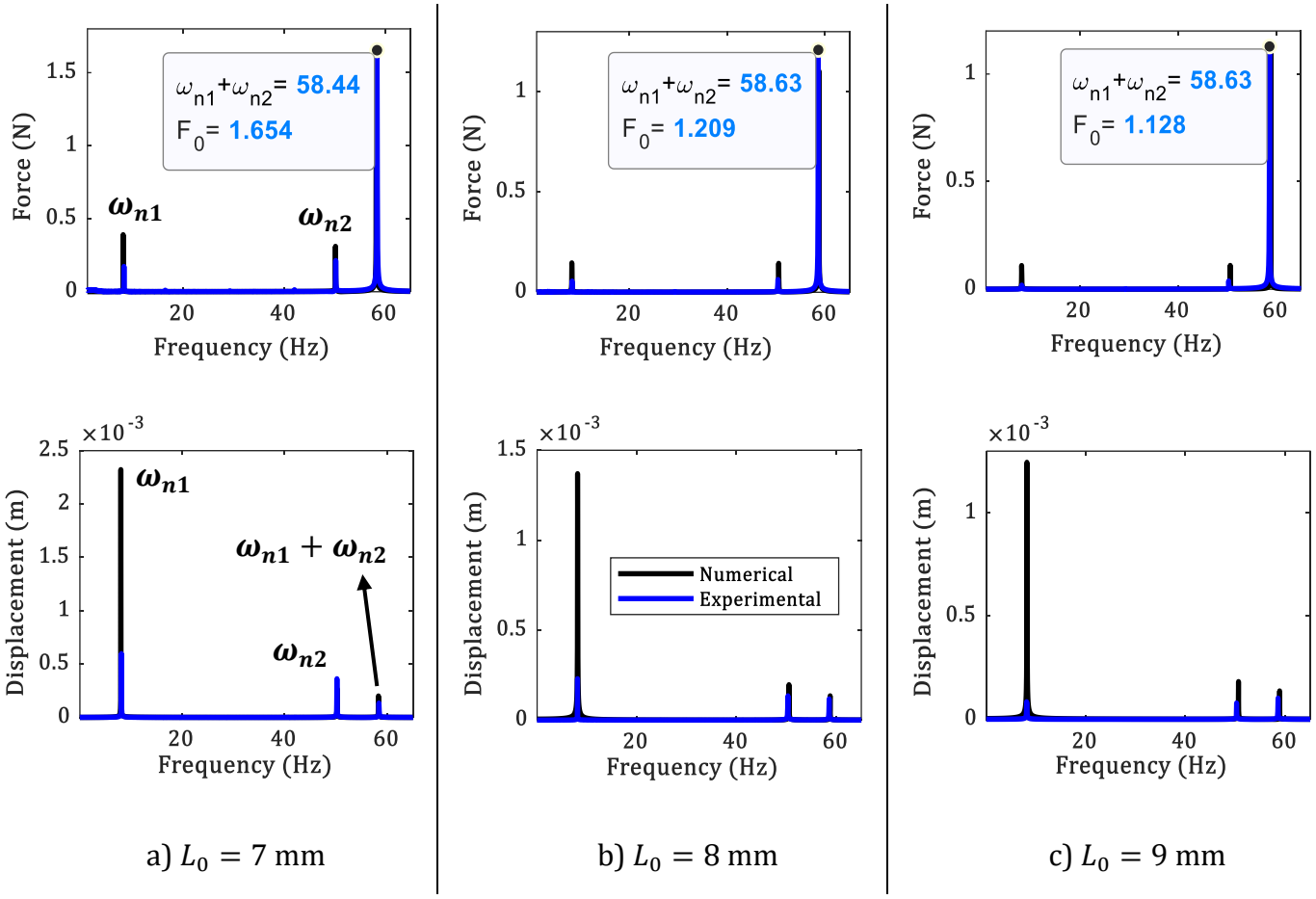

Figure 53: FFT of the force and displacement of the rig and mathematical model for different values of L_0

In order to compare the experimental results with numerical ones for each L_0 value and at $\eta \approx \omega_{n1}+\omega_{n2}$, the following quantities must be determined:

- the amplitude of the external force F_0

- the amplitude of the time – varying stiffness K_0
- the modal damping ratio ζ

The values of F_0 are read from the FFT of the magnetic force in the upper portion of Figure 53. These values which are denoted by the labels correspond to the peaks at the forcing frequency $\eta \approx \omega_{n1} + \omega_{n2}$. Inserting the values of F_0 and corresponding L_0 in Eq. (4.20) results in three different values of the coefficient A. In section 4.4.1, it has been shown that the strength of the time – varying stiffness (parametric excitation) generated by the electromagnet unit is a function of the gap value L_0 between the beam and the electromagnet's head. Here, it has also been proven mathematically that the amplitude of the time – varying stiffness K_0 is proportional to $1/L_0^3$ which implies that the small gaps generate big time – varying stiffness and vice versa (Check Eq. (4.19) and Eq. (4.20)). Considering this point, since the damping matrix is proportional and accordingly depends on the stiffness matrix of the beam which is a function of K_0, hence the damping matrix depends on the gap L_0. Therefore, the damping matrix must be updated for each value of L_0.

To determine the modal damping ratio, three tests/experiments for each of the following gap values: $L_0 = 7\ \text{mm}, 8\ \text{mm}, 9\ \text{mm}$, in all the cases instability has been observed experimentally, are carried out. Then, a series of numerical simulations for each gap value L_0 are performed. For each numerical attempt, a specific value is assigned to the modal damping ratio ζ and at the end, the highest value which ensures the numerical system to reach instability was chosen. By repeating this procedure for all nine experiments (three for each L_0), the selected values of ζ are collected and presented in Figure 54. To be able to predict the modal damping ratios for different gaps in $7\text{mm} \leq L_0 \leq 9\ \text{mm}$, two curves (Polynomial & Power) which best approximate the values of ζ as function of L_0 are fitted. For this study, the Polynomial fitted curve is chosen as the representative formula of ζ. Since instability is not observed experimentally for $L_0 > 9\ \text{mm}$, the modal damping is kept fixed and equal to the value of ζ at $L_0 = 9\ \text{mm}$.

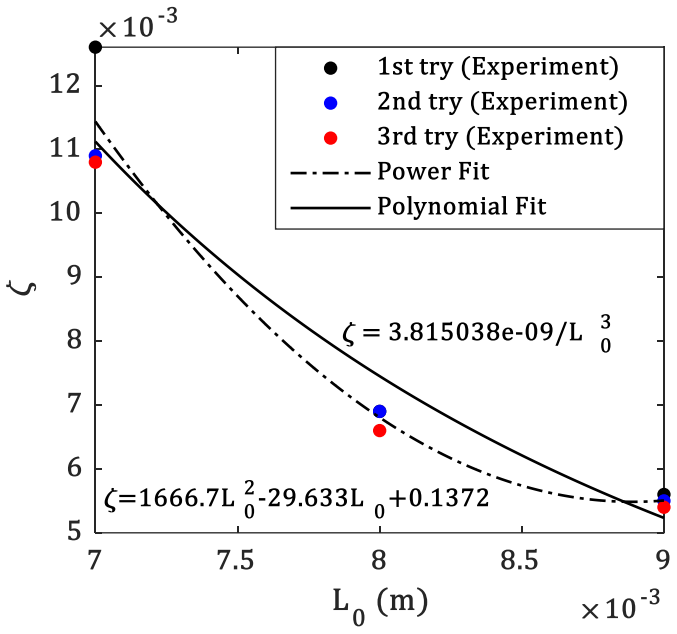

Figure 54: Modal damping ratio of the test rig

Then, by performing the Numerical analysis, the FFTs of the magnetic force i.e. $F_0(1-\cos\eta t)$ presented in Eq. (4.19) and the response of the same node as the test rig are plotted by the black solid lines in Figure 53. According to these results, a good agreement between the numerical and experimental results could be observed.

The only difference here is that the mathematical model oscillates unboundedly at the combination parametric frequency through time while the experimental rig reaches a steady state with high amplitude. This could be due to additional damping at the clamped support as a result of friction of the bolts as depicted in Figure 50. This point is better clarified in Figure 55 where the time signals of the measuring point, obtained Numerically and Experimentally for $L_0 = 8$ mm, are demonstrated. According to this figure, the time response in the mathematical model grows exponentially through time while in the experimental model the oscillations increase initially and then enter a steady – state. This shows that there is(are) extra damping(s) in the experimental model that prevents unbounded growth of the vibrations via time.

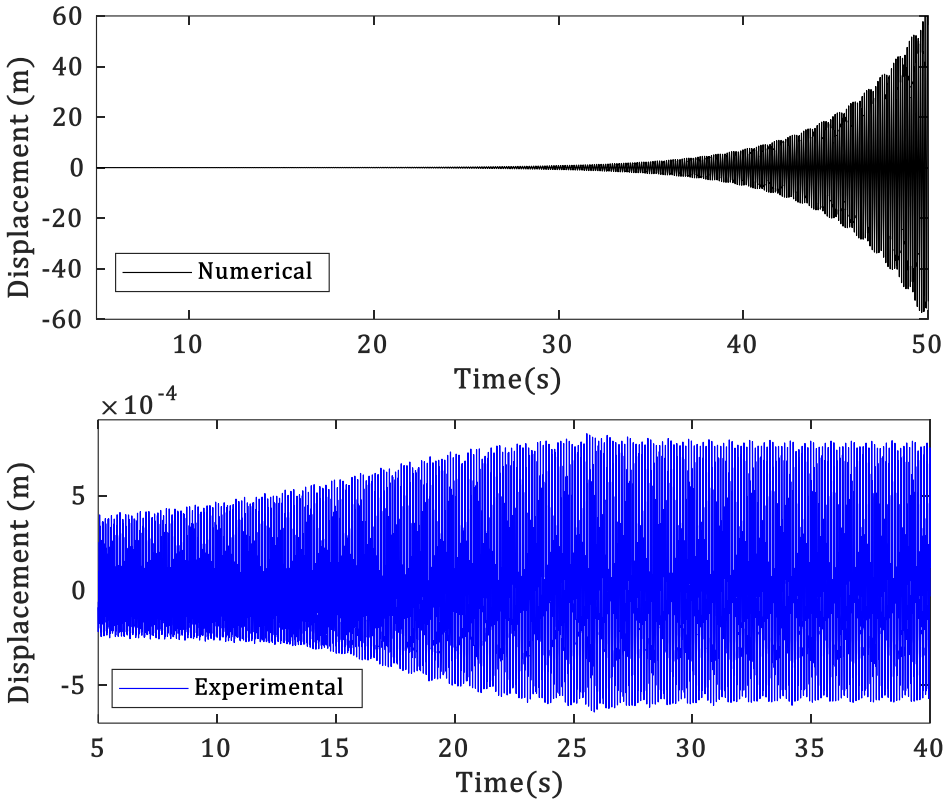

Figure 55: Numerical & Experimental time response of the measuring point for $L_0 = 8$ mm

It must be pointed out that as L_0 increases the effect of the parametric excitation becomes less and this is due to the dependency of K_0 on the gap as shown in Figure 56. Furthermore, considering the FFT of the responses in the lower portion of Figure 53, it is observable that the amplitude of the response at frequencies ω_{n1} and ω_{n2} decreases as the electromagnet is put farther from the beam.

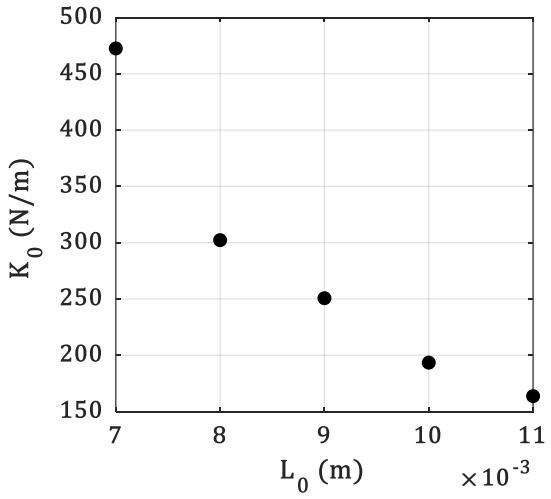

Figure 56: Amplitude of the time – varying stiffness K_0 as a function of the gap L_0

A numerical stability plot with the modified damping ratio obtained from Figure 54 has been performed and is shown in Figure 57. It must be noted again that the formula of the ζ is valid for K_0s corresponding to the gap range of $7\ \text{mm} \leq L_0 \leq 9\ \text{mm}$ while for K_0 correspoding to $L_0 > 9\ \text{mm}$ the constant value of ζ at $L_0 = 9\ \text{mm}$ is adopted. According to Figure 57, the experimental results for K_0 related to $L_0 = 7\ \text{mm}, 8\ \text{mm}, 9\ \text{mm}$, presented by red circles, are at the unstable region. Howevre, as L_0 goes beyond 9 mm the system becomes stable which is also confirmed experimentally. Here, the stable responses at K_0 correspoding to $L_0 = 10\ \text{mm}$ and $11\ \text{mm}$ are denoted by greeen squares which are outside the unstable zone.

A feature of the adopted electromagnet unit is that the FFT of the magnetic force signal contains a frequency component at half of the inserted frequency. Since the instabilities caused by the primary parametric resonances occur when the exciting frequency is almost equal to twice the natural frequency (see Figure 45), the existence of the aforementioned half frequency component results in the system's simple resonance rather than parametric resonance. Therefore, detection of the unstable zones due to the primary parametric resonances are excluded from the current experimental work.

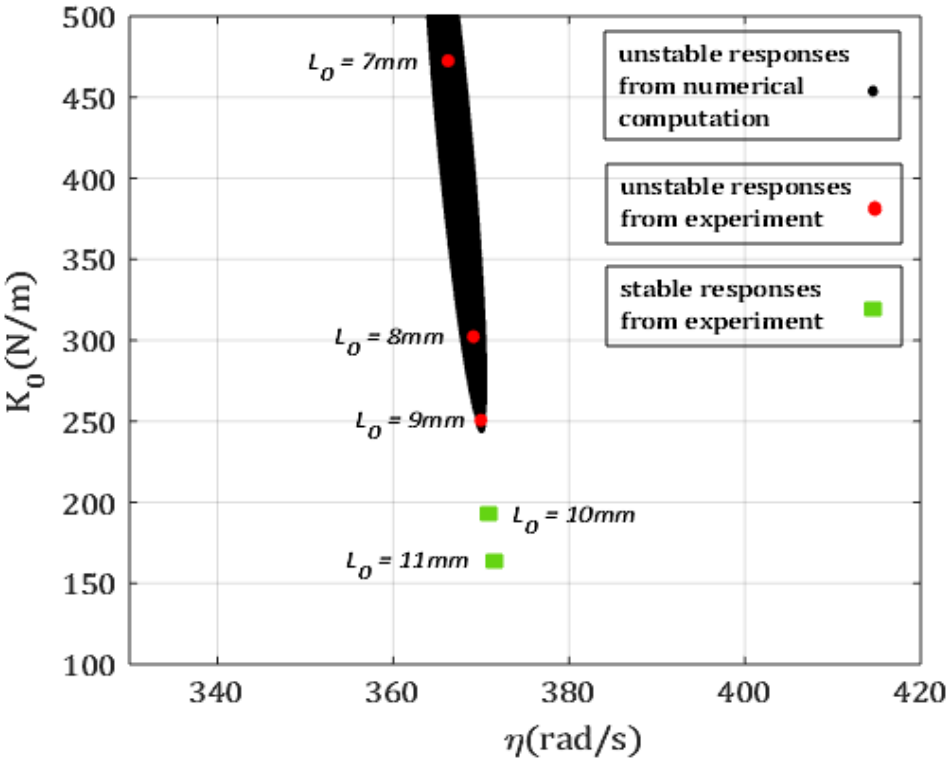

Figure 57: Stability plot corresponding to the test rig at the combination parametric resonance frequency

4.6 Conclusion

In this chapter a test case, consisting of a cantilever beam mounted on a spring with a time – varying stiffness is adopted as a demonstrator. In the first part of this chapter, the developed method JBA is applied to this demonstrator. The performance of the JBA has been examined and compared to the results from Hill's method. In the second part of the chapter, an experimental study of instability induced by parametric excitation on the same demonstrator has been carried out.

- The methods for the detection of unstable responses, coming from the literature (i.e. Hill's method) and proposed by the authors (Jacobian Based Approach), successfully identify the unstable regions of the system.
- It has been observed that by knowing the frequency contents of the responses at the unstable regions, JBA can obtain the full stability plot.
- By comparing the stability plots and computational time obtained by JBA and Hill's methods, the accuracy and efficiency of the JBA have been guaranteed.

- Utilizing the electromagnet in the test rig enables to trigger the instability at parametric combination resonance frequency which is typical of parametric excitation.
- The experimental results based on the direct measurement of the magnetic force confirm the results from the numerical simulation in terms of the frequency content of the response and stability characteristics.
- The amplitude of the unstable response in the numerical simulation is greater than the experimental one. This may be caused by disregarding additional sources of damping in the numerical model, e.g. friction at the bolts, which may limit the amplitude of the response.
- The peculiar characteristics of the combination resonance unstable response, i.e. large amplitude and multiple frequencies which are, in turn, different from the exciting frequency, make the experimental set up a good candidate for different applications, e.g. energy harvesting, multi-modal investigations, etc.

Chapter 5

Conclusion & Future Research Activities

5.1 An overview of the thesis

Parametrically excited systems are prone to unstable responses or high amplitude oscillations. The peculiarity of such instabilities is their occurrence at the so – called "Parametric Resonance Frequencies" which are different from the frequencies causing the simple resonances. Therefore, the stability analysis of structures under parametric excitation to detect the regions of instability is of high importance. The presence of instability is generally shown by the 'Stability Plot' where the domains of unstable responses are highlighted as a function of some system parameters.

The possibility of instability occurrence due to parametric excitation was examined in the thesis starting from the theoretical basis, going through the development of new methods to track the presence of instability, and ending with the search for experimental evidence of the presence of instability.

The 2nd chapter of the thesis is dedicated to the detailed explanations of the state-of-the-art stability analysis approaches i.e. Floquet theory, Hill's method, Harmonic Balance Method (HBM), Multiple Scales Method (MSM), and newly proposed method i.e. Jacobian Based Approach (JBA). In this chapter, a model of Mass – Spring – Damper is adopted as a simple, academic but applicable example to demonstrate a detailed implementation procedure of each of the aforementioned stability analysis approaches. In this chapter, it has been demonstrated that the stability plot of a 1-Dof parametrically excited system contains just instabilities due to the Simple and Primary Parametric Resonances. However, in case of a 2-Dof parametrically excited system, the instabilities as a result of Combination Parametric Resonance as well as Simple and Primary Parametric Resonances are present in the stability plot. In this chapter, the performance of the recently

developed method, Jacobian Based Approach, in terms of accuracy and computational time efficiency has been addressed.

In chapter 3, an improved HBM implementation called “Trained HBM (THBM)” is proposed and the applicability of the newly developed method, Jacobian Based Approach (JBA) is investigated. For this study, a Jeffcott rotor model supported by rolling bearing elements (REB), whose effect is modeled by time – varying stiffnesses (source of parametric excitation), is adopted as a demonstrator. In the first part of this study, it has been observed that not all the state-of-the-art methods i.e. simple implementation of HBM (SHBM) and Hill’s method, can successfully identify all unstable regions due to parametric excitation. It is demonstrated that, by proposing and applying THBM and comparing the results to the ones from Floquet theory, the stability plot containing all the unstable regions can be obtained. However, THBM had the drawback of demanding too much computational time, which is unacceptable specifically for systems with more than two degrees of freedom. Then, the implementation of the new stability analysis technique i.e. JBA, as a simpler and faster method was then proposed. The performance of this method is examined by obtaining the stability plot and recording the time of the computation. In this study, the accuracy of the results from JBA has been promised and it has been shown JBA to be 3600 times faster than the Floquet theory and 2180 times faster than THBM which proves its efficiency.

Further evaluation of JBA for the stability analysis of a system under parametric excitation as well as the experimental study of the instability induced by the parametric excitation are fulfilled in chapter 4. In this chapter, a cantilever beam model mounted on a spring with time – varying stiffness is employed as a demonstrator. In the first part of this chapter, the applicability of JBA in obtaining the stability plot is investigated. Here, the resultant stability plot from the JBA implementation and the one acquired via Hill’s method, already validated by the results from the Floquet theory, are compared. It has been shown that JBA is computationally efficient and precisely detects all the unstable regions caused by the Primary and Combination parametric resonances. The experimental investigation of the instability due to the parametric excitation is performed in the second part of chapter 4. A test rig, comprising a cantilever beam and an electromagnet unit, is designed and adopted as a test case. Here, it is proven that the electromagnet force generates a spring – like effect with varying stiffness. A diverging response, interpreted as instability, is obtained by setting the electrical frequency of the magnet equal to the combination parametric resonance frequency.

A good correlation, in terms of the frequency contents, between the experimental and predicted numerical results is also achieved.

5.2 Concluding remarks

The major contributions of this thesis are listed below:

- A detailed analysis of the state-of-the-art approaches, i.e. Floquet theory, Hill's method, Multiple Scales method, and Harmonic Balance method, to detect the unstable zones due to the parametric.
- A refinement of the HBM named here Trained HBM (THBM) to obtain the complete stability plot, in particular for the case of a parametrically excited 2-Dof system having equal eigenfrequencies.
- The development of a new, accurate, and computationally efficient stability analysis method based on the forced response analysis named "Jacobian Based Approach (JBA)".
- Design of a simple test rig to demonstrate, in a laboratory condition, the presence of instability due to parametric excitation generated by means of an electromagnet. In particular, the experiment provides measurements of the response and direct measurement of magnetic force, from which the variable stiffness can be computed.
- Validation of the numerical results by the ones from the experiment, in case of unstable dynamic response induced by parametric excitation.

5.3 Recommendations for future works

The newly proposed stability analysis method, JBA, requires substantial studies. To verify the suitability and capability of JBA in obtaining the stability plots, it should be applied to more complex systems under parametric excitation. Some of the potential future research objectives are listed in the following:

- Implementation of JBA to study a parametrically excited rotor systems due to a cracked shaft.
- Employment of JBA for stability analysis of a gearbox system with a time – varying mesh stiffness.
- Application of JBA in a comb – drive actuator MEMS with an electrostatic time – dependent stiffness due to input voltage variation.
- Investigation of JBA applicability for the stability analysis of parametrically excited wind turbines due to varying gravitational force.

References

Acar, G. D., Acar, M. A. and Feeny, B. F. (2020) 'Parametric resonances of a three-blade-rotor system with reference to wind turbines', *Journal of Vibration and Acoustics, Transactions of the ASME*, 142(2), pp. 1–9. doi: 10.1115/1.4045773.

Arvin, H., Arena, A. and Lacarbonara, W. (2020) 'Nonlinear vibration analysis of rotating beams undergoing parametric instability: Lagging-axial motion', *Mechanical Systems and Signal Processing*. Elsevier Ltd, 144, p. 106892. doi: 10.1016/j.ymssp.2020.106892.

Berruti, T., Firrone, C. M. and Gola, M. M. (2011) 'A test rig for noncontact traveling wave excitation of a bladed disk with underplatform dampers', *Journal of Engineering for Gas Turbines and Power*, 133(3), pp. 1–8. doi: 10.1115/1.4002100.

Brewe, David E. and Hamrock, B. J. (1977) 'Simplified solution for elliptical-contact deformation between two elastic solids', *Journal of Tribology*. doi: 10.1115/1.3453245.

Brewe, David E and Hamrock, B. J. (1977) *technical Irieffi Simplified Solution for Elliptical-Contact Deformation Between Two Elastic Solids*. Available at: https://asmedigitalcollection.asme.org/tribology/article-pdf/99/4/485/5796557/485_1.pdf.

Bruzzone, F. and Rosso, C. (2020) 'Sources of excitation and models for cylindrical gear dynamics: A review', *Machines*, 8(3), pp. 1–19. doi: 10.3390/MACHINES8030037.

Cao, H. *et al.* (2018) 'Mechanical model development of rolling bearing-rotor systems: A review', *Mechanical Systems and Signal Processing*. Elsevier Ltd, 102, pp. 37–58. doi: 10.1016/j.ymssp.2017.09.023.

Champneys, A. (2011) 'Dynamics of Parametric Excitation', in Robert A. Meyers (ed.) *In Mathematics of Complexity and Dynamical System*. Springer, New York, NY, pp. 183–204. doi: 10.1007/978-1-4614-1806-1_13.

Chang, B. C. (2008) 'On the parametric rolling of ships using a numerical simulation method', *Ocean Engineering*, 35(5–6), pp. 447–457. doi: 10.1016/j.oceaneng.2008.01.008.

Das, S. and Wahi, P. (2017) 'Approximations for period-1 rotation of vertically

and horizontally excited parametric pendulum', *Nonlinear Dynamics*. Springer Netherlands, 88(3), pp. 2171–2201. doi: 10.1007/s11071-017-3370-z.

Detroux, T. *et al.* (2015) 'The harmonic balance method for bifurcation analysis of large-scale nonlinear mechanical systems', *Computer Methods in Applied Mechanics and Engineering*. Elsevier B.V., 296, pp. 18–38. doi: 10.1016/j.cma.2015.07.017.

Dohnal, F. and Tondl, A. (2013) 'Using time-periodicity for inducing energy transfer between vibration modes', in. ASME, pp. 1–10. doi: 10.1115/DETC2013-12936.

Dohnal, F. (2012) 'Experimental studies on damping by parametric excitation using electromagnets', *Proceedings of the Institution of Mechanical Engineers, Part C: Journal of Mechanical Engineering Science*, 226(8), pp. 2015–2027. doi: 10.1177/0954406212439515.

Dohnal, F. and Mace, B. R. (2008) 'Amplification of damping of a cantilever beam by parametric excitation', in *9th International Conference on Motion and Vibration Control*. Munich, Germany: 9th International Conference on Motion and Vibration Control.

El-Dib, Y. O. (2001) 'Nonlinear Mathieu equation and coupled resonance mechanism', *Chaos, solitons and fractals*, 12(4), pp. 705–720. doi: 10.1016/S0960-0779(00)00011-4.

Falzarano, J., Cheng, J. and Das, S. (2003) 'Parametric excitation of floating offshore platforms', in *8th International Conference on the Stability of Ships and Ocean Vehicles*. 8th International Conference on the Stability of Ships and Ocean Vehicles, pp. 507–520.

Firrone, C. M., Berruti, T. M. and Gola, M. M. (2013) 'On force control of an engine order-type excitation applied to a bladed disk with underplatform dampers', *Journal of Vibration and Acoustics, Transactions of the ASME*, 135(4), pp. 1–9. doi: 10.1115/1.4023899.

Garira, W. and Bishop, S. R. (2003) 'Oscillatory orbits of the parametrically excited pendulum', *International Journal of Bifurcation and Chaos in Applied Sciences and Engineering*, 13(10), pp. 2949–2958. doi: 10.1142/S0218127403008351.

Gastaldi, C. and Berruti, T. M. (2017) 'A method to solve the efficiency-accuracy trade-off of multi-harmonic balance calculation of structures with friction contacts', *International Journal of Non-Linear Mechanics*. Elsevier Ltd, 92(February), pp. 25–40. doi: 10.1016/j.ijnonlinmec.2017.03.010.

Gupta, T. C., Gupta, K. and Sehgal, D. K. (2011) 'Instability and chaos of a flexible rotor ball bearing system: An investigation on the influence of rotating imbalance and bearing clearance', *Journal of Engineering for Gas Turbines and Power*, 133(8), pp. 082501–082512. doi: 10.1115/1.4002657.

Hamrock B. J. and Anderson W. J. (1983) *Rolling-Element Bearings*. National Aeronautics and Space Administration.

Han, Q. and Chu, F. (2015) 'Parametric instability of flexible rotor-bearing system under time-periodic base angular motions', *Applied Mathematical Modelling*. Elsevier Inc., 39(15), pp. 4511–4522. doi: 10.1016/j.apm.2014.10.064.

Han, Q., Wang, J. and Li, Q. (2011) 'Parametric instability of a cantilever beam subjected to two electromagnetic excitations: Experiments and analytical validation', *Journal of Sound and Vibration*. Elsevier, 330(14), pp. 3473–3487. doi: 10.1016/j.jsv.2011.01.034.

Harris, T. A. (2001) *Rolling bearing analysis*. 4th edn. John Wiley.

Harsha, S. P. (2005a) 'Non-linear dynamic response of a balanced rotor supported on rolling element bearings', *Mechanical Systems and Signal Processing*, 19(3), pp. 551–578. doi: 10.1016/j.ymssp.2004.04.002.

Harsha, S. P. (2005b) 'Non-linear dynamic response of a balanced rotor supported on rolling element bearings', *Mechanical Systems and Signal Processing*, 19, pp. 551–578. doi: 10.1016/j.ymssp.2004.04.002.

Haslam, A. H., Schwingshackl, C. W. and Rix, A. I. J. (2020) 'A parametric study of an unbalanced Jeffcott rotor supported by a rolling-element bearing', *Nonlinear Dynamics*. Springer Netherlands, 99(4), pp. 2571–2604. doi: 10.1007/s11071-020-05470-4.

Hasnain, S. *et al.* (2020) 'Dynamic response of an inverted pendulum system in water under parametric excitations for energy harvesting: A conceptual approach', *Energies*, 13(19). doi: 10.3390/en13195215.

Hedlund, J. and Lehtovaara, A. (2008) 'Testing method for the evaluation of parametric excitation of cylindrical gears', *Nondestructive Testing and Evaluation*, 23(4), pp. 285–299. doi: 10.1080/10589750802258994.

Hocquet, T. and Devaud, M. (2020) 'The two-degree-of-freedom parametric oscillator: A mechanical experimental implementation', *Epl*, 132(3). doi: 10.1209/0295-5075/132/30003.

Ikeda, T., Harata, Y. and Ishida, Y. (2018) 'Parametric Instability and

Localization of Vibrations in Three-Blade Wind Turbines', *Journal of Computational and Nonlinear Dynamics*, 13(7), pp. 1–4. doi: 10.1115/1.4039899.

Jazar, G. N. (2004) 'Stability chart of parametric vibrating systems using energy-rate method', *International Journal of Non-Linear Mechanics*, 39(8), pp. 1319–1331. doi: 10.1016/j.ijnonlinmec.2003.08.009.

Khang, N. V, Cau, T. M. and Dien, N. P. (2004) 'Modelling Parametric Vibration of Gear-Pair Systems as a Tool for Aiding Gear Fault Diagnosis', *Technische Mechanik*, 24, pp. 198–205.

Kovacic, I., Rand, R. and Sah, S. M. (2018) 'Mathieu's equation and its generalizations: Overview of stability charts and their features', *Applied Mechanics Reviews*, 70(2), pp. 020802–020824. doi: 10.1115/1.4039144.

Krack, M. and Gross, J. (2019) *Harmonic Balance for Nonlinear Vibration Problems*. Springer.

Lazarus, A. and Thomas, O. (2010) 'Une méthode fréquentielle pour le calcul de stabilité des solutions périodiques des systèmes dynamiques', *Comptes Rendus - Mecanique*. Elsevier Masson SAS, 338(9), pp. 510–517. doi: 10.1016/j.crme.2010.07.020.

Lei, S. *et al.* (2017) 'Instability Analysis of Parametrically Excited Marine Risers by Extended Precise Integration Method', *International Journal of Structural Stability and Dynamics*, 17(8), pp. 1–28. doi: 10.1142/S0219455417500961.

Lin, J. and Parker, R. G. (2002) 'Planetary gear parametric instability caused by mesh stiffness variation', *Journal of Sound and Vibration*, 249(1), pp. 129–145. doi: 10.1006/jsvi.2001.3848.

Marathe, A. and Chatterjee, A. (2006) 'Asymmetric Mathieu equations', *Proceedings of the Royal Society A: Mathematical, Physical and Engineering Sciences*, 462(2070), pp. 1643–1659. doi: 10.1098/rspa.2005.1632.

Mathieu, É. (1868) 'Thesis on the vibratory movement of an elliptical membrane.', *Journal of Pure and Applied Mathematics*, 13, pp. 137–203.

Metsebo, J. *et al.* (2016) 'Modelling of a rotor-ball bearings system using Timoshenko beam and effects of rotating shaft on their dynamics', *Journal of Mechanical Science and Technology*, 30(12), pp. 5339–5350. doi: 10.1007/s12206-016-1101-x.

Moideen, H., Falzarano, J. M. and Sharma, S. A. (2012) 'Parametric roll of container ships in head waves', *Ocean Systems Engineering*, 2(4), pp. 239–255.

doi: 10.12989/ose.2012.2.4.239.

Nayfeh A. H. (1993) *Introduction to Perturbation Techniques*, *SIAM Review*. John Wiley. doi: 10.1137/1024080.

Nayfeh, A. H. (2000) *Perturbation Methods*. WILEY-VCH Verlag GmbH & Co. doi: 10.1002/9783527617609.

Nayfeh A. H., M. D. T. (1995) *Nonlinear Oscillation.pdf*. John Wiley. doi: 10.1002/9783527617586.

Qaderi, M. S., Hosseini, S. A. A. and Zamanian, M. (2018) 'Combination parametric resonance of nonlinear unbalanced rotating shafts', *Journal of Computational and Nonlinear Dynamics*, 13(11), pp. 111002–111010. doi: 10.1115/1.4041029.

Qiu, X., Han, Q. and Chu, F. (2017) 'Investigation of Parametric Instability of the Planetary Gear under Speed Fluctuations', *Shock and Vibration*, 2017. doi: 10.1155/2017/6851903.

Ramakrishnan, V. and Feeny, Brian F (2012) 'Detc2012-71532 Second Order Perturbation Analysis of a Forced Nonlinear', in. Chicago, Illinois, USA: Proceedings of the ASME 2012 International Design Engineering Technical Conferences and Computers and Information in Engineering Conference. Volume 1: 24th Conference on Mechanical Vibration and Noise, Parts A and B., pp. 1–10.

Ramakrishnan, V. and Feeny, Brian F. (2012) 'Resonances of a forced Mathieu equation with reference to wind turbine blades', *Journal of Vibration and Acoustics, Transactions of the ASME*, 134(6), pp. 1–5. doi: 10.1115/1.4006183.

Rand, R. H. (2014) *Lecture Notes on Nonlinear Optics*. Available at: http://urn.kb.se/resolve?urn=urn:nbn:se:kth:diva-9154.

Rand, R. H., Sah, S. M. and Suchorsky, M. K. (2010) 'Fractional Mathieu equation', *Communications in Nonlinear Science and Numerical Simulation*, 15(11), pp. 3254–3262. doi: 10.1016/j.cnsns.2009.12.009.

Sah, S. M. and Mann, B. (2012) 'Transition curves in a parametrically excited pendulum with a force of elliptic type', *Proceedings of the Royal Society A: Mathematical, Physical and Engineering Sciences*, 468(2148), pp. 3995–4007. doi: 10.1098/rspa.2012.0328.

Sawicki, J. T. and Kulesza, Z. (2015) 'Stability of a cracked rotor subjected to parametric excitation', *Journal of Engineering for Gas Turbines and Power*, 137(5), pp. 052508–052516. doi: 10.1115/1.4028742.

Sharma, A. *et al.* (2018) 'Nonlinear dynamic investigations on rolling element bearings: A review', *Advances in Mechanical Engineering*, 10(3), pp. 1–15. doi: 10.1177/1687814018764148.

Sinou, J. J. (2009) 'Non-linear dynamics and contacts of an unbalanced flexible rotor supported on ball bearings', *Mechanism and Machine Theory*, 44(9), pp. 1713–1732. doi: 10.1016/j.mechmachtheory.2009.02.004.

Soni, T., Dutt, J. K. and Das, A. S. (2020) 'Parametric Stability Analysis of Active Magnetic Bearing Supported Rotor System with a Novel Control Law Subject to Periodic Base Motion', *IEEE Transactions on Industrial Electronics*. IEEE, 67(2), pp. 1160–1170. doi: 10.1109/TIE.2019.2898604.

Tehrani, G. G., Gastaldi, C. and Berruti, T. M. (2021a) 'A forced response-based method to track instability of rotating systems', *European Journal of Mechanics, A/Solids*. Elsevier Masson SAS, 90(October 2020), p. 104319. doi: 10.1016/j.euromechsol.2021.104319.

Tehrani, G. G., Gastaldi, C. and Berruti, T. M. (2021b) 'Trained Harmonic Balance Method for Parametrically Excited Jeffcott Rotor Analysis', *Journal of Computational and Nonlinear Dynamics*, 16(1), pp. 011003–011014. doi: 10.1115/1.4048578.

Thomas, O., Lazarus, A. and Touzé, C. (2010) 'Oscillations of Non-Linear Structural Systems', in *Proceedings of the ASME 2010 International Design Engineering Technical Conferences & Computers and Information in Engineering Conference*. Montreal, Quebec, Canada.

Tiwari, M., Gupta, K. and Prakash, O. (2000) 'Effect of radial internal clearance of a ball bearing on the dynamics of a balanced horizontal rotor', *Journal of Sound and Vibration*, 238(5), pp. 723–756. doi: 10.1006/jsvi.1999.3109.

Tlalolini, D. *et al.* (2018) 'Modeling and characterization of an electromagnetic system for the estimation of Frequency Response Function of spindle', *Mechanical Systems and Signal Processing*. Elsevier Ltd, 104, pp. 294–304. doi: 10.1016/j.ymssp.2017.11.003.

Villa, C., Sinou, J. J. and Thouverez, F. (2008) 'Stability and vibration analysis of a complex flexible rotor bearing system', *Communications in Nonlinear Science and Numerical Simulation*, 13(4), pp. 804–821. doi: 10.1016/j.cnsns.2006.06.012.

W. SZEMPLII~ISKA-STUPNICKA (1978) 'THE GENERALIZED HARMONIC BALANCE METHOD FOR DETERMINING THE COMBINATION RESONANCE IN THE PARAMETRIC DYNAMIC SYSTEMS', *Mnras*, 58(3), pp. 347–361.

Wang, Y., Xiong, X. and Hu, X. (2021) 'Vibration and stability analysis of a bearing-rotor system with transverse breathing crack and initial bending', *Machines*, 9(4). doi: 10.3390/machines9040079.

Xu, C., Wang, Z. and Li, B. (2021) 'Dynamic Stability of Simply Supported Beams with Multi-Harmonic Parametric Excitation', *International Journal of Structural Stability and Dynamics*, 21(2), pp. 1–29. doi: 10.1142/S0219455421500279.

Yang, R. *et al.* (2018) 'The Varying Compliance Resonance in a Ball Bearing Rotor System Affected by Different Ball Numbers and Rotor Eccentricities', *Journal of Tribology*, 140(5), pp. 1–10. doi: 10.1115/1.4039566.

Yatawara, R. J., Neilson, R. D. and Barr, A. D. S. (2006) 'Theory and experiment on establishing the stability boundaries of a one-degree-of-freedom system under two high-frequency parametric excitation inputs', *Journal of Sound and Vibration*, 297(3–5), pp. 962–980. doi: 10.1016/j.jsv.2006.05.008.

Yi, Y., Qiu, Z. and Han, Q. (2018) 'The effect of time-periodic base angular motions upon dynamic response of asymmetric rotor systems', *Advances in Mechanical Engineering*, 10(3), pp. 1–12. doi: 10.1177/1687814018767172.

Younesian, D., Esmailzadeh, E. and Sedaghati, R. (2007) 'Asymptotic solutions and stability analysis for generalized non-homogeneous Mathieu equation', *Communications in Nonlinear Science and Numerical Simulation*, 12(1), pp. 58–71. doi: 10.1016/j.cnsns.2006.01.005.

Zaghari, B., Rustighi, E. and Ghandchi Tehrani, M. (2018) 'Improved Modelling of a Nonlinear Parametrically Excited System with Electromagnetic Excitation', *Vibration*, 1(1), pp. 157–171. doi: 10.3390/vibration1010012.

Zhang, D. B. *et al.* (2021) 'Dynamic stability of an axially transporting beam with two-frequency parametric excitation and internal resonance', *European Journal of Mechanics, A/Solids*. Elsevier Masson SAS, 85(July 2020), p. 104084. doi: 10.1016/j.euromechsol.2020.104084.

Zhang, X. *et al.* (2013) 'Stability analysis of a rotor-bearing system with time-varying bearing stiffness due to finite number of balls and unbalanced force', *Journal of Sound and Vibration*, 332(25), pp. 6768–6784. doi: 10.1016/j.jsv.2013.08.002.

Zhang, X. *et al.* (2016) 'A comprehensive dynamic model to investigate the stability problems of the rotor-bearing system due to multiple excitations', *Mechanical Systems and Signal Processing*. Elsevier, 70–71, pp. 1171–1192. doi: 10.1016/j.ymssp.2015.10.006.

Zhang, Z. *et al.* (2020) ‘Mechanism and characteristics of global varying compliance parametric resonances in a ball bearing’, *Applied Sciences (Switzerland)*, 10(21), pp. 1–28. doi: 10.3390/app10217849.

Zhang, Z., Chen, Y. and Cao, Q. (2015) ‘Bifurcations and hysteresis of varying compliance vibrations in the primary parametric resonance for a ball bearing’, *Journal of Sound and Vibration*. Academic Press, 350, pp. 171–184. doi: 10.1016/j.jsv.2015.04.003.

Appendices

7.1 APPENDIX A

To clarify Eq. (2.20) when $|\lambda_n| \approx 1$, consider $y_n(t+mT) = \lambda_n^m y_n(t)$ from Eq. (2.18). When:

- $\lambda_n \approx 1$, for any values of m:
  $y_n(t+mT) = y_n(t) \rightarrow y_n(t+\boldsymbol{T}) = y_n(t)$, minimum period is T **(A.1)**
- $\lambda_n \approx -1$, for odd values of m:
  $y_n(t+mT) = -y_n(t) \rightarrow$ No periodic **(A.2)**
- $\lambda_n \approx -1$, for even values of m:
  $y_n(t+mT) = -y_n(t) \rightarrow y_n(t+\boldsymbol{2T}) = y_n(t)$, minimum period is $2T$ **(A.3)**

7.2 APPENDIX B: Jacobian matrix $[\boldsymbol{J}]$

In Eq. (2.31), X and its derivatives are as follows:

$$\{r\} = \sum_{z=0,1,2,\dots}^{\infty} \left(\vec{a}_z \sin\frac{z\eta t}{2} + \vec{b}_z \cos\frac{z\eta t}{2}\right)$$

$$\{\dot{r}\} = \sum_{z=0,1,2,\dots}^{\infty} \frac{z\eta}{2}\left(\vec{a}_z \cos\frac{z\eta t}{2} - \vec{b}_z \sin\frac{z\eta t}{2}\right) \quad \textbf{(B.1)}$$

$$\{\ddot{r}\} = -\sum_{z=0,1,2,\dots}^{\infty} \left(\frac{z\eta}{2}\right)^2 \left(\vec{a}_z \sin\frac{z\eta t}{2} + \vec{b}_z \cos\frac{z\eta t}{2}\right)$$

Substituting Eq. (B.1) in $E(p)$ presented by Eq. (2.31), results in the following:

$$
\begin{aligned}
&-M\sum_{z=0,1,2,\dots}^{\infty}\left(\frac{z\eta}{2}\right)^2\left(\vec{a}_z\sin\frac{z\eta t}{2}+\vec{b}_z\cos\frac{z\eta t}{2}\right)\\
&+C\sum_{z=0,1,2,\dots}^{\infty}\frac{z\eta}{2}\left(\vec{a}_z\cos\frac{z\eta t}{2}-\vec{b}_z\sin\frac{z\eta t}{2}\right)\\
&+\left(K+K(t)\right)\sum_{z=0,1,2,\dots}^{\infty}\left(\vec{a}_z\sin\frac{z\eta t}{2}+\vec{b}_z\cos\frac{z\eta t}{2}\right)=0\,,
\end{aligned}
\tag{B.2}
$$

where, by organizing Eq. (B.2), the following equation would be obtained:

$$
\begin{aligned}
&\left(-M\sum_{z=0,1,2,\dots}^{\infty}\left(\frac{z\eta}{2}\right)^2\vec{a}_z-C\sum_{z=0,1,2,\dots}^{\infty}\frac{z\eta}{2}\vec{b}_z\right.\\
&\left.+\left(K+K(t)\right)\sum_{z=0,1,2,\dots}^{\infty}\vec{a}_z\right)\sin\frac{z\eta t}{2}\\
&+\left(-M\sum_{z=0,1,2,\dots}^{\infty}\left(\frac{z\eta}{2}\right)^2\vec{b}_z+C\sum_{z=0,1,2,\dots}^{\infty}\frac{z\eta}{2}\vec{a}_z\right.\\
&\left.+\left(K+K(t)\right)\sum_{z=0,1,2,\dots}^{\infty}\vec{b}_z\right)\cos\frac{z\eta t}{2}=0
\end{aligned}
\tag{B.3}
$$

Considering the z^{th} harmonic of Eq. (B.3) and equating the sin and cosine terms to zero:

$$
\left(K+K(t)-M\left(\frac{z\eta}{2}\right)^2\right)a_z-C\left(\frac{z\eta}{2}\right)b_z=0
\tag{B.4}
$$

$$
\left(K+K(t)-M\left(\frac{z\eta}{2}\right)^2\right)b_z+C\left(\frac{z\eta}{2}\right)a_z=0
\tag{B.5}
$$

Eq. (C.4) and (C.5) could be written as:

$$
\begin{bmatrix}\left(K+K(t)-M\left(\frac{z\eta}{2}\right)^2\right) & -C\left(\frac{z\eta}{2}\right)\\ C\left(\frac{z\eta}{2}\right) & \left(K+K(t)-M\left(\frac{z\eta}{2}\right)^2\right)\end{bmatrix}\begin{Bmatrix}a_z\\ b_z\end{Bmatrix}=0
\tag{B.6}
$$

Truncating the Fourier series by N_h harmonics:

$\boldsymbol{z = 0}$**:**

$$\begin{bmatrix} K + K(t) & 0 \\ 0 & K + K(t) \end{bmatrix} \begin{Bmatrix} a_0 \\ b_0 \end{Bmatrix} = 0$$

$\boldsymbol{z = 1}$**:**

$$\begin{bmatrix} \left(K + K(t) - M\left(\frac{\eta}{2}\right)^2\right) & -C\left(\frac{\eta}{2}\right) \\ C\left(\frac{\eta}{2}\right) & \left(K + K(t) - M\left(\frac{\eta}{2}\right)^2\right) \end{bmatrix} \begin{Bmatrix} a_1 \\ b_1 \end{Bmatrix} = 0 \qquad \textbf{(B.7)}$$

.

.

$\boldsymbol{z = N_h}$**:**

$$\begin{bmatrix} \left(K + K(t) - M\left(\frac{N_h\eta}{2}\right)^2\right) & -C\left(\frac{N_h\eta}{2}\right) \\ C\left(\frac{N_h\eta}{2}\right) & \left(K + K(t) - M\left(\frac{N_h\eta}{2}\right)^2\right) \end{bmatrix} \begin{Bmatrix} a_{N_h} \\ b_{N_h} \end{Bmatrix} = 0$$

Collecting all the harmonics, Eq. (B.7) could be written in the following compact form:

$$[J]\{A\} = 0\,, \qquad \textbf{(B.8)}$$

Where:

$$\{A\} = \begin{Bmatrix} \boldsymbol{a_0} \\ \boldsymbol{b_0} \\ \vdots \\ \boldsymbol{a_z} \\ \boldsymbol{b_z} \\ \vdots \\ \boldsymbol{a_{N_h}} \\ \boldsymbol{b_{N_h}} \end{Bmatrix}$$

$$\mathbf{J} = \begin{bmatrix} \boldsymbol{K(t)} & & & \\ & \ddots & & \\ & & \begin{bmatrix} \left(\boldsymbol{K}+\boldsymbol{K(t)}-\boldsymbol{M}\left(\frac{z\eta}{2}\right)^2\right) & -\boldsymbol{C}\left(\frac{z\eta}{2}\right) \\ \boldsymbol{C}\left(\frac{z\eta}{2}\right) & \left(\boldsymbol{K}+\boldsymbol{K(t)}-\boldsymbol{M}\left(\frac{z\eta}{2}\right)^2\right) \end{bmatrix} & \\ & & & \ddots \\ & & & \begin{bmatrix} \left(\boldsymbol{K}+\boldsymbol{K(t)}-\boldsymbol{M}\left(\frac{N_h\eta}{2}\right)^2\right) & -\boldsymbol{C}\left(\frac{N_h\eta}{2}\right) \\ \boldsymbol{C}\left(\frac{N_h\eta}{2}\right) & \left(\boldsymbol{K}+\boldsymbol{K(t)}-\boldsymbol{M}\left(\frac{N_h\eta}{2}\right)^2\right) \end{bmatrix} \end{bmatrix}$$

7.3 APPENDIX C: Formation of Eq. (2.47)

In Eq. (2.45), X and its derivatives are as follows:

$$\begin{aligned} X &= \sum_{z=0,1,2,\dots}^{\infty} \left(\vec{a}_z \sin\frac{z\eta t}{2} + \vec{b}_z \cos\frac{z\eta t}{2}\right) \\ \dot{X} &= \sum_{z=0,1,2,\dots}^{\infty} \frac{z\eta}{2}\left(\vec{a}_z \cos\frac{z\eta t}{2} - \vec{b}_z \sin\frac{z\eta t}{2}\right) \\ \ddot{X} &= -\sum_{z=0,1,2,\dots}^{\infty} \left(\frac{z\eta}{2}\right)^2 \left(\vec{a}_z \sin\frac{z\eta t}{2} + \vec{b}_z \cos\frac{z\eta t}{2}\right) \end{aligned} \quad \textbf{(C.1)}$$

Substituting Eq. (C.1) in $E(p)$ presented by Eq. (2.45), results in the following:

$$\begin{aligned} &\left(-M \sum_{z=0,1,2,\dots}^{\infty} \left(\frac{z\eta}{2}\right)^2 \left(\vec{a}_z \sin\frac{z\eta t}{2} + \vec{b}_z \cos\frac{z\eta t}{2}\right)\right. \\ &+ C \sum_{z=0,1,2,\dots}^{\infty} \frac{z\eta}{2}\left(\vec{a}_z \cos\frac{z\eta t}{2} - \vec{b}_z \sin\frac{z\eta t}{2}\right) \\ &+ (K + K(t) + M\gamma^2) \sum_{z=0,1,2,\dots}^{\infty} \left(\vec{a}_z \sin\frac{z\eta t}{2} + \vec{b}_z \cos\frac{z\eta t}{2}\right) \\ &+ \left(2M \sum_{z=0,1,2,\dots}^{\infty} \frac{z\eta}{2}\left(\vec{a}_z \cos\frac{z\eta t}{2} - \vec{b}_z \sin\frac{z\eta t}{2}\right)\right. \\ &\left.\left. + C \sum_{z=0,1,2,\dots}^{\infty} \left(\vec{a}_z \sin\frac{z\eta t}{2} + \vec{b}_z \cos\frac{z\eta t}{2}\right)\right)\gamma\right) e^{\gamma t} = 0\,, \end{aligned} \quad \textbf{(C.2)}$$

where, by organizing Eq. (C.2), the following equation would be obtained:

$$\left(\left(-M\sum_{z=0,1,2,\dots}^{\infty}\left(\frac{z\eta}{2}\right)^2\vec{a}_z - C\sum_{z=0,1,2,\dots}^{\infty}\frac{z\eta}{2}\vec{b}_z + \left(K+K(t)\right)\sum_{z=0,1,2,\dots}^{\infty}\vec{a}_z + \left(-2M\sum_{z=0,1,2,\dots}^{\infty}\frac{z\eta}{2}\vec{b}_z + C\sum_{z=0,1,2,\dots}^{\infty}\vec{a}_z\right)\gamma + M\gamma^2\sum_{z=0,1,2,\dots}^{\infty}\vec{a}_z\right)\sin\frac{z\eta t}{2} + \left(-M\sum_{z=0,1,2,\dots}^{\infty}\left(\frac{z\eta}{2}\right)^2\vec{b}_z + C\sum_{z=0,1,2,\dots}^{\infty}\frac{z\eta}{2}\vec{a}_z + \left(K+K(t)\right)\sum_{z=0,1,2,\dots}^{\infty}\vec{b}_z + \left(2M\sum_{z=0,1,2,\dots}^{\infty}\frac{z\eta}{2}\vec{a}_z + C\sum_{z=0,1,2,\dots}^{\infty}\vec{b}_z\right)\gamma + M\gamma^2\sum_{z=0,1,2,\dots}^{\infty}\vec{b}_z\right)\cos\frac{z\eta t}{2}\right)e^{\gamma t} = 0 \quad \textbf{(C.3)}$$

Considering the z[th] harmonic of Eq. (C.3) and equating the Sine and Cosine terms to zero:

$$\left(K+K(t)-M\left(\frac{z\eta}{2}\right)^2\right)a_z - C\left(\frac{z\eta}{2}\right)b_z + (-M\eta z b_z + Ca_z)\gamma + M\gamma^2 a_z = 0 \quad \textbf{(C.4)}$$

$$\left(K+K(t)-M\left(\frac{z\eta}{2}\right)^2\right)b_z + C\left(\frac{z\eta}{2}\right)a_z + (-M\eta z a_z + Cb_z)\gamma + M\gamma^2 b_z = 0 \quad \textbf{(C.5)}$$

Eq. (C.4) and Eq. (C.5) could be combined and written as:

$$\left(\begin{bmatrix}\left(K+K(t)-M\left(\frac{z\eta}{2}\right)^2\right) & -C\left(\frac{z\eta}{2}\right)\\ C\left(\frac{z\eta}{2}\right) & \left(K+K(t)-M\left(\frac{z\eta}{2}\right)^2\right)\end{bmatrix} + \begin{bmatrix}C & -M\eta z\\ -M\eta z & C\end{bmatrix}\gamma + \begin{bmatrix}M & 0\\ 0 & M\end{bmatrix}\gamma^2\right)\begin{Bmatrix}a_z\\ b_z\end{Bmatrix} = 0 \quad \textbf{(C.6)}$$

Truncating the Fourier series by N_h harmonics:

$\boldsymbol{z = 0}$**:**

$$\left(\begin{bmatrix} K + K(t) & 0 \\ 0 & K + K(t) \end{bmatrix} + \begin{bmatrix} C & 0 \\ 0 & C \end{bmatrix}\gamma + \begin{bmatrix} M & 0 \\ 0 & M \end{bmatrix}\gamma^2\right)\begin{Bmatrix} a_0 \\ b_0 \end{Bmatrix} = 0$$

$\boldsymbol{z = 1}$**:**

$$\left(\begin{bmatrix} \left(K + K(t) - M\left(\frac{\eta}{2}\right)^2\right) & -C\left(\frac{\eta}{2}\right) \\ C\left(\frac{\eta}{2}\right) & \left(K + K(t) - M\left(\frac{\eta}{2}\right)^2\right) \end{bmatrix} + \begin{bmatrix} C & -M\eta \\ -M\eta & C \end{bmatrix}\gamma + \begin{bmatrix} M & 0 \\ 0 & M \end{bmatrix}\gamma^2\right)\begin{Bmatrix} a_1 \\ b_1 \end{Bmatrix} = 0 \quad \textbf{(C.7)}$$

.

.

$\boldsymbol{z = N_h}$**:**

$$\left(\begin{bmatrix} \left(K + K(t) - M\left(\frac{N_h\eta}{2}\right)^2\right) & -C\left(\frac{N_h\eta}{2}\right) \\ C\left(\frac{N_h\eta}{2}\right) & \left(K + K(t) - M\left(\frac{N_h\eta}{2}\right)^2\right) \end{bmatrix} + \begin{bmatrix} C & -M\eta N_h \\ -M\eta N_h & C \end{bmatrix}\gamma + \begin{bmatrix} M & 0 \\ 0 & M \end{bmatrix}\gamma^2\right)\begin{Bmatrix} a_{N_h} \\ b_{N_h} \end{Bmatrix} = 0$$

Collecting all the harmonics, Eq. (C.7) could be written in the following compact form:

$$(\gamma^2\Gamma_2 + \gamma\Gamma_1 + \mathrm{J})u = 0\,, \quad \textbf{(C.8)}$$

Where:

$$\boldsymbol{u}=\begin{Bmatrix}\boldsymbol{a_0}\\ \boldsymbol{b_0}\\ \vdots\\ \boldsymbol{a_z}\\ \boldsymbol{b_z}\\ \vdots\\ \boldsymbol{a_{N_h}}\\ \boldsymbol{b_{N_h}}\end{Bmatrix},\boldsymbol{\Gamma_1}=\begin{bmatrix}\boldsymbol{C} & & & & \\ & \ddots & & & \\ & & \begin{bmatrix}\boldsymbol{C} & -\boldsymbol{Mz\eta}\\ -\boldsymbol{Mz\eta} & \boldsymbol{C}\end{bmatrix} & & \\ & & & \ddots & \\ & & & & \begin{bmatrix}\boldsymbol{C} & -\boldsymbol{M\eta N_h}\\ -\boldsymbol{M\eta N_h} & \boldsymbol{C}\end{bmatrix}\end{bmatrix}$$

$$\boldsymbol{\Gamma_2}=\begin{bmatrix}\boldsymbol{M} & & & & \\ & \ddots & & & \\ & & \begin{bmatrix}\boldsymbol{M} & \boldsymbol{0}\\ \boldsymbol{0} & \boldsymbol{M}\end{bmatrix} & & \\ & & & \ddots & \\ & & & & \begin{bmatrix}\boldsymbol{M} & \boldsymbol{0}\\ \boldsymbol{0} & \boldsymbol{M}\end{bmatrix}\end{bmatrix}$$

$$\mathbf{J}=\begin{bmatrix}\boldsymbol{K(t)} & & & & \\ & \ddots & & & \\ & & \begin{bmatrix}\left(\boldsymbol{K}+\boldsymbol{K(t)}-\boldsymbol{M}\left(\frac{z\eta}{2}\right)^2\right) & -\boldsymbol{C}\left(\frac{z\eta}{2}\right)\\ \boldsymbol{C}\left(\frac{z\eta}{2}\right) & \left(\boldsymbol{K}+\boldsymbol{K(t)}-\boldsymbol{M}\left(\frac{z\eta}{2}\right)^2\right)\end{bmatrix} & & \\ & & & \ddots & \\ & & & & \begin{bmatrix}\left(\boldsymbol{K}+\boldsymbol{K(t)}-\boldsymbol{M}\left(\frac{N_h\eta}{2}\right)^2\right) & -\boldsymbol{C}\left(\frac{N_h\eta}{2}\right)\\ \boldsymbol{C}\left(\frac{N_h\eta}{2}\right) & \left(\boldsymbol{K}+\boldsymbol{K(t)}-\boldsymbol{M}\left(\frac{N_h\eta}{2}\right)^2\right)\end{bmatrix}\end{bmatrix}$$

7.4 APPENDIX D: Computation Procedure of δ^* (David E. Brewe and Hamrock, 1977)

The proposed formula for δ^* by is as follows:

$$\delta^*=\frac{2\mathcal{F}}{\pi}\left(\frac{\pi}{\kappa^2\mathbb{E}}\right)^{\frac{1}{3}}, \qquad \textbf{(D.1)}$$

where κ is the ratio of the projected contact ellipse semi-axes a and b as shown in Figure 58 and $\mathcal{F}$ and $\mathbb{E}$ are elliptic integrals. The latter parameters are defined as follows (David E Brewe and Hamrock, 1977):

$$\kappa = \frac{a}{b}, \tag{D.2}$$

$$\mathbb{E} = 1.0003 + \frac{0.5968}{\frac{R_Y}{R_X}}, \tag{D.3}$$

$$\mathcal{F} = 1.5277 + 0.6023 \ln\left(\frac{R_Y}{R_X}\right), \tag{D.4}$$

where the parameters R_Y and R_X and the ratio in Eq. (D.2) are:

$$R_X = \frac{1}{2(\alpha_X + \beta_X)}$$
$$R_Y = \frac{1}{2(\alpha_y + \beta_y)} \tag{D.5}$$
$$\frac{a}{b} = 1.0339 \left(\frac{R_Y}{R_X}\right)^{0.636}$$

Here, α_X and α_Y are the curvatures of the ball's contact ellipse presented in Eq. (3.5); and, β_X and β_Y are the curvatures indicated in Eq. (3.6) and Eq. (3.7) for inner and outer races respectively. Depending on which contact stiffness is of interest to compute, ball – inner or ball – outer races, the value of δ^* changes.

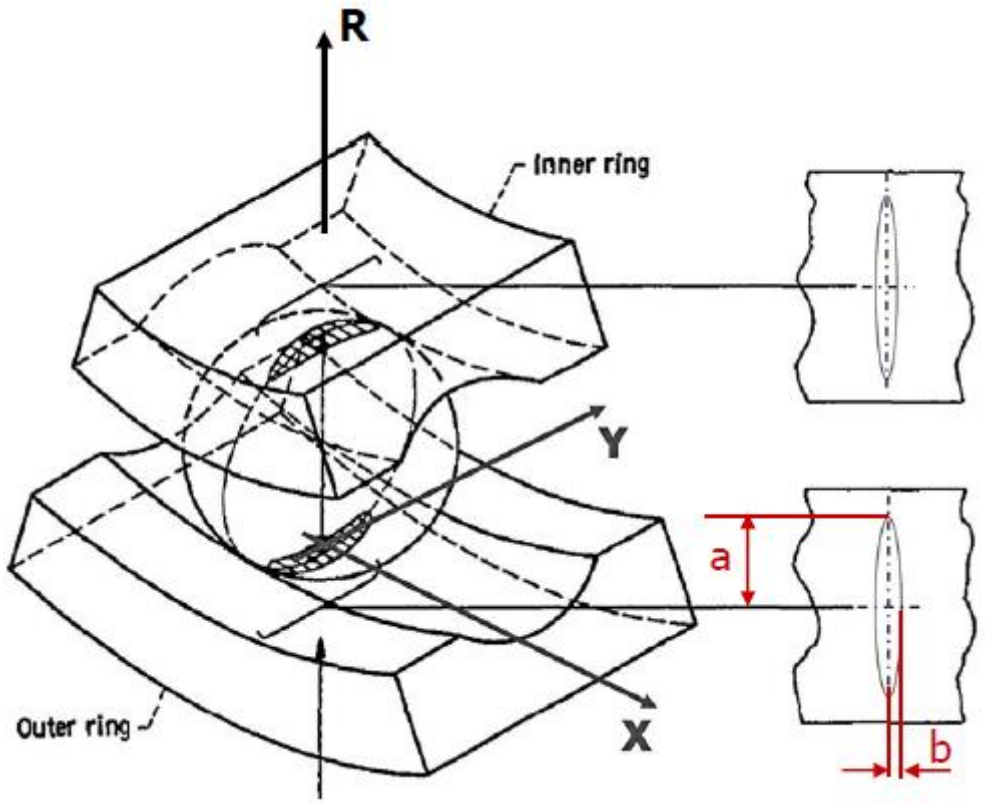

Figure 58: Schematic of the ball – races contact area with semi – axes demonstration of the contact surface[2]

7.5 APPENDIX E: Equivalent Stiffness Computation in Jeffcott Rotor

The simplified model of Figure 25 where the REB are modeled as springs is shown in Figure 59. The total displacement of the system is as follows:

$$\delta = \delta_b + \delta_s \rightarrow \begin{Bmatrix} x \\ y \end{Bmatrix} = \begin{Bmatrix} x_b \\ y_b \end{Bmatrix} + \begin{Bmatrix} x_s \\ y_s \end{Bmatrix} \quad \textbf{(E.1)}$$

In addition:

[2] The figure is taken from M.M. Gola, Machine Design Lecture Notes 2015 , Politecnico di Torino

$$\begin{Bmatrix} F_x \\ F_y \end{Bmatrix} = \begin{bmatrix} k_{xx} & k_{xy} \\ k_{yx} & k_{yy} \end{bmatrix} \begin{Bmatrix} x_b \\ y_b \end{Bmatrix}, \begin{Bmatrix} F_x \\ F_y \end{Bmatrix} = \begin{bmatrix} K_s & 0 \\ 0 & K_s \end{bmatrix} \begin{Bmatrix} x_s \\ y_s \end{Bmatrix}, \quad \textbf{(E.2)}$$

where the first matrix corresponds to the time – varying stiffness of the REB given by Eq. (3.19) and K_s is the stiffness of the shaft. Substituting $\begin{Bmatrix} x_b \\ y_b \end{Bmatrix}$ and $\begin{Bmatrix} x_s \\ y_s \end{Bmatrix}$ from Eq. (E.2) in Eq. (E.1) reults in:

$$\begin{Bmatrix} x \\ y \end{Bmatrix} = \begin{Bmatrix} F_x \\ F_y \end{Bmatrix} \left(\begin{bmatrix} k_{xx} & k_{xy} \\ k_{yx} & k_{yy} \end{bmatrix}^{-1} + \begin{bmatrix} K_s & 0 \\ 0 & K_s \end{bmatrix}^{-1} \right) = \begin{Bmatrix} F_x \\ F_y \end{Bmatrix} [\Delta] \quad \textbf{(E.3)}$$

Consequently, the equivalent stiffness system denoted by K_{eq} is equal to $[\Delta]^{-1}$.

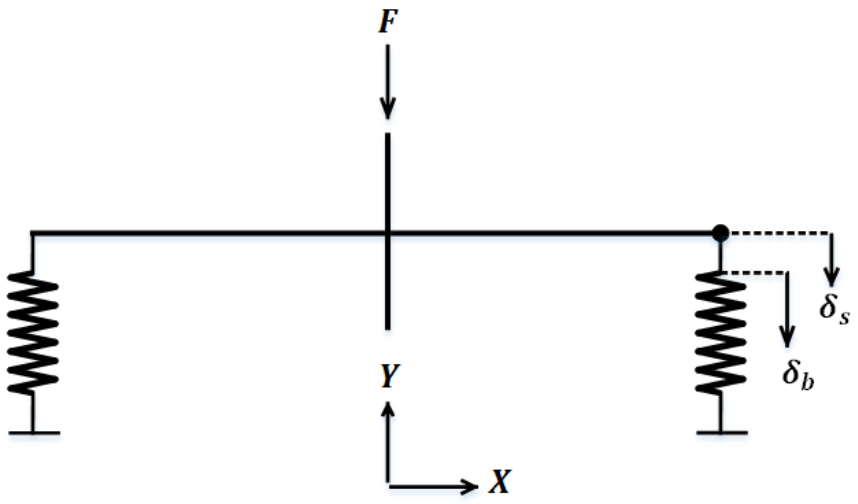

Figure 59: Equivalent mass – spring – damper model of Jeffcott rotor

7.6 APPENDIX F: Confirmation of the results in Figure 45

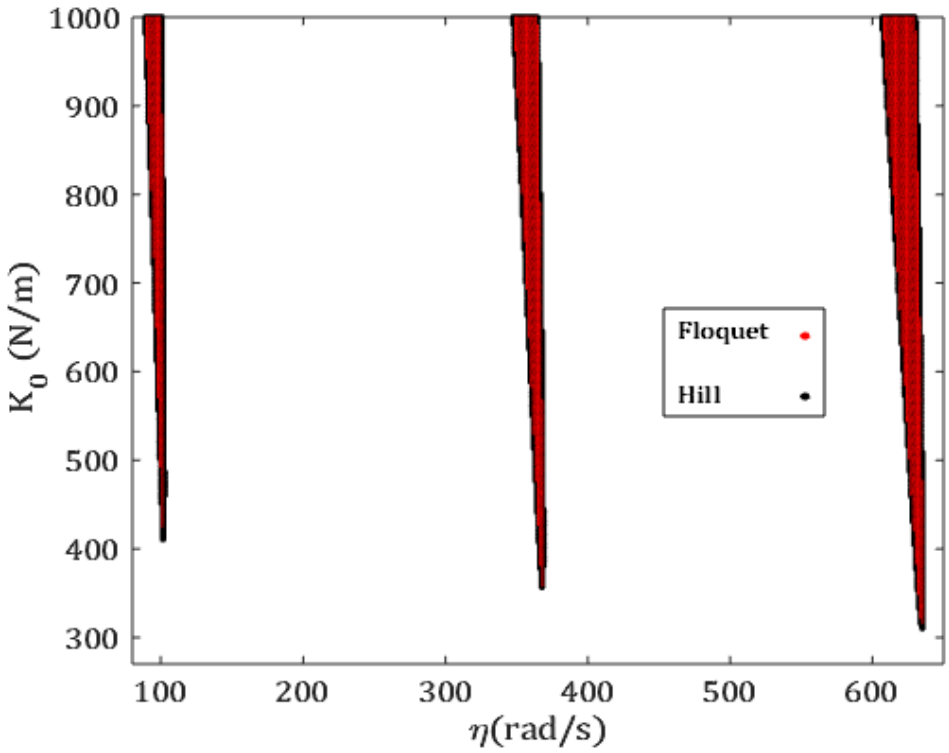

Figure 60: Equivalent mass – spring – damper model of Jeffcott rotor

7.7 APPENDIX G: Magnetic force

For the equivalent circuit of the electromagnet presented in Figure 61 the following relationship could be written (Firrone, Berruti and Gola, 2013):

$$2Ni = 2\Re_{air}\Phi = 2\frac{l_{air}}{\mu_{air}S'}\Phi\,, \qquad \textbf{(G.1)}$$

where N is the number of turns of the coil, i is the current and Φ is the magnetic flux. l_{iar} is the gap between the beam and the electromagnet, μ_{air} is the permeability of the air and S' is the area of the wedge head of the electromagnet facing the beam in which Φ/S' represents the magnetic field denoted by B. Therefore:

$$B = \frac{Ni.\mu_{air}}{l_{air}} \tag{G.2}$$

The exciting force generated by the two coils according to the principle of energy conservation (Tlalolini *et al.*, 2018):

$$f = 2f_{coil} = 2\left(\frac{B^2 S'}{2\mu_{air}}\right) \tag{G.3}$$

Substituting B from Eq. (G.2) in Eq. (G.3) and considering the alternating current as $i = I \sin \eta_e t$, the magnetic force would be:

$$f = \frac{N^2.\mu_{air}S'}{l_{air}^2} I^2 \sin^2 \eta t = \frac{N^2.\mu_{air}S'}{l_{air}^2}\frac{I^2}{2}(1 - \cos 2\eta_e t) = \frac{A}{l_{air}^2}(1 - \cos \eta t) \tag{G.4}$$

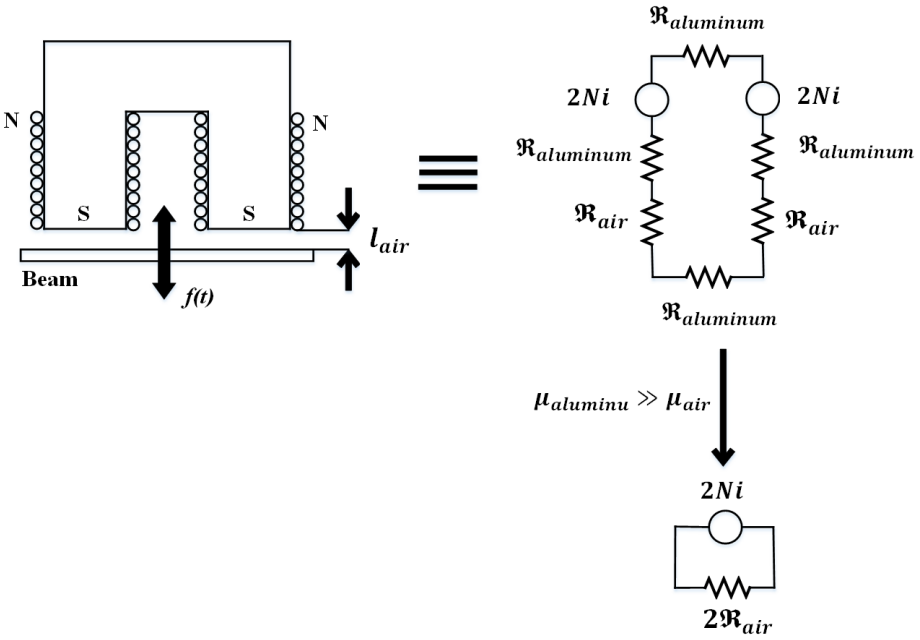

Figure 61: Schematic of equivalent magnetic circuit taken from (Berruti, Firrone, and Gola, 2011)